

## Novel catalysts and applications for polymer electrolyte membrane cells

Bunea, S.

**DOI**

[10.4233/uuid:8f2edbca-3e32-4dee-b6a3-39d5e43b4473](https://doi.org/10.4233/uuid:8f2edbca-3e32-4dee-b6a3-39d5e43b4473)

**Publication date**

2022

**Document Version**

Final published version

**Citation (APA)**

Bunea, S. (2022). *Novel catalysts and applications for polymer electrolyte membrane cells*. [Dissertation (TU Delft), Delft University of Technology]. <https://doi.org/10.4233/uuid:8f2edbca-3e32-4dee-b6a3-39d5e43b4473>

**Important note**

To cite this publication, please use the final published version (if applicable). Please check the document version above.

**Copyright**

Other than for strictly personal use, it is not permitted to download, forward or distribute the text or part of it, without the consent of the author(s) and/or copyright holder(s), unless the work is under an open content license such as Creative Commons.

**Takedown policy**

Please contact us and provide details if you believe this document breaches copyrights. We will remove access to the work immediately and investigate your claim.

# **Novel catalysts and applications for polymer electrolyte membrane cells**

Dissertation

for the purpose of obtaining the degree of doctor

at Delft University of Technology

by the authority of the Rector Magnificus prof.dr.ir. T.H.J.J. van der Hagen

chair of the Board for Doctorates

to be defended publicly on

Tuesday 26 April 2022 at 17:30 o'clock

by

Sorin BUNEA

Master of Science in Chemistry, Ruhr University Bochum, Germany

Born in Orhei, Republic of Moldova

This dissertation has been approved by the promotor.

Composition of the doctoral committee:

Rector Magnificus,	chairperson
Prof.dr.ir. A. Urakawa	Delft University of Technology, promotor
Dr. T.E. Burdyny	Delft University of Technology, copromotor

Independent members:

Prof.dr. M.T.M. Koper	Leiden University
Prof.dr. F.M. Mulder	Delft University of Technology
Dr.ir. A. Anastasopol	TNO
Prof.dr. P. Broekmann	University of Bern, Switzerland
Prof.dr.ir. W. de Jong	Delft University of Technology, reserve member

Cover design: Sorin Bunea

Copyright © 2022 Sorin Bunea

# Contents

Summary.....	7
Samenvatting.....	11
1 Introduction.....	15
1.1 Electrochemical water splitting.....	17
1.2 Electrochemical NO <sub>3</sub> <sup>-</sup> reduction.....	21
1.3 Electrochemical NO reduction.....	24
1.4 Aims of the thesis.....	25
1.5 References.....	26
2 Solution combustion synthesis of IrO <sub>2</sub> and IrO <sub>2</sub> -SnO <sub>2</sub> oxygen evolution catalysts for PEM electrolysis cells.....	31
Abstract.....	31
2.1 Introduction.....	32
2.2 Experimental.....	33
2.3 Results and discussion.....	36
2.4 Conclusions.....	45
2.5 References.....	45
3 Nanostructured Sn-Ir oxygen evolution catalysts prepared by a coprecipitation deposition method with superior activity in PEM electrolysis cells.....	49
Abstract.....	49
3.1 Introduction.....	50
3.2 Experimental.....	51
3.3 Results and discussion.....	52
3.4 Conclusions.....	61
3.5 References.....	62
4 Electrified conversion of contaminated water to value: selective conversion of aqueous nitrate to ammonia in a PEM cell.....	67
Abstract.....	67
4.1 Introduction.....	68
4.2 Experimental.....	71
4.3 Results and discussion.....	74

4.4 Conclusions.....	96
4.5 References.....	97
5 Electrochemical conversion of NO to NH <sub>3</sub> in a PEM cell.....	103
Abstract.....	103
5.1 Introduction.....	104
5.2 Experimental.....	106
5.3 Results and discussion.....	111
5.4 Conclusions.....	123
5.5 References.....	123
6 Conclusions and outlook.....	127
Acknowledgements.....	131
List of publications.....	133
Curriculum Vitae.....	135





## Summary

Polymer electrolyte membrane (PEM) water electrolysis represents a promising technology for the sustainable, emission-free hydrogen production from renewable energy, as it is able to quickly respond to fluctuations in the renewable energy supply. Nevertheless, natural scarcity of iridium, which is used as catalyst for the anodic water oxidation reaction, hinders wide-scale implementation of these cells. In this thesis we investigated how the performance of iridium catalysts can be improved by the addition of Sn and SnO<sub>2</sub>. Furthermore, despite their high efficiency, PEM cells are currently only employed for hydrogen production. We investigated whether it is possible to run other electrochemical transformations in PEM cells. Particularly, we focused on nitrate and nitric oxide reduction. These are pollutant molecules in ground water and in air, respectively. We investigated potential catalysts for the efficient transformation of these species to ammonia, which is a very important molecule for the fertilizer industry. Our approach can open new pathways for ammonia synthesis, replacing the energy-intensive, state-of-the-art Haber-Bosch process. Therefore, this thesis tackles two major topics, which are further split in four chapters. Chapters 2 and 3 are focused on oxygen evolution reaction catalysts and Chapters 4 and 5 are focused on electrochemical nitrate and nitric oxide reduction, respectively.

**Chapter 2** of this thesis explores the solution combustion synthesis method for the preparation of highly dispersed binary IrO<sub>2</sub>-SnO<sub>2</sub> catalysts. We obtained mixed oxide solid solution materials with varying IrO<sub>2</sub> and SnO<sub>2</sub> content. These materials were tested as oxygen evolution reaction (OER) catalysts in a single PEM electrolysis cell. The performance of the solid solution catalysts was inferior to state-of-the-art commercial IrO<sub>2</sub>, mainly due to the lower intrinsic catalytic activity of our materials.

In **Chapter 3**, a different class of iridium-based OER catalysts is presented. Sn-decorated iridium catalysts were prepared by a precipitation-deposition method. The goal of this synthesis approach was to study the promotion effect of Sn on the performance of iridium black catalysts in a PEM electrolysis cell. The obtained catalysts exhibit a superior performance compared to iridium black. The optimum tin loading was identified, and the



cause of the performance improvement effect was investigated by deconvoluting various overpotential contributions of membrane electrode assemblies (MEAs) containing Sn/Ir catalysts.

Aside from their high efficiency towards green hydrogen production, PEM electrolysis cells can be employed for other electrochemical transformations due to advantages like robustness, long-term stability and relatively easy scale-up. Protons that are produced in the oxygen evolution reaction at the anode of the cell which travel through the membrane to the cathode side can be used in electrocatalytic or electrolysis-assisted hydrogenation reactions. In this way, various reduction reactions can be conducted at the cathode of PEM cells, such as  $\text{CO}_2$ ,  $\text{NO}_3^-$  or  $\text{NO}_x$  reduction reactions. The advantage of using PEM cells compared to traditional thermal heterogeneous catalysis is their energy efficiency, allowing the operation at 80 °C temperature and at atmospheric pressure. Furthermore, it is more efficient to run such transformations in a single reactor, providing protons or hydrogen from the anode side to the cathode side, rather than producing hydrogen in a separate reactor and employ it in a second reactor for hydrogenation.

In **Chapter 4** we investigate the electrochemical nitrate reduction in a PEM cell. Nitrate is the most common pollutant in water bodies and its removal by state-of-the-art methods such as biological denitrification, reverse osmosis, ion exchange or catalytic hydrogenation is challenging. The electrochemical reduction approach in the PEM cells allows for continuous operation and would allow the use of renewable electricity for removal of nitrate in remote areas. The most common nitrate reduction product reported in literature is nitrogen, which is environmentally harmless but does not represent a value-added nitrate reduction product. At the same time, with the correct choice of catalyst materials, the electrochemical nitrate reduction can yield ammonia, which is the main building block of the fertilizer industry and a commercially attractive chemical. In this part of the project, four carbon-supported metal catalysts were screened for their activity in nitrate reduction, selectivity and faradaic efficiency towards ammonia. After identifying ruthenium as the most promising catalyst, reaction parameters such as anode catalyst loading, nitrate solution flow and cell potential were optimized.

Another major reactive nitrogen pollutant in the atmosphere is nitric oxide. Together with  $\text{NO}_2$ , it is part of the toxic  $\text{NO}_x$  compounds. These gases are formed in the reaction of

nitrogen and oxygen at high temperature in the combustion chamber of internal combustion engines of cars, in municipal waste incinerators and in coal or natural gas-fired power plants. In **Chapter 5** of this thesis, the first experiments of electrochemical NO reduction in a PEM electrolysis cell are reported. The same ruthenium catalyst that was found active for nitrate reduction yielded 97% NO conversion and 93% ammonia faradaic efficiency. We investigated how flow variation, anode catalyst loading and operation with hydrogen oxidation reaction (HOR) as anode reaction impacts the performance and product distribution.



## Samenvatting

Polymeer elektrolyt membraan (PEM) elektrolyse is een veelbelovende technologie voor duurzame, emissievrije, waterstofproductie uit hernieuwbare energie en het is in staat om snel op fluctuaties in de hernieuwbare energievoorziening te reageren. Echter, natuurlijke schaarste van iridium, wat gebruikt wordt als katalysator voor de anodische waterstofoxidatiereactie, belemmert grootschalige implementatie van deze cellen. In dit proefschrift hebben we onderzocht hoe de prestatie van iridium katalysators kan worden verbeterd door toevoeging van Sn of  $\text{SnO}_2$ . Verder worden, ondanks hun hoge efficiëntie, PEM cellen op dit moment alleen gebruikt voor de productie van waterstof. We hebben onderzocht of het mogelijk is om andere elektrochemische transformaties in PEM cellen uit te voeren. Met name hebben we gefocust op nitraat- en stikstofmonoxidereactie. Dit zijn respectievelijk de verontreinigde stoffen in water en lucht. We hebben potentiële katalysators onderzocht voor de efficiënte omzetting van deze stoffen naar ammoniak, wat een zeer belangrijk molecuul is voor de meststoffenindustrie. Onze aanpak kan nieuwe paden openen voor ammoniaksynthese, ter vervanging van het energie-intensieve, state-of-the-art, Haber-Bosch proces. Daartoe worden in dit proefschrift twee belangrijke onderwerpen behandeld, die verder worden opgedeeld in vier hoofdstukken. Hoofdstukken 1 en 2 focussen op de zuurstofevolutioreactie katalysators en Hoofdstukken 3 en 4 focussen respectievelijk op elektrochemische nitraat- en stikstofoxidereactie.

**Hoofdstuk 2** van dit proefschrift verkent de “solution combustion” synthesesmethode ter voorbereiding van zeer verspreide binaire  $\text{IrO}_2$ - $\text{SnO}_2$  katalysators. We verkregen zodoende een gemengd vast oxide oplossingsmateriaal, met variërende  $\text{IrO}_2$  en  $\text{SnO}_2$  inhoud. Deze materialen werden getest als zuurstofevolutioreactie (“Oxygen evolution reaction (OER)”) katalysators in een enkele PEM elektrolysecel. De prestaties van de vast oxide oplossingsmateriaal katalysators was inferieur aan state-of-the-art commerciële  $\text{IrO}_2$ , voornamelijk door de lagere intrinsieke katalytische activiteit van onze materialen.

In **Hoofdstuk 3** is een andere klasse op iridium gebaseerde OER katalysators gepresenteerd. Sn-gedecoreerde iridium katalysators werden gemaakt door middel van

een neerslag-afzettingsmethode. Het doel van deze synthese-aanpak was om de promotie-effecten van Sn op de prestaties van iridium zwart (“black”) katalysators in een PEM elektrolysecel te bestuderen. De verkregen katalysators vertonen superieure prestaties ten opzichte van iridium zwart. De optimale hoeveelheid tin werd geïdentificeerd, en de aanleiding van de prestatieverbetering werd onderzocht door het deconvolueren van de verschillende overpotentiaal bijdragen van de Sn/Ir katalysator bevattende membraan elektrode assemblages (MEA).

Naast hun hoge efficiëntie naar groene waterstofproductie, kunnen PEM elektrolysecellen worden ingezet voor andere elektrochemische omzettingen, dankzij voordelen zoals robuustheid, stabiliteit op de lange termijn en relatief eenvoudige opschaling. Geproduceerde protonen in de zuurstofevolutiereactie die aan de anode van de cel door het membraan naar de kathode kant gaan kunnen worden gebruikt in elektrokatalytische of elektrolyse-ondersteunde hydrogenatie reacties. Op deze manier kunnen verscheidene reductiereacties worden uitgevoerd aan de kathode van PEM cellen, zoals  $\text{CO}_2$ ,  $\text{NO}_3^-$  of  $\text{NO}_x$  reductiereacties. Het voordeel van het gebruik van PEM cellen ten opzichte van traditionele thermische heterogene katalyse is hun energie-efficiëntie, waardoor werking bij een temperatuur van  $80\text{ }^\circ\text{C}$  en atmosferische druk mogelijk is. Bovendien is het efficiënter om zulke omzettingen in een enkele reactor uit te voeren, om protonen of waterstof van de anodezijde naar de kathodezijde te voorzien, in plaats van waterstof in een aparte reactor te produceren en toe te passen in een tweede reactor voor hydrogenatie.

In **Hoofdstuk 4** onderzochten we elektrochemische nitraatreductie in een PEM cel. Nitraat is de meest voorkomende vervuiling in watermassa's en verwijdering door state-of-the-art methoden zoals biologische denitrificatie, omgekeerde osmose, ionenuitwisseling of katalytische hydrogenatie is uitdagend. De elektrochemische reductie aanpak in PEM cellen staat continue werking toe en zou gebruik van hernieuwbare elektriciteit voor nitraatverwijdering toestaan in afgelegen gebieden. Het meest gerapporteerde nitraatreductieproduct in de literatuur is stikstof, wat onschadelijk is voor het milieu, maar het biedt geen toegevoegde waarde als nitraatreductieproduct. Tegelijkertijd, met de juiste keuze van katalysatormateriaal, kan de elektrochemische nitraatreductie ammoniak opleveren, wat een belangrijke bouwsteen is van de meststoffenindustrie en een commercieel aantrekkelijke chemische stof. In dit deel van het project werden vier koolstof-

ondersteunde metaal katalysators gescreend voor hun activiteit in nitraatreductie, selectiviteit en faradaïsche efficiëntie naar ammoniak. Na identificatie van ruthenium als de meest belovende katalysator werden reactieparameters zoals anode katalysator hoeveelheid, nitraatoplossingsdebiet en celpotentiaal geoptimaliseerd.

Een andere grote, reactieve, stikstofvervuiler in de atmosfeer is stikstofmonoxide. Samen met  $\text{NO}_2$  maakt het deel uit van de giftige  $\text{NO}_x$  verbindingen. Deze gassen worden gevormd in de reactie van stikstof met zuurstof op hoge temperatuur in de verbrandingskamer van de verbrandingsmotor van auto's, in gemeentelijke afvalverbranders en in kolen- of gascentrales. In **Hoofdstuk 5** van dit proefschrift worden de eerste experimenten van elektrochemische stikstofmonoxidereductie in een PEM elektrolysecel gerapporteerd. Dezelfde ruthenium katalysator die actief was bevonden voor nitraatreductie gaf 97%  $\text{NO}$  omzetting en 93% ammoniak faradaïsche efficiëntie. We hebben onderzocht hoe debietvariatie, anode katalysator hoeveelheid en werking met de waterstofoxidatiereactie ("hydrogen oxidation reaction (HOR)") als anodereactie de prestaties beïnvloeden alsmede de productdistributie.





## Introduction

The use of fossil fuels for energy generation over the past two centuries has led to significant improvements of the standard of living for mankind. Contemporary life would be difficult to imagine without vehicles, fertilizer-grown crops and electricity. Nevertheless, at the beginning of the 21<sup>st</sup> century, it appears that fossil fuels have exhausted their potential to drive the human race further into the future. The alarmingly increasing CO<sub>2</sub> concentration in the atmosphere, which is produced during the burning of coal, oil and gas resources, has become a threat to our planet. CO<sub>2</sub> is a greenhouse gas, absorbing infrared radiation from Earth's surface and partially emitting it back. Over many millennia, a stable concentration of CO<sub>2</sub> in Earth's atmosphere allowed the evolution of life as we know it today. However, only in about 250 years, starting with the industrial revolution, the CO<sub>2</sub> concentration in the atmosphere has increased from around 280 parts per million to more than 400 parts per million (Figure 1.1).<sup>1,2</sup> This led to an increase of ~1 °C in the average surface temperature on Earth from 1880 to 2020 (Figure 1.2).<sup>3</sup> To prevent a further increase of the temperature on our planet, the Paris agreement was adopted by 191 countries as of 2021.<sup>4</sup> The main goal of the treaty is to keep the increase of the global temperature under 2 °C compared to pre-industrial levels.



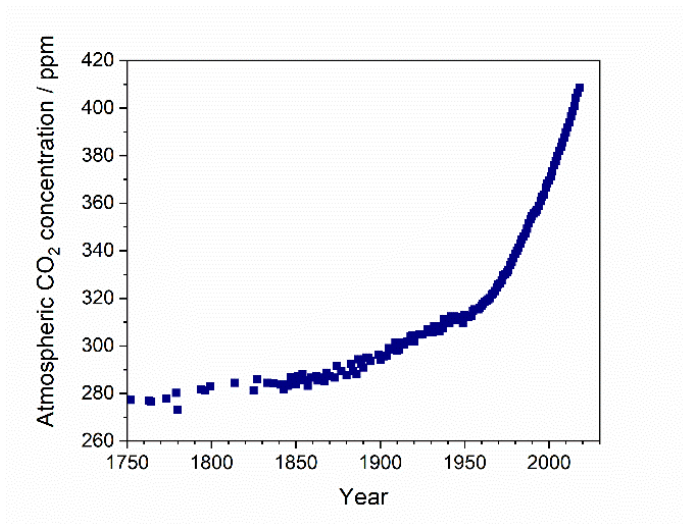


Figure I.1: Atmospheric CO<sub>2</sub> concentration increase from 18<sup>th</sup> century to present time.<sup>1,2</sup>

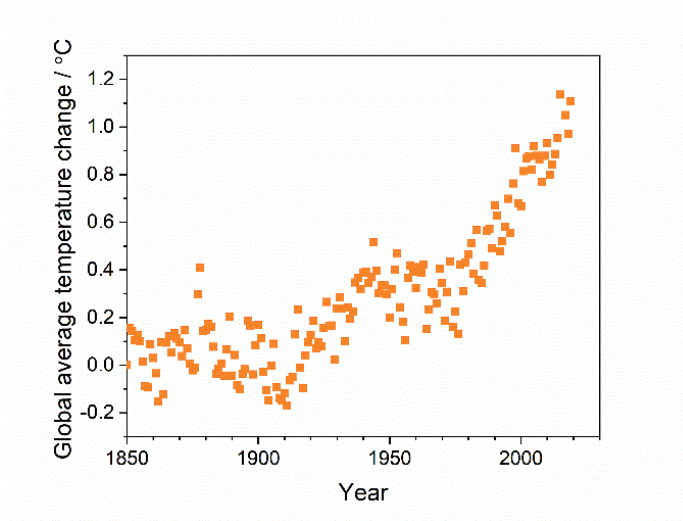


Figure I.2: Global average temperature variation from 1850 to present time.<sup>3</sup>

For this ambitious endeavor to be successful, a thorough transformation of the way we produce our energy and chemicals is required. This is particularly challenging, considering that the global energy demand is expected to increase over the next decades, with an increasing global population and improving living standards in developing countries.<sup>5</sup> The share of renewable electricity sources has increased in the last decades, but these still only account for less than 15% of the global energy sources as of 2019.<sup>6</sup> One of the main causes

for the slow rollout of renewable electricity technologies is their inherent inability to provide a stable supply over the day. Wind and sunshine are intermittent energy sources and their availabilities rarely align with our electricity demand patterns. To counter these drawbacks and make renewable electricity technologies widely adopted, novel energy storage technologies are required to act as a buffer and harmonize the electricity supply and demand cycles.

## 1.1 Electrochemical water splitting

Among available technologies to store renewable electricity, chemical energy storage has prominent advantages because of its product scope (gas, liquid or solid), transportation and on-demand utilization. Hydrogen has gained major attention in the past decade as a clean chemical energy carrier.<sup>7,8</sup> Electrolysis of water to produce hydrogen, which can be later used to produce electricity via fuel cells or employed in the chemical industry, is probably the most investigated and promising path for this electricity-to-chemical conversion. Hydrogen produced via water electrolysis is commonly referred to as *green hydrogen*. The main advantages of hydrogen as energy carrier compared to other technologies are its high storage capacity and long release time, as shown in Figure 1.3.

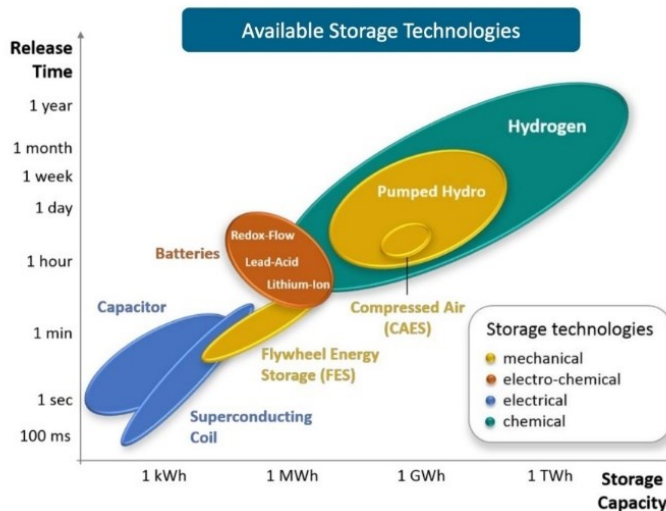


Figure 1.3: Storage capacity and release time of various energy storage technologies.<sup>9</sup>

Theoretically, a potential difference of 1.23 V ( $E_{td}$ ) is required to drive the water-splitting reaction to hydrogen and oxygen electrochemically (Eqs 1.1, 1.2). Nevertheless, in practice a larger electrical potential is required. The difference between the theoretical potential and the experimental potential is called overpotential. The application of an overpotential is caused by various losses in the system. Consequently, the total overpotential can be split into (i) the Ohmic overpotential ( $\eta_{Ohm}$ ) reflecting the electric resistance of the electrolyte, (ii) the activation overpotential ( $\eta_a$ ) accounting for the required energy for transferring electrons between the electrodes and chemical species involved in the reactions, and (iii) mass transport overpotential ( $\eta_{mt}$ ) arising from diffusion mass transport limitations and depletion of reactants at electrode surface.



Thus, an experimental cell voltage  $E_{exp}$  can be described by Eq. 1.3.

$$E_{exp} = E_{td} + \eta_{Ohm} + \eta_a + \eta_{mt} \quad \text{Eq. 1.3}$$

Alkaline water electrolysis for hydrogen production was implemented on a large scale already in the 1920s. Multiple plants at 100 MW scale were constructed and operated across the world in the following decades. However, as hydrogen became cheaper to produce via steam reforming of natural gas, the alkaline water electrolysis technology gradually went into a decline.<sup>10</sup>

With the new challenges our society is facing in the 21<sup>st</sup> century, the interest in hydrogen production via water electrolysis is renewed. The water electrolysis technology has advanced in the meantime, and the main research focus shifted from alkaline electrolysis to polymer electrolyte membrane (PEM) electrolysis. The main difference between alkaline water electrolysis and PEM electrolysis is that the latter eliminates the need for the liquid electrolyte, which are typically concentrated KOH solutions, replacing it with a solid polymer electrolyte with a thickness between 100 and 200  $\mu\text{m}$  (Figure 1.4).<sup>11</sup> Due to this decrease in electrolyte layer thickness, PEM electrolysis cells exhibit lower Ohmic losses and higher current densities which are more proportional to the amount of produced

hydrogen, and are achievable compared to alkaline water electrolyzers. Additionally, the polymeric membrane offers superior gas separation, resulting in higher purity hydrogen.

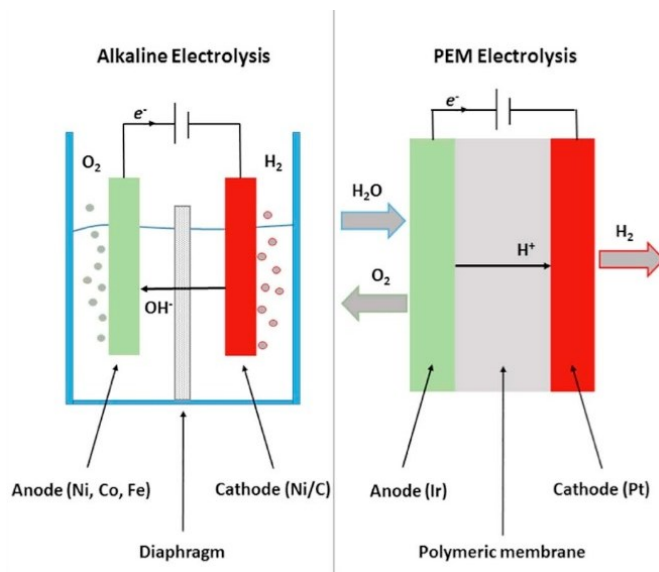


Figure 1.4: Schematic representation of alkaline and PEM water electrolysis.<sup>11</sup>

The PEM water electrolysis technology was developed in the 1960s at General Electric based on a sulfonated polystyrene membrane.<sup>12</sup> Nowadays, the most commonly used polymer material is Nafion, developed by DuPont, which consists of a sulfonated tetrafluoroethylene-based fluoropolymer-copolymer. The sulfonic group in the structure provides acidity and proton conductivity (Figure 1.5).

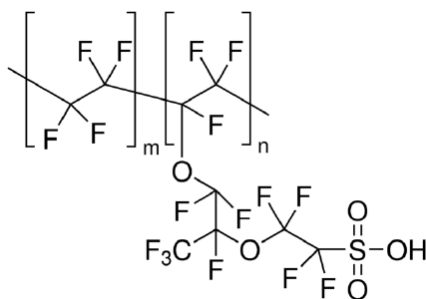


Figure 1.5: Chemical structure of Nafion.<sup>13</sup>

Despite significant technological developments, great challenges still lie ahead on the path towards large-scale implementation of green hydrogen production technologies using PEM

electrolysis. One of the greatest challenges is the scarcity and high price of state-of-the-art catalyst materials used in PEM electrolyzers, since platinum-based catalysts are used at the cathode for the hydrogen evolution reaction (HER) (Eq. 1.1), and iridium-based catalysts are used at the anode for the oxygen evolution reaction (OER) (Eq. 1.2). In fact, iridium is the rarest element in Earth's crust, with a global yearly production of only 7.1 tons.<sup>14</sup> According to the roadmap scenario of the International Renewable Energy Agency (IRENA), renewable hydrogen production should reach 19 EJ year<sup>-1</sup>, which will be equivalent to 5% of the global energy consumption.<sup>15, 16</sup> Assuming 50% of the production is by PEM electrolysis, 495 tons of iridium are needed to build the electrolyser capacity with state-of-the-art iridium loadings, according to Palmer et al.<sup>16</sup> At the current pace of iridium mining, 181 years would be needed to obtain this amount (Figure 1.6). The decrease in iridium loading is therefore crucial for deploying PEM electrolyzers on GW scale.

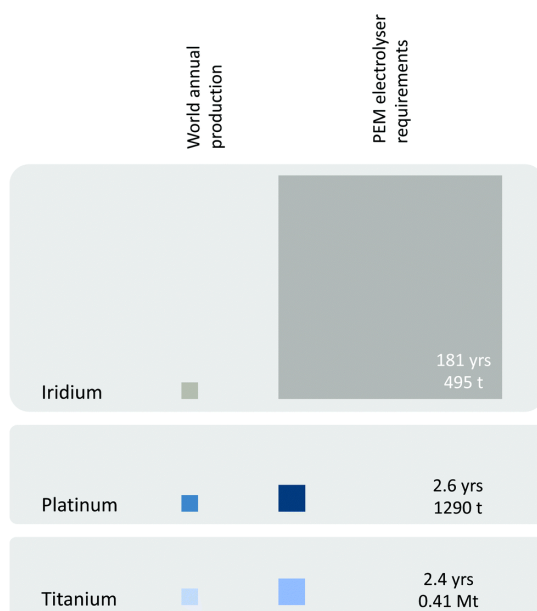


Figure 1.6: Requirement of minerals for constructing PEM electrolyser facilities to meet 50% of IRENA's 2050 renewable hydrogen production target.<sup>16</sup>

Replacing iridium-based catalysts with other more Earth-abundant materials is difficult, because iridium exhibits unparalleled activity, sitting near the top of the volcano plot correlating overpotential with the activity descriptor determined by the difference between energy states of two intermediates ( $\Delta G^{\circ}_{\text{O}^*} - \Delta G^{\circ}_{\text{HO}}$ ) (Figure 1.7).<sup>17, 18</sup> Compared to more active

materials, such as  $\text{RuO}_2$ , it has a better long-term stability in the corrosive anodic environment of PEM electrolyzers.

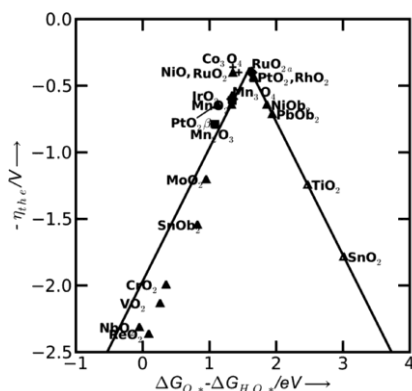


Figure 1.7: Volcano plot showing the dependency of the theoretical overpotential for oxygen evolution as a function of the difference between the standard free energy of two reaction intermediates involved in the reaction.<sup>18</sup>

Replacing Ir or  $\text{IrO}_2$  by another chemical element, a composite of mixed metals (alloy) and metal oxides is desired, but this has been found to be very challenging. An alternative approach to cope with the development is to increase the activity and utilization efficiency of Ir by catalyst engineering. Using a catalyst support to efficiently disperse iridium and preparing various nanostructures of iridium or mixing it together with another material may lead to a synergetic performance improvement, which would aid the more efficient utilization of iridium and ultimately lead to wide-scale commercialization of PEM electrolyzers.<sup>19-21</sup>

## 1.2 Electrochemical $\text{NO}_3^-$ reduction

Going one step further, PEM electrolyzers can be employed for chemical transformations other than water splitting for hydrogen production. In contrast to traditional chemical reactors, which are often part of centralized chemical plants and powered by fossil fuels, electrolyzers can be used in a decentralized fashion and are powered by renewable electricity. Furthermore, they can be potentially operated under much milder reaction conditions than traditional reactors due to the electrochemical bias to accelerate reactions. These make PEM electrolyzers attractive for applications like wastewater treatment or decentralized small-scale production of chemicals. One of such chemical transformations that is

feasible in a PEM cell is the conversion of nitrate, which is increasingly present in human activities and needs to be mitigated to protect the environment and our lives. Nitrate to harmless  $N_2$  conversion has been demonstrated recently by our group using PEM cells in combination with photocatalytic oxidation.<sup>22</sup> Alternatively, nitrate can be transformed into ammonia, which is the most important building block of the fertilizer industry. With the correct choice of catalyst materials, reaction conditions and PEM development, ammonia could be synthesized from nitrogen at near-ambient conditions from water and nitrogen via nitrate. This would greatly accelerate the transition of humanity to a more sustainable existence on Earth and might render the highly energy-demanding and polluting Haber-Bosch process obsolete.

The electrochemical nitrate reduction reaction has been extensively studied in literature and reaction pathways leading to various products have been elucidated (Figure 1.8).<sup>23</sup> Depending on the number of involved electrons and protons in the acidic environment, the formation of several N-containing products is possible (Table 1.1).

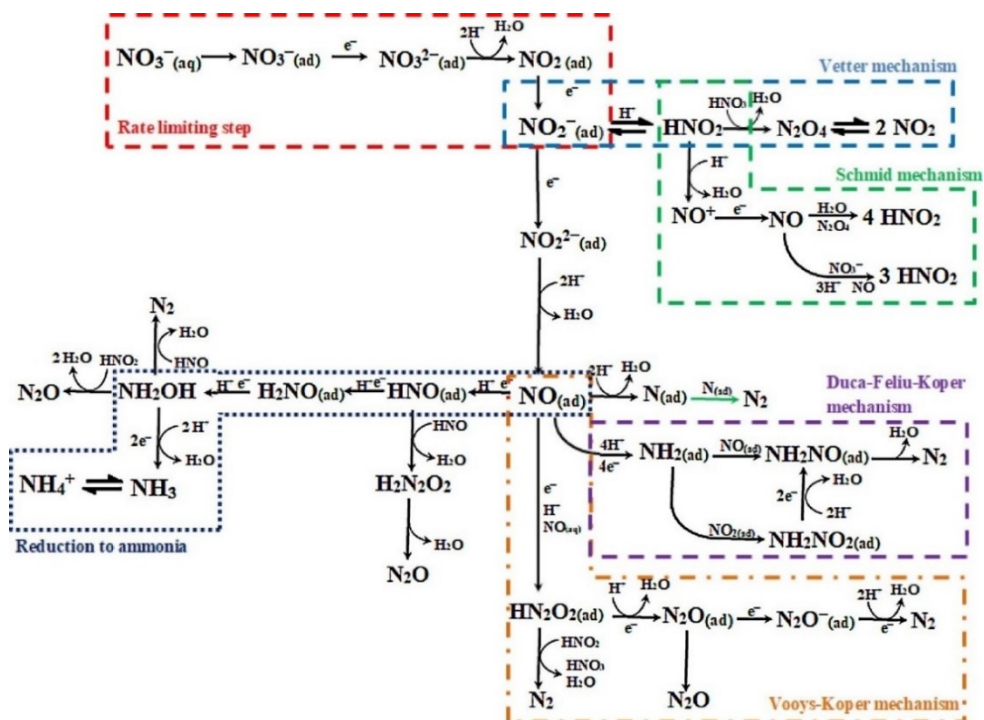


Figure 1.8: Overview of reaction mechanisms in electrochemical nitrate reduction.<sup>23</sup>

Table I.1: Nitrate reduction reactions towards various products in acidic media and corresponding standard reduction potentials.

Nitrate reduction reactions in acidic media	Standard reduction potential $E^\circ$ (V vs. SHE)
$\text{NO}_3^- + 2\text{H}^+ + \text{e}^- \rightarrow \text{NO}_2 (\text{g}) + \text{H}_2\text{O}$	+0.78
$\text{NO}_3^- + 2 \text{H}^+ + 2\text{e}^- \rightarrow \text{NO}_2^- + \text{H}_2\text{O}$	+0.84
$\text{NO}_3^- + 10\text{H}^+ + 8\text{e}^- \rightarrow \text{NH}_4^+ + 3\text{H}_2\text{O}$	+0.88
$2\text{NO}_3^- + 3\text{H}^+ + 2\text{e}^- \rightarrow 2\text{HNO}_2 + 2\text{H}_2\text{O}$	+0.94
$\text{NO}_3^- + 4\text{H}^+ + 3\text{e}^- \rightarrow \text{NO} (\text{g}) + 2\text{H}_2\text{O}$	+0.96
$2\text{NO}_3^- + 10\text{H}^+ + 8\text{e}^- \rightarrow \text{N}_2\text{O} (\text{g}) + 5\text{H}_2\text{O}$	+1.12
$2\text{NO}_3^- + 12\text{H}^+ + 10\text{e}^- \rightarrow \text{N}_2 (\text{g}) + 6\text{H}_2\text{O}$	+1.23

To have an efficient process and reduce the energy cost for separation, it is important to drive the reaction selectively towards a single reaction product. For nitrate reduction, this is particularly challenging because standard reduction potential values are close to each other, leading to the concomitant formation of several products. Furthermore, nitrite ions formed during nitrate reduction can undergo subsequent reduction (Table I.2).

Table I.2: Nitrite reduction reactions towards various products in acidic media and corresponding standard reduction potentials.

Nitrite reduction reactions in acidic media	Standard reduction potential $E^\circ$ (V vs. SHE)
$\text{NO}_2^- + 8\text{H}^+ + 6\text{e}^- \rightarrow \text{NH}_4^+ + 2\text{H}_2\text{O}$	+0.90
$\text{NO}_2^- + 2\text{H}^+ + \text{e}^- \rightarrow \text{NO} (\text{g}) + \text{H}_2\text{O}$	+1.20
$2\text{NO}_2^- + 6\text{H}^+ + 4\text{e}^- \rightarrow \text{N}_2\text{O} (\text{g}) + 3\text{H}_2\text{O}$	+1.40
$2\text{NO}_2^- + 8\text{H}^+ + 6\text{e}^- \rightarrow \text{N}_2 (\text{g}) + 4\text{H}_2\text{O}$	+1.52

An efficient way to selectively drive a reaction is by using a catalyst material which favors a reaction pathway over the others. Often, product distribution over well-defined metal electrode differs from that of powdered catalysts. This fact requires particular attention when adapting the PEM cell for electrochemical nitrate reduction.

Furthermore, an expected advantage to conducting the nitrate reduction in a PEM cell is the unique interface arising at the cathode surface, where the nitrates meet the protons



which are transported via the membrane on the catalyst surface. Precise tuning of proton transport through the membrane can lead to increased nitrate reduction rates, overcoming the competing HER (Eq. 1.1).

### 1.3 Electrochemical NO reduction

Another relevant reaction which may be conducted in a PEM cell is the electrochemical nitric oxide (NO) reduction reaction. NO together with NO<sub>2</sub> represents a strongly polluting nitrogen-containing species. It is generated during high-temperature combustion in thermal power plants, internal combustion engines of vehicles and waste incinerator facilities. Efficiently converting these emissions into harmless form (N<sub>2</sub>) or economically valuable products (e.g., NH<sub>3</sub>) would represent an important step towards a circular economy. At the same time, the lowered carbon footprint of the electrochemical conversion process N-containing species would allow for a faster transition towards a carbon-neutral society.

Electrochemical NO reduction is reported to yield four different reaction products (Table 1.3).<sup>24</sup>

Table 1.3: Nitric oxide reduction reactions towards various products in acidic media and corresponding standard reduction potentials.

Nitric oxide reduction reactions in acidic media	Standard reduction potential E° (V vs. SHE)
$2\text{NO (g)} + 4\text{H}^+ + 4\text{e}^- \rightarrow \text{N}_2 \text{(g)} + 2\text{H}_2\text{O}$	+1.68
$2\text{NO (g)} + 2\text{H}^+ + 2\text{e}^- \rightarrow \text{N}_2\text{O (g)} + \text{H}_2\text{O}$	+1.59
$\text{NO (g)} + 5\text{H}^+ + 5\text{e}^- \rightarrow \text{NH}_3 \text{(g)} + \text{H}_2\text{O}$	+0.71
$\text{NO} + 3\text{H}^+ + 3\text{e}^- \rightarrow \text{NH}_2\text{OH (g)}$	+0.38

A key intermediate in the nitric oxide reduction mechanism is the adsorbed NO species (\*NO), similar to nitrate reduction reactions (Figure 1.9).<sup>24</sup> When using similar catalyst materials, similar product distribution trends and cell voltages are expected.

Principally, the electrochemical NO<sub>x</sub> reduction process could be conducted via nitrate reduction by first absorbing gaseous species in an aqueous solution and then feeding this aqueous solution to the cathode of a PEM cell. However, this involves an additional

absorption step that would require additional equipment. Feeding gaseous  $\text{NO}_x$ -containing streams to the cathode directly represents a more facile and economical approach. Depending on the targeted reaction product, the electrochemical process can be used as a sustainable and alternative ammonia synthesis approach or as a  $\text{NO}_x$  removal technology. To compete with the scale of the Haber-Bosch process however, highly concentrated  $\text{NO}$  streams are required. As an example, these can be generated via nitrogen oxidation using plasma technology, a topic which has gained significant research interest in the recent years.<sup>25</sup>

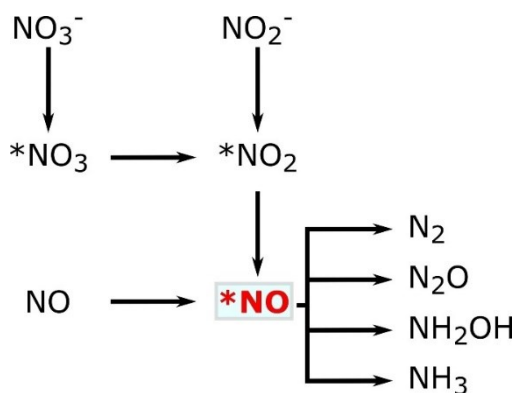


Figure 1.9: Key intermediates in electrochemical nitrate, nitrite and nitric oxide reduction mechanisms.<sup>18</sup>

## 1.4 Aims of the thesis

In Chapters 2 and 3 of this work we propose to develop more economical and efficient OER catalysts by incorporating more earth-abundant Sn and  $\text{SnO}_2$  to obtain binary Ir-Sn catalysts. Literature reports that the addition of Sn and  $\text{SnO}_2$  enhances the activity of Ir and  $\text{IrO}_2$  catalysts. We investigated what the exact role of tin/tin oxide is. Is it a good support for the iridium-active metal or does it function as a promotor? Obtaining a deeper understanding of this aspect will allow for the rational design of more efficient catalysts. For this aim, two synthesis methods, namely the one-step solution combustion method and the precipitation-deposition method with sodium borohydride reduction were evaluated to prepare distinct nanostructures and to clarify whether the formation of a mixed oxide solid-solution would yield superior catalysts or whether the two phases should be segregated.

In Chapters 4 and 5, we expand on the applicability of PEM electrolysis cells to the conversion of nitrate and nitric oxide. The use of nitrogen-containing fertilizers has led to an increase of nitrate ion (simply called nitrate or  $\text{NO}_3^-$ ) concentration in the soil and groundwater. It has to be removed to prevent eutrophication and consequences to human health (e.g., methemoglobinemia). Electrochemical conversion of nitrate to ammonia offers a unique solution to this problem by converting the undesired chemical waste into a valuable product. Replacing the platinum catalyst and suppressing HER is crucial for obtaining high efficiencies for nitrate reduction. We explore two methods to regulate the proton transport and thus suppress HER, namely by decreasing the anode catalyst amount and limiting the reactant supply at the anode of the cell.

As the reaction mechanisms of nitrate reduction and nitric oxide reduction may proceed via the same key reaction intermediate (adsorbed NO), we evaluate whether similar performances can be obtained for ammonia production when switching the cathode feed from an aqueous nitrate solution to gaseous NO. This doctoral thesis shows the high potential of PEM electrolysis cells for nitrogen oxide conversion and also hydrogenation reactions in general.

### I.5 References

1. C. MacFarling Meure, D. Etheridge, C. Trudinger, P. Steele, R. Langenfelds, T. van Ommen, A. Smith and J. Elkins, *Geophysical Research Letters*, 2006, **33**.
2. C. D. Keeling, S. C. Piper, R. B. Bacastow, M. Wahlen, T. P. Whorf, M. Heimann and H. A. Meijer, in *A History of Atmospheric CO<sub>2</sub> and Its Effects on Plants, Animals, and Ecosystems*, ed. I. T. Baldwin, M. M. Caldwell, G. Heldmaier, R. B. Jackson, O. L. Lange, H. A. Mooney, E. D. Schulze, U. Sommer, J. R. Ehleringer, M. Denise Dearing and T. E. Cerling, Springer New York, New York, NY, 2005, 83-113.
3. Giss Surface Temperature Analysis (Gistemp), Version 4. Nasa Goddard Institute for Space Studies, <https://data.giss.nasa.gov/gistemp/> (accessed January 2022)
4. United Nations Framework Convention on Climate Change, 2016.
5. Electricity Market Report - July 2021, <https://www.iea.org/reports/electricity-market-report-july-2021> (accessed January 2022)
6. V. Smil, *Energy Transitions: Global and National Perspectives*, ed. 2, Praeger, 2016.

7. Z. Abdin, A. Zafaranloo, A. Rafiee, W. Mérida, W. Lipiński and K. R. Khalilpour, *Renewable and Sustainable Energy Rev.*, 2020, **120**, 109620.
8. Staffell, D. Scamman, A. Velazquez Abad, P. Balcombe, P. E. Dodds, P. Ekins, N. Shah and K. R. Ward, *Energy Environ. Sci.*, 2019, **12**, 463.
9. <https://www.joiscientific.com/hydrogen-and-energy-storage-expanding-capacity/available-storage-technologies/> (accessed January 2022)
10. K. Zeng and D. Zhang, *Prog. Energy Combust. Sci.*, 2010, **36**, 307.
11. F. M. Sapountzi, J. M. Gracia, C. J. Weststrate, H. O. A. Fredriksson and J. W. Niemantsverdriet, *Prog. Energy Combust. Sci.*, 2017, **58**, 1.
12. M. Carmo, D. L. Fritz, J. Mergel and D. Stolten, *Int. J. Hydrogen Energy*, 2013, **38**, 4901.
13. Nafion Structure, <https://www.sigmaaldrich.com/US/en/product/aldrich/527106>, (accessed January 2022)
14. S. Kiemel, T. Smolinka, F. Lehner, J. Full, A. Sauer and R. Miehe, *International Journal of Energy Research*, 2021, **45**, 9914.
15. IRENA, Green Hydrogen Cost Reduction: Scaling up Electrolysers to Meet the 1.5 °C Climate Goal, International Renewable Energy Agency, Abu Dhabi, 2020.
16. G. Palmer, A. Roberts, A. Hoadley, R. Dargaville and D. Honnery, *Energy Environ. Sci.*, 2021, **14**, 5113.
17. E. Fabbri, A. Habereeder, K. Waltar, R. Kötz and T. J. Schmidt, *Catalysis Science & Technology*, 2014, **4**, 3800.
18. C. Man, H.-Y. Su, F. Calle-Vallejo, H. A. Hansen, J. I. Martínez, N. G. Inoglu, J. Kitchin, T. F. Jaramillo, J. K. Nørskov and J. Rossmeisl, *ChemCatChem*, 2011, **3**, 1159.
19. G. C. da Silva, S. I. Venturini, S. Zhang, M. Löffler, C. Scheu, K. J. J. Mayrhofer, E. A. Ticianelli and S. Cherevko, *ChemElectroChem*, 2020, **7**, 2330.
20. V. A. Saveleva, L. Wang, O. Kasian, M. Batuk, J. Hadermann, J. J. Gallet, F. Bournel, N. Alonso-Vante, G. Ozouf, C. Beauger, K. J. J. Mayrhofer, S. Cherevko, A. S. Gago, K. A. Friedrich, S. Zafeiratos and E. R. Savinova, *ACS Catal.*, 2020, **10**, 2508.
21. M. Ledendecker, S. Geiger, K. Hengge, J. Lim, S. Cherevko, A. M. Mingers, D. Göhl, G. V. Fortunato, D. Jalalpoor, F. Schüth, C. Scheu and K. J. J. Mayrhofer, *Nano Research*, 2019, **12**, 2275.

22. J. Ampurdanés, S. Bunea and A. Urakawa, *ChemSusChem*, 2021, **14**, 1534.
23. S. Garcia-Segura, M. Lanzarini-Lopes, K. Hristovski and P. Westerhoff, *Appl. Catal. B*, 2018, **236**, 546.
24. H. Wan, A. Bagger and J. Rossmeisl, *Angew. Chem., Int. Ed.*, 2021, **60**, 21966.
25. K. H. R. Rouwenhorst, F. Jardali, A. Bogaerts and L. Lefferts, *Energy Environ. Sci.*, 2021, **14**, 2520





# 2

## **Solution combustion synthesis of IrO<sub>2</sub> and IrO<sub>2</sub>-SnO<sub>2</sub> oxygen evolution catalysts for PEM electrolysis cells**

### **Abstract**

This chapter investigates the performance of a series of IrO<sub>2</sub>-SnO<sub>2</sub> oxygen evolution catalysts prepared by the facile solution combustion synthesis method. The performance of the materials was tested in a polymer electrolyte membrane electrolysis cell and compared to the state-of-the-art commercial IrO<sub>2</sub> catalyst. Transmission electron microscopy revealed that a mixed Ir-Sn oxide phase emerged. Nevertheless, this did not lead to a performance increase in polymer electrolyte membrane electrolysis cells, supporting previous literature reports on the use of mixed iridium-tin oxides as oxygen evolution catalysts.

This chapter is based on the following publication:

S. Bunea, P. Zeng, M. G. Willinger, A. Urakawa, *under review*.



## 2.1 Introduction

Green hydrogen obtained via water electrolysis is widely regarded as the fuel of the future, when society will finally leave the fossil-fuel era behind. Some advantages of hydrogen compared to fossil fuels are its high energy density, its possibility to be generated using renewable electricity from widely abundant water and the absence of emissions when it is used to produce energy. The most important aspect for commercial implementation of water electrolysis for hydrogen production is the cost competitiveness of this technology compared to the traditional method of obtaining hydrogen via the steam reforming of natural gas. The current production cost for grey hydrogen (from steam reforming) is 1.5-3.0 \$ kg<sup>-1</sup>. The production cost of green hydrogen is 2.5-6.0 \$ kg<sup>-1</sup>.<sup>1</sup> Consequently, there is a need to decrease the costs for green hydrogen production to make it more attractive from an economic point of view and to convince the industry to start using this technology.

PEM electrolysis is widely considered a promising technology for energy storage and clean hydrogen production due to the advantages it has over state-of-the-art alkaline water electrolysis.<sup>2</sup> Typically, PEM electrolyzers can operate at higher current densities than their alkaline counterparts, have a more robust design, and due to the zero-gap design, exhibit smaller Ohmic losses. Furthermore, PEM electrolyzers can yield hydrogen at elevated pressures, eliminating the need for compression. Nevertheless, a series of challenges hinder the large-scale commercial implementation of PEM electrolyzers. One of the main causes for the high price of green hydrogen is the high capital expenditure cost, which includes the high price of electrolyser stacks, polymeric membranes, gas diffusion layers and catalyst materials. The high cost of catalyst materials is a particularly challenging aspect, because of the nature of these materials. At the cathode, platinum-based materials are often used, with recent reports of cheaper MoS<sub>2</sub> catalysts emerging. At the anode of the PEM electrolysis cells, iridium or iridium oxide is used as catalyst for OER (Eq. 2.1). Developing alternative catalysts is difficult because iridium provides good activity and long-term stability. Nevertheless, it is possible to decrease the loading of iridium and utilize it more efficiently by using electrically conductive support materials.



In this chapter, the solution combustion synthesis (SCS) for the preparation of IrO<sub>2</sub>-SnO<sub>2</sub> catalysts was used, which is a facile one-step synthesis method to produce nano-dispersed materials as demonstrated by high Ir/IrO<sub>2</sub> dispersion in an Al<sub>2</sub>O<sub>3</sub> matrix.<sup>3</sup> The Al<sub>2</sub>O<sub>3</sub> was replaced with SnO<sub>2</sub> due to its superior electronic conductivity and literature reports that the addition of SnO<sub>2</sub> enhances the activity of IrO<sub>2</sub> catalysts.<sup>4,6</sup>

## 2.2 Experimental

### 2.2.1 Catalyst synthesis

SCS requires three components: a soluble metal salt precursor which is typically chloride or nitrate, an oxidizing agent such as ammonium nitrate and a fuel, which can be an oxidizable organic molecule. Often, these organic molecules can chelate the metal ion, leading to a better mixing of the components, which can yield a smaller size of the resulting metal oxide powder. These are dissolved in a solvent and the mixture is heated to a temperature of 10 degrees below the boiling point of the solvent on a heating plate. As the solvent evaporates, the mixture turns into a gel. At this point, the crucible containing the gel is transferred to a preheated furnace and the temperature is ramped up to the desired calcination temperature. As the temperature increases, the gel ignites, and an intense gas formation can be observed. During the combustion, temperatures of up to 1000 °C can be reached. The fast combustion yields fine metal oxide powders which do not require further washing and drying steps. A schematic of SCS is presented in Figure 2.1.

IrO<sub>2</sub>-SnO<sub>2</sub> powders were synthesized via the solution combustion method. IrCl<sub>3</sub>·xH<sub>2</sub>O (Precious Metals Online Ltd) and SnCl<sub>4</sub>·5H<sub>2</sub>O (Sigma Aldrich) were used as metal precursor salts, glycine (Alfa Aesar) was used as fuel and ammonium nitrate (Sigma Aldrich) was used as oxidizing agent. A stoichiometric ratio of components, according to  $\phi$  parameter ( $\phi=1$ ), which is described elsewhere, was used.<sup>7</sup> The components were mixed together and dissolved in a minimum amount of water in a porcelain crucible. The mixture was stirred on a heating plate at 90 °C until the water evaporated and a gel was formed. After the gel formation, the crucible was transferred to a preheated furnace at 90 °C and the temperature was ramped up to 500 °C, at a rate of 10 °C min<sup>-1</sup>, and was held at this temperature for 3

hours for the calcination of the powders and removal of carbon compounds which might have remained after the combustion. The obtained powders were used as OER catalysts without any further treatment steps.

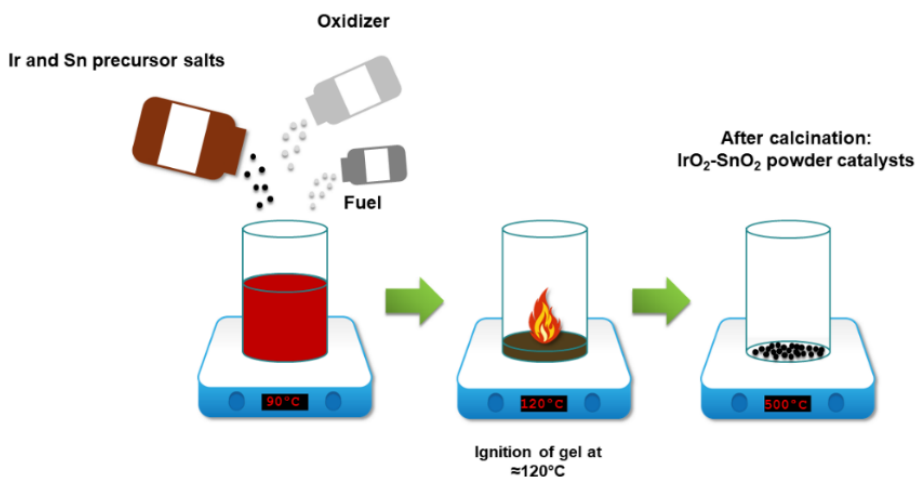


Figure 2.1: Schematic representation of SCS.

### 2.2.2 Preparation of catalyst-coated membranes (CCMs)

To test the iridium oxide-based catalyst powders in the PEM electrolysis cell, these powders have to be deposited either on gas-diffusion electrodes or over the membrane. For an improved contact of the catalyst particles and the polymeric membrane, the first step of the deposition process involves the incorporation of the powders in an ink. Besides the catalyst powder, this ink contains a dispersion of the polymer material of the membrane (ionomer) and a solvent. Nafion 115 membranes (Ion Power) were used for all experiments. The membranes were pre-treated in 3 wt% H<sub>2</sub>O<sub>2</sub> for 1 h at 80 °C to remove any organic impurities, then for 1 h at 80 °C in 1 M H<sub>2</sub>SO<sub>4</sub> to ensure the sulfonic groups of the polymer are protonated, and finally for 1 h in boiling milliQ water.

Commercial 40 wt% Pt/C (Sigma Aldrich) was used as cathode catalyst for all membrane electrode assemblies (MEAs). Catalyst inks containing the dry powder, 30 wt% of the dry catalyst Nafion ionomer and 1 mL ionomer were prepared.

Anode catalyst inks were prepared in a similar fashion. The Nafion ionomer was set at 20 wt% of the dry catalyst loading and 2 mL of isopropanol was used. The catalyst loading on MEAs was set at  $2 \text{ mg cm}^{-2}$  for  $\text{IrO}_2\text{-SnO}_2$  and Sn/Ir catalysts. As described in the results section, variable loadings of commercial  $\text{IrO}_2$  and iridium black loadings were used.

The catalyst inks were spray-coated on the membranes, which were fixed between in-house designed two aluminum plates heated at  $60 \text{ }^\circ\text{C}$ . The geometric catalyst-coated area of membranes was  $4 \text{ cm}^2$  (Figure 2.2a). After spray-coating the catalysts, the membranes were hot-pressed at  $130 \text{ }^\circ\text{C}$ ,  $25 \text{ kg cm}^{-2}$  for 3 minutes.

### 2.2.3 Cell assembly

Subsequently the catalyst-coated membranes were sandwiched between two  $0.45 \text{ }\mu\text{m}$  thick platinum-coated titanium felt plates which acted as gas diffusion layers (GDLs), and were assembled in an in-house designed single PEM electrolysis cell with titanium collectors and single serpentine flow channels, as shown in assembled form in Figure 2.2b. For a higher corrosion resistance, the area of the collectors in contact with GDLs is gold-coated (Figure 2.2c).

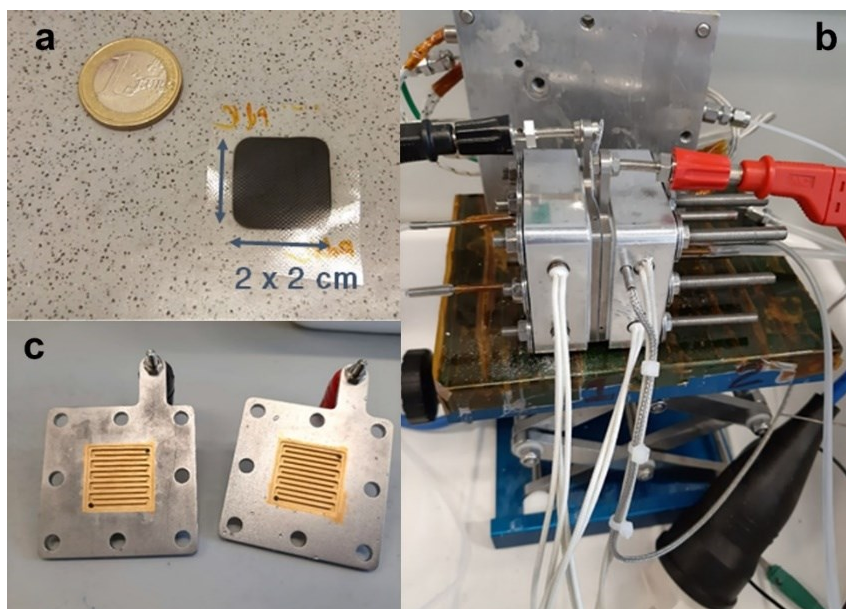


Figure 2.2: (a) Catalyst coated membrane, (b) PEM electrolysis cell in assembled form and (c) bipolar plates with gold-coated serpentine flow channels.

### 2.2.4 Electrochemical experiments

Water electrolysis experiments were conducted at 80 °C. MilliQ water was fed both to the anode and the cathode compartments of the PEM cell at a flow rate of 1 mL min<sup>-1</sup> using a peristaltic pump (Ismatec Reglo Digital). The water was preheated at 85 °C before being passed through the PEM cell.

Linear sweep voltammetry experiments were conducted with a PGSTAT 302N potentiostat (Metrohm Autolab), equipped with a 20A booster. The potential was scanned in the 1.3-2.2 V range. The scan rate was set at 15 mV min<sup>-1</sup>. Electrochemical impedance spectroscopy experiments were conducted at 1.5 V, with a perturbation wave of 10 mV in the 16 kHz – 100 MHz frequency range. Spectra were fitted using the NOVA software. Galvanostatic chronoamperometry experiments were performed at 1 A cm<sup>-2</sup> current density for 24 h.

### 2.2.5 Catalyst characterization

N<sub>2</sub> physisorption experiments were performed using a Micromeritics Tristar 3020 setup after an overnight degassing step at 150 °C. X-ray diffractograms of the powders were recorded with a Bruker D8 Discover powder diffractometer with a Co K-alpha radiation source and Bruker D8 Advance with a Cu K-alpha radiation source. Scanning electron micrographs were recorded with a JEOL 6010 microscope.

## 2.3 Results and discussion

Several synthesis methods for IrO<sub>2</sub>-SnO<sub>2</sub> OER catalysts based on the modified Adams fusion method, the modified polyol method and template-assisted synthesis are reported in literature.<sup>4, 8-10</sup> Often obtaining nanosized iridium oxide powder catalysts involve a series of steps which are time and resource consuming. The SCS method can yield nanoparticulate oxide catalyst powders in one step, eliminating washing and separation procedures. This poses significant advantages in the context of reducing the CO<sub>2</sub> footprint of catalyst manufacturing and achieving a more sustainable chemical industry. We took this advantage of SCS and applied this method to prepare a series of IrO<sub>2</sub>-SnO<sub>2</sub> catalysts with 10, 25, 50, 75 and 90 wt% SnO<sub>2</sub> content. The IrO<sub>2</sub>-SnO<sub>2</sub> catalysts were tested for their oxygen evolution activity in a single PEM electrolysis cell, accompanying HER at the cathode.

### 2.3.1 Iridium oxide-tin oxide catalyst characterization

The synthesized powders were characterized by X-ray diffraction (XRD), nitrogen physisorption and transmission electron microscopy (TEM). The most significant observation in the XRD patterns of the catalysts is the shift of the most intense peaks compared to the reference values for  $\text{IrO}_2$  and  $\text{SnO}_2$  (Figure 2.3). This shift is indicative of a mixed oxide formation, and more precisely of a solid-solution formation.  $\text{IrO}_2$  and  $\text{SnO}_2$  both crystallize in a tetragonal phase with  $a = 0.4499$  nm,  $c = 0.3146$  nm for  $\text{IrO}_2$  and  $a = 0.4738$  nm,  $c = 0.31865$  nm for  $\text{SnO}_2$ , respectively.<sup>11, 12</sup> Ionic radii of  $\text{Ir}^{4+}$  and  $\text{Sn}^{4+}$  are also similar with 0.077 nm and 0.083 nm, respectively. As pointed by Xu et al., according to the Hume-Rothery theory, the formation of a solid solution of  $\text{IrO}_2$  and  $\text{SnO}_2$  should be possible.<sup>4</sup> The authors mention that metastable solid solutions of  $\text{IrO}_2$  and  $\text{SnO}_2$  are formed under well-defined composition and temperature conditions. More recently, Marshall et al. succeeded in obtaining a metastable solid solution of Ir-Sn oxides via a modified polyol method.<sup>8</sup> Interestingly, the authors found that the Adams fusion method yields a material with two distinct phases, an iridium-rich and a tin-rich phase. The reason for the formation of the solid solution is the formation of a highly mixed Ir-Sn phase during synthesis, which is not achieved via the Adams fusion method. In a further study, Marshall et al. tested their Ir-Sn mixed oxide powders prepared by the polyol method in a PEM cell.<sup>9</sup> Unfortunately, the catalysts containing tin showed inferior performance than neat  $\text{IrO}_2$  catalysts.

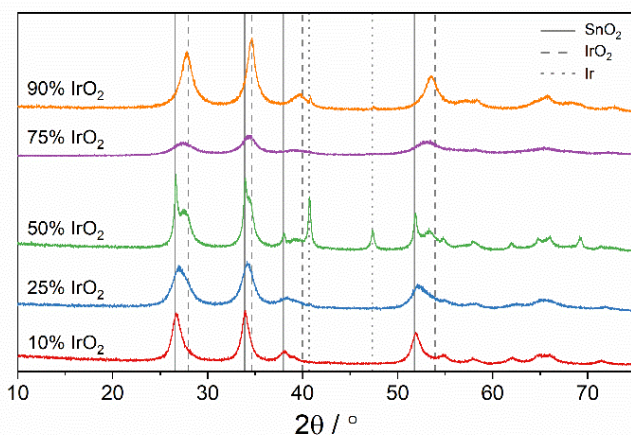


Figure 2.3: X-ray diffractograms of  $\text{Ir}_x\text{Sn}_{(1-x)}\text{O}_2$  powders synthesized by the SCS.

We performed lattice parameter refinement of X-ray diffractograms to determine sample composition. A good agreement of the experimentally determined lattice parameter  $a$  with values predicted according to Vegard's law was found (Figure 2.4). The formation of solid solutions, matching the Ir:Sn ratio calculated during synthesis, was confirmed. The surface area of the SCS-prepared samples determined by nitrogen physisorption varied between 24 and 68  $\text{m}^2 \text{g}^{-1}$  (Table 2.1). No clear correlation was observed between the  $\text{IrO}_2$  and  $\text{SnO}_2$  ratio and the surface area of the catalyst powders.

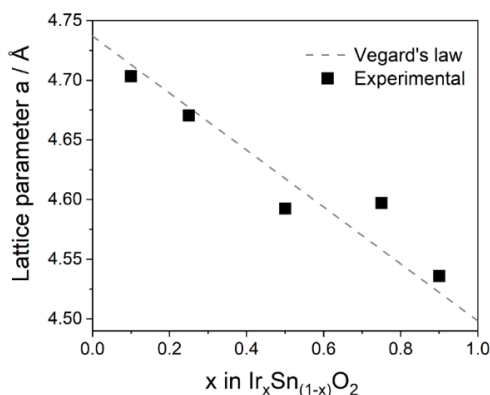


Figure 2.4: Lattice parameter  $a$  as a function of solid solution composition in iridium oxide-tin oxide SCS catalysts.

Table 2.1: BET surface area of  $\text{IrO}_2$ - $\text{SnO}_2$  SCS catalysts determined by nitrogen physisorption.

Catalyst	Surface area ( $\text{m}^2 \text{g}^{-1}$ )
90% $\text{IrO}_2$ -10% $\text{SnO}_2$	43
75% $\text{IrO}_2$ -25% $\text{SnO}_2$	68
50% $\text{IrO}_2$ -50% $\text{SnO}_2$	25
25% $\text{IrO}_2$ -75% $\text{SnO}_2$	42

Needle-like crystallites similar to those previously observed in our work on solution combustion-prepared  $\text{IrO}_2$ - $\text{Al}_2\text{O}_3$  catalysts were observed in transmission electron micrographs (Figure 2.5, 2.6).<sup>3</sup> From energy-dispersive X-ray spectroscopy (EDS) mapping, high dispersion and mostly uniform distribution of Ir and Sn throughout the particle can be observed (Figure 2.5, 2.7). This is in good agreement with the findings from XRD analysis, indicating the formation of an iridium-tin oxide solid solution.

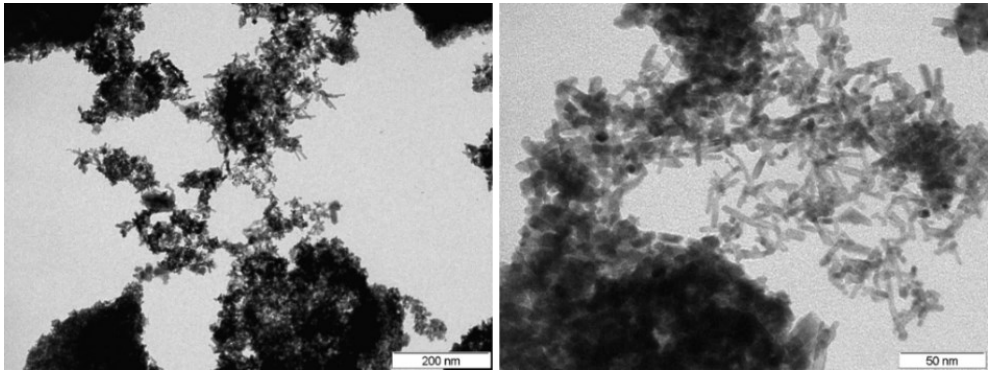


Figure 2.5: Transmission electron micrograph of Ir<sub>0.75</sub>Sn<sub>0.25</sub>O<sub>2</sub> powder.

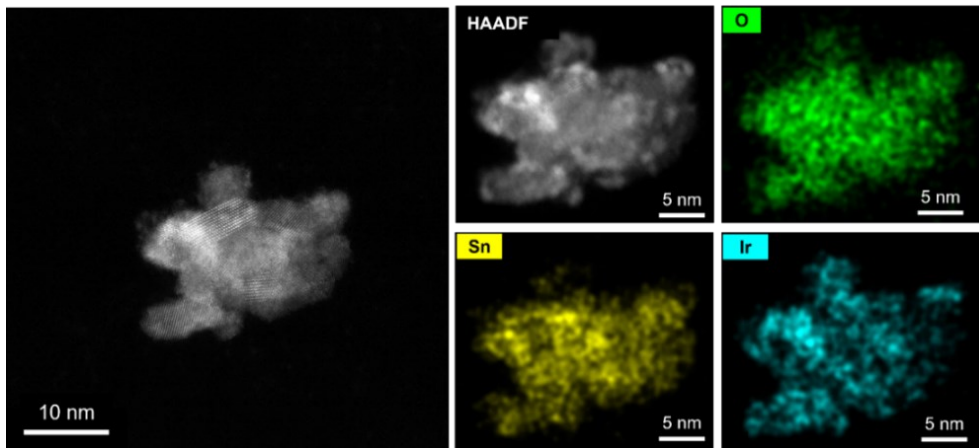


Figure 2.6: High resolution transmission electron micrograph of an Ir<sub>0.75</sub>Sn<sub>0.25</sub>O<sub>2</sub> catalyst synthesized by the SCS and energy dispersive X-ray (EDS) map showing the distribution of Sn and Ir.

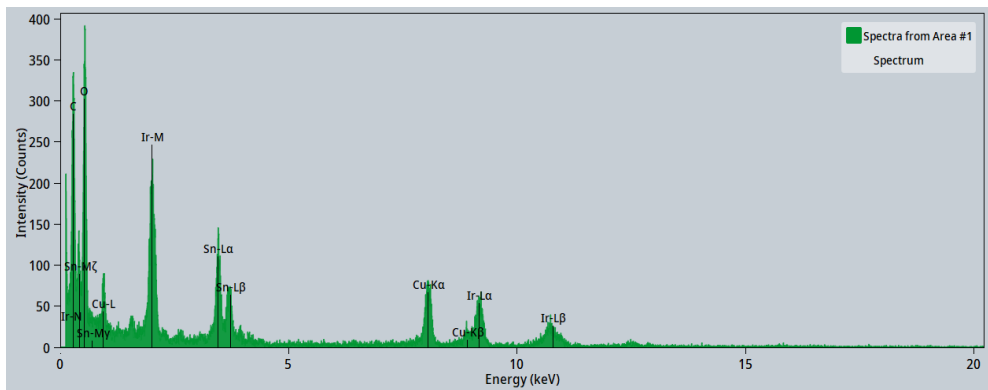


Figure 2.7: Energy dispersive X-ray spectrum of the Ir<sub>0.75</sub>Sn<sub>0.25</sub>O<sub>2</sub> catalyst synthesized by the SCS presented in Figure 2.6



### 2.3.2 $\text{Ir}_x\text{Sn}_{(1-x)}\text{O}_2$ – PEM cell performance and overpotential analysis

After the successful synthesis and the observation of mixed oxide formation, we proceeded with testing the samples in the PEM cell for their catalytic activity in OER. For a fair comparison, we tested a series of MEAs containing comparable commercial  $\text{IrO}_2$  loadings to  $\text{Ir}_x\text{Sn}_{(1-x)}\text{O}_2$  MEAs. The anode catalyst loading for  $\text{Ir}_x\text{Sn}_{(1-x)}\text{O}_2$  MEAs was fixed at  $2 \text{ mg cm}^{-2}$ . The loading of iridium oxide MEAs was set at 0.2, 0.5, 1, 1.5 and  $2 \text{ mg cm}^{-2}$ . The assessment of MEA performance was conducted by recording polarization curves in the 1.3-2.2 V cell voltage range (Figure 2.8). As a first observation, the inferior performance of  $\text{Ir}_x\text{Sn}_{(1-x)}\text{O}_2$  MEAs compared to commercial iridium oxide MEAs, even at low catalyst loadings, is noted.

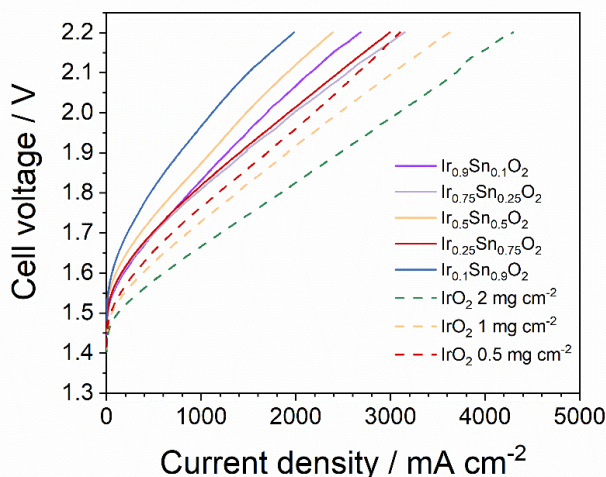


Figure 2.8: Polarization curves of  $\text{Ir}_x\text{Sn}_{(1-x)}\text{O}_2$  and commercial  $\text{IrO}_2$  MEAs,  $0.75 \text{ mg cm}^{-2}$  40 wt% Pt/C cathode catalyst, Nafion 115,  $80^\circ\text{C}$ .

To understand the origin of poorer performance and higher cell voltage when the SCS-synthesized materials were used, the contribution of various overpotentials was decoupled by deconvoluting the polarization curves (Figure 2.9).<sup>28-30</sup> The kinetic overpotential is accessible from the Tafel plot analysis of  $iR$ -free polarization curves. The Ohmic overpotential can be determined from the Ohmic resistance measured by electrochemical impedance spectroscopy (EIS). It is characterized by a single parameter, which is the cell resistance determined from the high frequency intercept (HFR) of impedance spectra measured for each MEA (Figure 2.10). Ohmic resistance values, together with the kinetic

parameters for each MEA, are summarized in Table 2.2. The thermodynamic cell voltage is determined using the Nernst equation. As the cell was operated at  $80\text{ }^\circ\text{C}$ , the calculated value of the thermodynamic potential is  $1.18\text{ V}$ . The remaining overpotential contribution, after subtraction of the aforementioned terms, can be assumed to correspond to mass transport overpotential.<sup>29</sup>

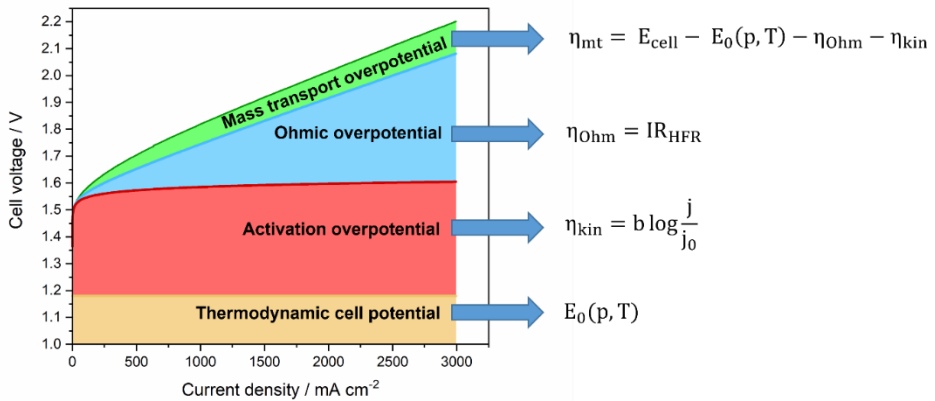


Figure 2.9: Overpotential contributions to overall cell voltage in a typical polarization curve of a PEM electrolyser and the corresponding equations used to model each parameter.

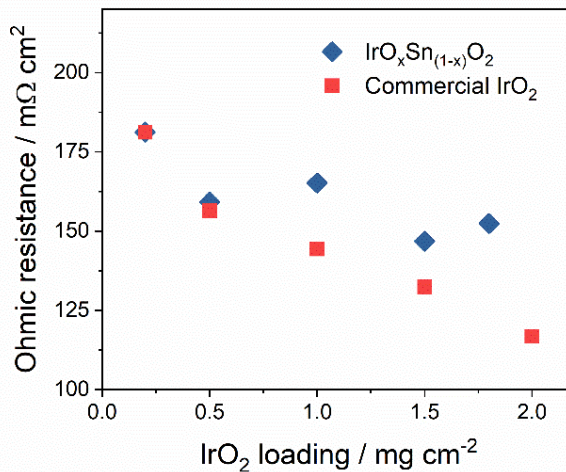


Figure 2.10: Ohmic resistance determined by EIS as a function of  $\text{IrO}_2$  loading for  $\text{Ir}_x\text{Sn}_{(1-x)}\text{O}_2$  and commercial  $\text{IrO}_2$  MEAs.

Table 2.2: Kinetic parameters determined from Tafel plot analysis and Ohmic resistance recorded by EIS for IrO<sub>2</sub>-SnO<sub>2</sub> SCS and commercial IrO<sub>2</sub> MEAs.

MEA	Apparent Tafel slope (mV dec <sup>-1</sup> )	log j <sub>0</sub>	R <sub>el</sub> (Ω cm <sup>2</sup> )
90%IrO <sub>2</sub> -10%SnO <sub>2</sub>	40.47	-6.83	152.4
75%IrO <sub>2</sub> -25%SnO <sub>2</sub>	40.77	-7.02	146.8
50%IrO <sub>2</sub> -50%SnO <sub>2</sub>	40.12	-7.49	165.2
25%IrO <sub>2</sub> -75%SnO <sub>2</sub>	40.83	-6.93	159.2
10%IrO <sub>2</sub> -90%SnO <sub>2</sub>	40.73	-7.67	181.2
Commercial IrO <sub>2</sub> 2 mg cm <sup>-2</sup>	41.52	-5.80	116.8
Commercial IrO <sub>2</sub> 1.5 mg cm <sup>-2</sup>	41.18	-5.24	132.4
Commercial IrO <sub>2</sub> 1 mg cm <sup>-2</sup>	41.64	-5.64	144.4
Commercial IrO <sub>2</sub> 0.5 mg cm <sup>-2</sup>	41.51	-5.80	156.4
Commercial IrO <sub>2</sub> 0.2 mg cm <sup>-2</sup>	53.46	-5.14	181.2

The Ohmic resistance of commercial iridium oxide MEAs increases linearly with decreasing iridium oxide loading. This correlation has been observed and described in literature. It can be explained by the decrease in catalyst layer thickness with loading, leading to a less contiguous and less uniform catalyst layer with a higher in plane resistance.<sup>31, 32</sup> For Ir<sub>x</sub>Sn<sub>(1-x)</sub>O<sub>2</sub> MEAs, a similar trend was observed. In comparison to the commercial iridium oxide MEAs, recorded Ohmic resistance values for Ir<sub>x</sub>Sn<sub>(1-x)</sub>O<sub>2</sub> were higher for similar iridium oxide loadings. This is likely due to a lower electronic conductivity of Ir<sub>x</sub>Sn<sub>(1-x)</sub>O<sub>2</sub> powders compared to IrO<sub>2</sub>, as reported in literature for IrO<sub>2</sub>-TiO<sub>2</sub> powders and Ir-Sn mixed oxides.<sup>24, 33</sup>

The kinetic overpotential is determined by two parameters: (i) the apparent Tafel slope, from which the reaction mechanism can be derived, and (ii) the exchange current density, which contains information about the intrinsic catalytic activity of the materials and available reaction sites. The apparent Tafel slopes for most of the tested MEAs exhibited values around 40-41 mV dec<sup>-1</sup>, in agreement with commonly reported literature values for iridium-based OER catalysts (Table 2.2).<sup>34, 35</sup> Ir<sub>x</sub>Sn<sub>(1-x)</sub>O<sub>2</sub> MEAs exhibited exchange current densities of two orders of magnitude lower than commercial IrO<sub>2</sub> MEAs (Figure 2.11). The

deconvolution of the activation overpotential clearly shows that the mixed oxide powders have a lower intrinsic catalytic activity for OER compared to commercial  $\text{IrO}_2$ . Based on the remarkable differences observed between the commercial catalyst and the mixed oxide materials, the lower intrinsic catalytic activity appears to be the critical parameter for the lower performance of  $\text{Ir}_x\text{Sn}_{(1-x)}\text{O}_2$  powders. In each series, a slight decrease in exchange current density with decreasing iridium oxide loading can be noted, suggesting a decrease in the number of available reaction sites.

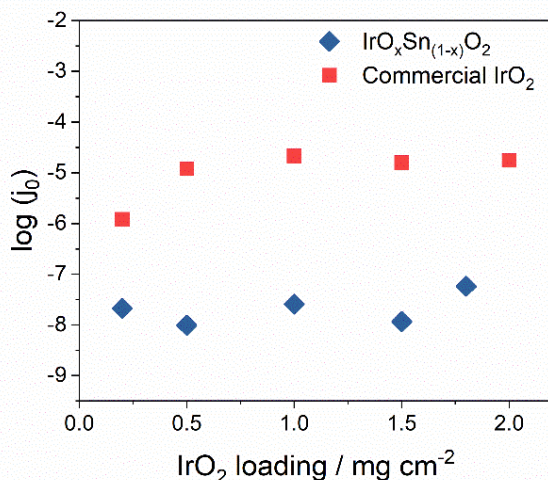


Figure 2.11: Logarithm of the exchange current density determined from  $iR$ -free Tafel plots as a function of  $\text{IrO}_2$  loading for  $\text{Ir}_x\text{Sn}_{(1-x)}\text{O}_2$  and commercial  $\text{IrO}_2$  MEAs.

For similar  $\text{IrO}_2$  loadings,  $\text{Ir}_x\text{Sn}_{(1-x)}\text{O}_2$  MEAs exhibited approximately 100 mV higher mass transport overpotentials to reach  $2 \text{ A cm}^{-2}$  current density compared to commercial  $\text{IrO}_2$  catalysts (Figure 2.12). These differences could be caused by differences in porosity of the catalyst layer. Typically, ink formulations and ionomer content have an influence on catalyst layer porosity. As we focused solely on catalyst composition variation, other parameters were kept the same. It is possible that differences in crystallite morphology of  $\text{Ir}_x\text{Sn}_{(1-x)}\text{O}_2$  powders compared to commercial  $\text{IrO}_2$  lead to changes in catalyst layer porosity. Optimization of parameters like ionomer content in catalyst inks or hot pressing could improve mass transport overpotentials.

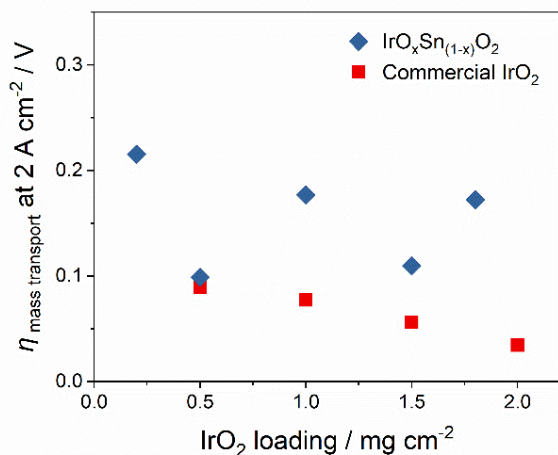


Figure 2.12: Mass transport overpotential at  $2 \text{ A cm}^{-2}$  current density as a function of  $\text{IrO}_2$  loading for  $\text{Ir}_x\text{Sn}_{(1-x)}\text{O}_2$  and commercial  $\text{IrO}_2$  MEAs.

Stability experiments for  $\text{Ir}_x\text{Sn}_{(1-x)}\text{O}_2$  MEAs indicated performance loss increases with  $\text{SnO}_2$  content in the samples (Figure 2.13). One of potential causes could be  $\text{SnO}_2$  leaching from the catalyst, as reported by Geiger et al. for doped tin oxide supports.<sup>18</sup>

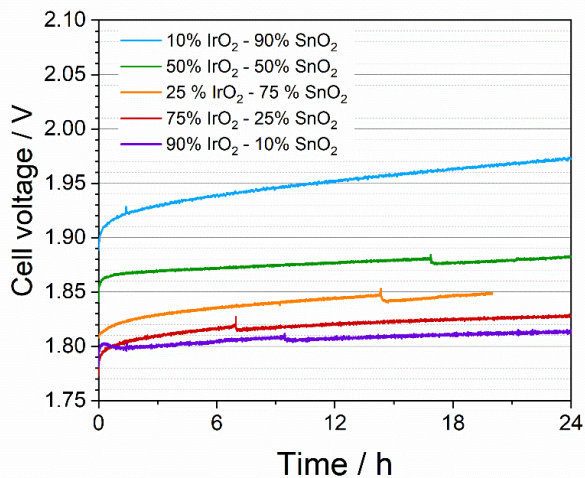


Figure 2.13: Chronopotentiometry experiments at  $1 \text{ A cm}^{-2}$  current density for  $\text{Ir}_x\text{Sn}_{(1-x)}\text{O}_2$  MEAs.

## 2.4 Conclusions

In summary, the performance of Ir<sub>x</sub>Sn<sub>(1-x)</sub>O<sub>2</sub> MEAs is inferior to commercial IrO<sub>2</sub> MEAs due to a combination of effects: higher Ohmic resistance, poorer intrinsic catalytic activity, and hindered mass transport through the catalyst layer. The Ohmic and mass transport overpotential at higher cell voltage could be reduced in principle by the addition of a conductive material or by the optimization of catalyst layer deposition methods. Nevertheless, the lower intrinsic catalytic activity of Ir<sub>x</sub>Sn<sub>(1-x)</sub>O<sub>2</sub> powders prepared by SCS is a factor which cannot be improved easily, making the mixed Ir-Sn oxides unsuitable for commercial application as OER catalysts.

## 2.5 References

1. IEA, *The Future of Hydrogen*, ed. Paris, 2019.
2. M. Carmo, D. L. Fritz, J. Mergel and D. Stolten, *Int. J. Hydrogen Energy*, 2013, **38**, 4901.
3. M. G. Chourashiya and A. Urakawa, *J. Mater. Chem. A*, 2017, **5**, 4774.
4. J. Xu, G. Liu, J. Li and X. Wang, *Electrochim. Acta*, 2012, **59**, 105.
5. H.-S. Oh, H. N. Nong, T. Reier, A. Bergmann, M. Gliech, J. Ferreira de Araújo, E. Willinger, R. Schlögl, D. Teschner and P. Strasser, *J. Am. Chem. Soc.*, 2016, **138**, 12552.
6. V. A. Saveleva, L. Wang, O. Kasian, M. Batuk, J. Hadermann, J. J. Gallet, F. Bournel, N. Alonso-Vante, G. Ozouf, C. Beauger, K. J. J. Mayrhofer, S. Cherevko, A. S. Gago, K. A. Friedrich, S. Zafeiratos and E. R. Savinova, *ACS Catal.*, 2020, **10**, 2508.
7. A. Varma, A. S. Mukasyan, A. S. Rogachev and K. V. Manukyan, *Chem. Rev.*, 2016, **116**, 14493.
8. A. Marshall, B. Børresen, G. Hagen, M. Tsytkin and R. Tunold, *Mater. Chem. Phys.*, 2005, **94**, 226.
9. A. Marshall, B. Børresen, G. Hagen, M. Tsytkin and R. Tunold, *Electrochim. Acta*, 2006, **51**, 3161.

10. G. Li, H. Yu, D. Yang, J. Chi, X. Wang, S. Sun, Z. Shao and B. Yi, *J. Power Sources*, 2016, **325**, 15.
11. V. M. Goldschmidt, *Naturwissenschaften*, 1926, **14**, 477.
12. W. H. Baur and A. A. Khan, *Acta Crystallographica Section B*, 1971, **27**, 2133.
13. C. Rozain, E. Mayousse, N. Guillet and P. Millet, *Appl. Catal. B*, 2016, **182**, 153.
14. D. S. Falcão and A. M. F. R. Pinto, *Journal of Cleaner Production*, 2020, **261**, 121184.
15. T. Schuler, T. J. Schmidt and F. N. Büchi, *J. Electrochem. Soc.*, 2019, **166**, F555.
16. E. T. Ojong, J. T. H. Kwan, A. Nouri-Khorasani, A. Bonakdarpour, D. P. Wilkinson and T. Smolinka, *Int. J. Hydrogen Energy*, 2017, **42**, 25831.
17. M. Bernt, A. Siebel and H. A. Gasteiger, *J. Electrochem. Soc.*, 2018, **165**, F305.
18. E. Oakton, D. Lebedev, A. Fedorov, F. Krumeich, J. Tillier, O. Sereda, T. J. Schmidt and C. Copéret, *New J. Chem.*, 2016, **40**, 1834.
19. Y. Zhao, N. M. Vargas-Barbosa, E. A. Hernandez-Pagan and T. E. Mallouk, *Small*, 2011, **7**, 2087.
20. T. Shinagawa, A. T. Garcia-Esparza and K. Takanebe, *Scientific Reports*, 2015, **5**, 13801.
21. S. Song, H. Zhang, B. Liu, P. Zhao, Y. Zhang and B. Yi, *Electrochem. Solid-State Lett.*, 2007, **10**, B122.
22. S. Geiger, O. Kasian, A. M. Mingers, K. J. J. Mayrhofer and S. Cherevko, *Scientific Reports*, 2017, **7**, 4595







# 3

## **Nanostructured Sn-Ir oxygen evolution catalysts prepared by a coprecipitation deposition method with superior activity in PEM electrolysis cells**

### **Abstract**

In this chapter, the influence of nanostructures and interaction of Sn and Ir in oxygen evolution catalysts in a polymer electrolyte membrane electrolysis cell was investigated. For this aim, the precipitation-deposition method with sodium borohydride reduction was evaluated as the method to prepare the nanostructures. Sn addition to Ir-based oxygen evolution reaction catalysts has been reported to yield materials with higher activity; this was also observed for Sn/Ir catalysts prepared by the precipitation-deposition method. The nano-layer of Sn/SnO<sub>2</sub> deposited over metallic Ir particles enhances the interfacial contacts, resulting in synergistic interactions. By deconvoluting the polarization curves into constituting contributions, the reason for performance improvement can be attributed to the higher exchange current density of the Sn/Ir powder as consequences of a higher intrinsic catalytic activity and/or a higher number of surface reaction sites.

This chapter is based on the following publication:

S. Bunea, P. Zeng, M. G. Willinger, A. Urakawa, *under review*.

### 3.1 Introduction

Electricity generation from renewable wind and solar energy has steadily increased in the last decade.<sup>1</sup> Nevertheless, greater efforts are required for renewable energy sources to become the primary energy sources for humanity. One of the major challenges toward achieving this ambitious goal is the intermittent nature of solar and wind energy, which is often asynchronous with the electricity demand. The adoption of a “hydrogen economy” could represent a solution to mitigate the aforementioned challenges.<sup>2</sup> In such an approach, electrical energy can be converted into chemical energy via water electrolysis. This yields hydrogen, which can be stored and used on demand for electricity production via fuel cells or simply clean combustion producing only water.

PEM electrolysis possesses a series of advantages over alkaline electrolysis, which makes it particularly attractive for commercial implementation. Some representative advantages are (i) high faradaic efficiency due to low gas crossover rate between cathode and anode compartments, (ii) ability to operate at high current densities, (iii) low Ohmic resistance, (iv) robust and compact cell design and (v) possibility of yielding hydrogen at elevated pressures.<sup>3</sup> Although a decrease in PEM electrolyser price has been witnessed over the past 30 years, a few drawbacks still limit the wide applicability of PEM technology.<sup>4</sup> One of the most important limitations is the need for costly and scarce noble metal electrocatalysts such as platinum, ruthenium and/or iridium. Particularly, replacing the state-of-the-art iridium as anode electrocatalyst in PEM electrolyzers has proved to be difficult, as the requirements for alternative catalyst candidates are not only limited to high activity towards OER (Eq. 3.1), but also demand long-term stability in the acidic anodic environment of the PEM electrolyser. The main efforts in the scientific community regarding the anode side of PEM electrolyzers are focused on improving iridium dispersion by using various support materials, engineering the catalyst layer morphology to increase surface area, porosity, and contact resistance between components, employing core-shell structures with reduced iridium content, and decreasing catalyst particle size.<sup>5-15</sup>



Out of various support materials proposed in literature, antimony-doped tin oxide (ATO) has been investigated extensively, as it provides good electric conductivity and stability in

anodic conditions.<sup>16-18</sup> Furthermore, recent reports suggest that the tin (IV) oxide does not merely play the role of a support, but rather it takes part in electrocatalysis.<sup>19-21</sup>

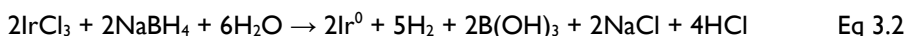
In this chapter, we examine potential synergies of Ir and Sn for OER in a PEM electrolyser. We employ the precipitation-deposition synthesis for the preparation of catalysts. In contrast to most of the literature studies based on the deposition of the active iridium metal over a tin oxide/antimony-doped tin oxide support, we take an opposite approach by depositing tin over iridium nanoparticles.<sup>6, 7, 16, 17</sup> In this way, the active Ir surface is expected to be covered with SnO<sub>2</sub> and should point out the existence of the synergy. We show how Ir interacts with SnO<sub>2</sub> on the nanoscale matters and the synergy of Ir and Sn interactions for OER.

## 3.2 Experimental

### 3.2.1 Catalyst synthesis

Sn/Ir powders were synthesized via the precipitation-deposition method. In the first step, iridium black powder was prepared according to the procedure described in literature.<sup>22</sup>

The IrCl<sub>3</sub>·xH<sub>2</sub>O (Precious Metals Online, 99%) precursor was dissolved in 100 mL water. The amount of iridium salt was calculated, so that approximately 200 mg of iridium black powder is obtained. The solution pH was brought to 13 by addition of 0.5 M KOH. After stirring the solution for 30 minutes, ensuring that the iridium precursor has completely dissolved, a 6-fold molar excess of sodium borohydride powder was added to the flask. Bubble formation was observed immediately after the addition of NaBH<sub>4</sub> (Acros Organics, 99%). The decomposition of sodium borohydride in water releases hydrogen, which reduces Ir<sup>3+</sup> ions to metallic iridium. The flask was stirred for approximately 1 h until bubble formation was no longer observed. This was accompanied by the disappearance of the yellow color of the IrCl<sub>3</sub> of the solution and the formation of a black precipitate powder. The reduction reaction that took place during the synthesis follows Eq. 3.2.



Subsequently, the black powder was thoroughly washed by filtration with approximately 2 L of type I ultrapure water to remove any soluble residues. The powder was dried at 120 °C overnight.

In the second step, the iridium black powder was suspended in 100 mL ultrapure water in a flask.  $\text{SnCl}_4 \cdot 5\text{H}_2\text{O}$  (Sigma Aldrich, 99.995%) was added and the flask was stirred until complete dissolution of  $\text{SnCl}_4 \cdot 5\text{H}_2\text{O}$ . The flask was transferred to an ultrasonic bath and  $\text{NaBH}_4$  powder was slowly added. The reaction follows Eq. 3.3.



When gas evolution was no longer observed, the powder was washed with 2 L of milliQ water and dried at 120 °C overnight.

### 3.2.2 Catalyst characterization

$\text{N}_2$  physisorption experiments were performed using a Micromeritics Tristar 3020 setup after an overnight degassing step at 150 °C. X-ray diffractograms (XRD) of the powders were recorded with a Bruker D8 Discover powder diffractometer with a Co K-alpha radiation source. Scanning electron micrographs (SEM) were recorded with a JEOL 6010 microscope. Transmission electron micrographs (TEM) were recorded using a JEOL Grand ARM “Vortex”.

### 3.2.3 Catalyst-coated membrane preparation and cell assembly

The catalyst-coated membrane (CCM) preparation procedure is similar to that described in Chapter 2.

### 3.2.4 Electrochemical experiments

The setup used for electrochemical measurements is the same as the one reported in Chapter 2.

## 3.3 Results and discussion

To investigate the promotional effect of Sn in Ir-based OER catalysts further, we explored different types of catalyst powders. The focus was switched from iridium oxide to metallic iridium, which is not as active as iridium oxide but provides satisfactory performance in OER. In our approach, we steered away from commonly reported methods in which the active iridium/iridium oxide component is deposited over the support material ( $\text{SnO}_2$ , antimony tin oxide, indium tin oxide, etc.).<sup>7, 20, 23, 24</sup> Instead, we started with iridium black (i.e., metallic Ir) powder, over which we deposited tin via the precipitation-deposition

method. In the anodic conditions of the PEM electrolyser, the deposited Sn would eventually oxidize to SnO<sub>2</sub>. With this nanostructured Ir-Sn composite, the promotional effect of SnO<sub>2</sub> on iridium-based OER catalysts, which was reported in literature but was not observed for Ir<sub>x</sub>Sn<sub>(1-x)</sub>O<sub>2</sub> MEAs, will be investigated further. The approach could lead to an enhancement of the Ir-Sn contact without the formation of a mixed oxide of solid-solutions, since the synthesis method we adopted yields Sn ensembles on the surface of iridium black particles.

With these in mind, we synthesized a series of catalysts with 5, 7, 10, 15, 20, 30, 50, and 90 wt% Sn coated over Ir black (denoted as Sn/Ir). We prepared and tested the Sn/Ir MEAs with 2 mg cm<sup>-2</sup> catalyst loading, containing iridium loadings of 1.9, 1.86, 1.8, 1.7, 1.6, 1.4, 1, and 0.2 mg cm<sup>-2</sup>, respectively. For the sake of comparison and in order to observe the effect of Sn addition, we also tested a series of MEAs containing solely iridium black powder with loadings of 0.2, 0.5, 0.7, 1, 1.5 and 2 mg cm<sup>-2</sup>.

### 3.3.1 Sn/Ir catalysts – Catalyst characterization

X-ray diffraction patterns of Sn/Ir catalysts exhibit reflections which are specific to metallic iridium (Figure 3.1). The Ir crystallite size determined using Scherrer equation is approximately 3 nm. No peaks characteristic to Sn or SnO<sub>2</sub> could be observed for the powders with Sn loading up to 20%. This indicates that Sn/SnO<sub>2</sub> is present in an amorphous phase or in a very small crystallite size, and thus not detectable by X-ray diffraction. Only for the catalyst with the highest Sn loading, 90 wt%, broad peaks characteristic to SnO<sub>2</sub> were detected. This suggests that only at very high loadings Sn/SnO<sub>2</sub> crystallizes with a long-range order, although the crystallite size is very small (approximately 2 nm).

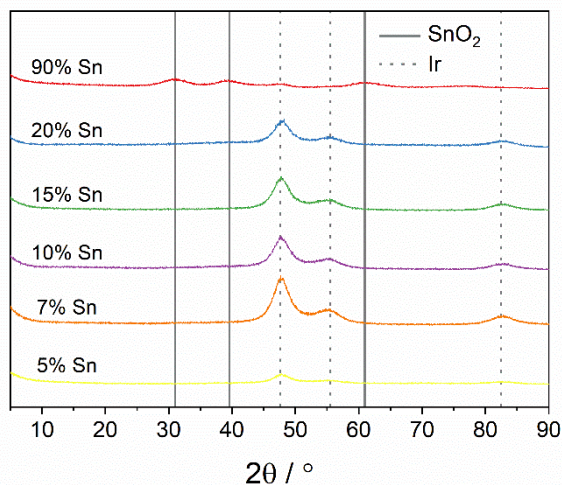


Figure 3.1: X-ray diffraction patterns of Sn/Ir powders.

Agglomerates consisting of  $<5$  nm crystallites and an amorphous phase were observed in transmission electron micrographs (Figure 3.2, 3.3). Energy dispersive X-ray spectra in Figure 3.3 reveal the presence of both iridium and tin in the sample. Both iridium and tin were detected by the elemental mapping, and Figure 3.3 shows high dispersion of the two elements in the amorphous phase. A good contact between the two elements was therefore achieved.

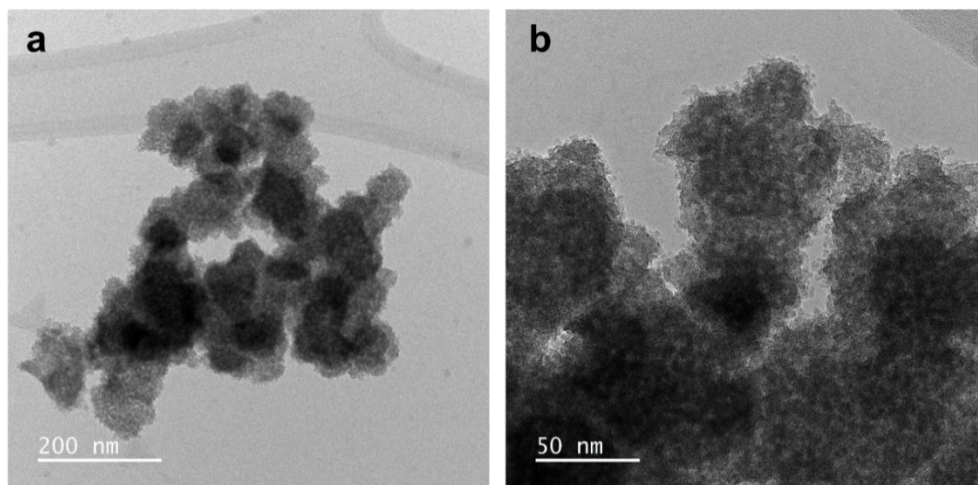


Figure 3.2: Transmission electron micrographs of the 10%Sn/90%Ir catalyst powder.

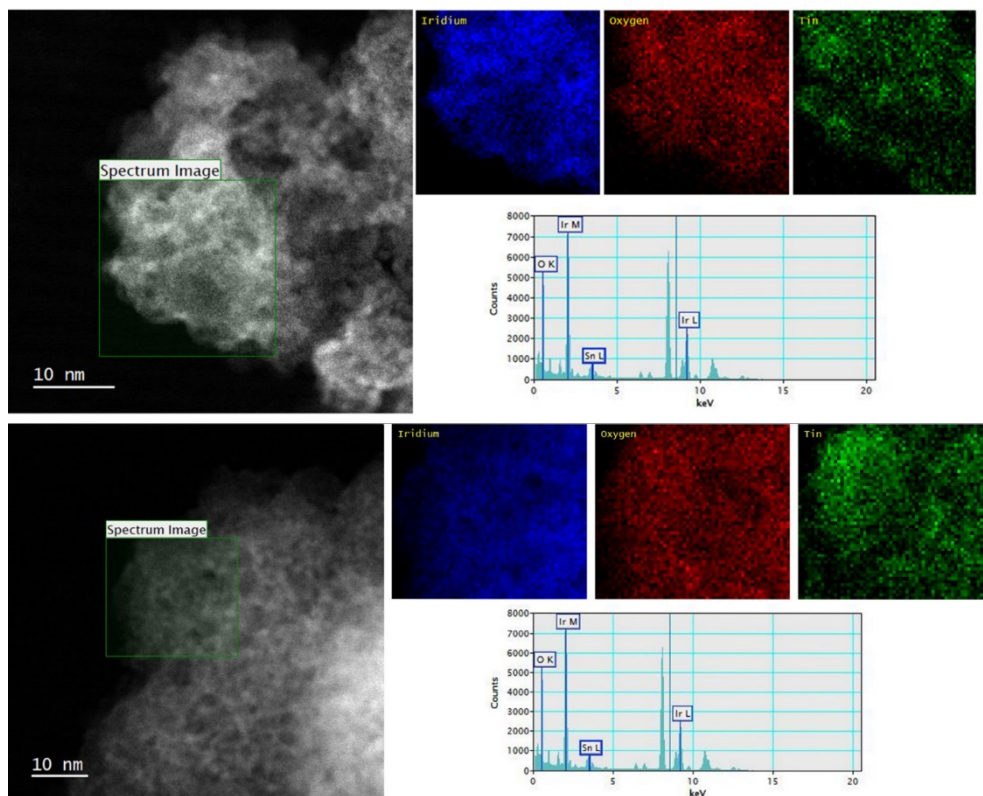


Figure 3.3: High resolution transmission electron micrographs of 10%Sn/90%Ir, elemental maps for Ir, O and Sn and the corresponding EDS spectrum.

In order to clarify the composition of the crystallites present in the sample, we calculated *d*-spacing of crystalline regions from high resolution transmission electron micrographs, revealing the presence of iridium, tin, iridium oxide and tin oxide (Figures 3.4-3.6). Lattice fringe distances were determined by performing inverse fast Fourier transformation (IFFT) of the areas, for example, marked in red in Figure 3.4, yielding the corresponding diffraction patterns (column A in Figure 3.4). Fast Fourier transform (FFT) performed on the diffraction patterns resulted in the reconstructed image (e.g., column B in Figure 3.4). Areas 1 and 2 in Figure 3.4 correspond to the IrO<sub>2</sub> (110) phase, with a distance between lattice fringes of 0.32 nm. In areas 3 and 4 in Figure 3.4, the determined lattice fringe distance was 0.34 nm, corresponding to the SnO<sub>2</sub> (110) phase. The (200) phase of SnO<sub>2</sub>, with a lattice fringe distance of 0.24 nm and the (211) phase of Sn, with a lattice fringe distance of 0.20 nm were also identified (Figure 3.5, 3.6). The preparation of the catalysts did not involve any



oxidations steps and metallic iridium is not expected to oxidize under ambient conditions. However, given the high surface area of the materials and the fact that the samples were not stored under an inert atmosphere, the formation of an oxide at nanometric scale is possible. Furthermore, TEM experiments were conducted at a later time compared to XRD, which might explain why  $\text{IrO}_2$  crystallites were not identified in XRD patterns. On the other hand, Sn forms a protective oxide layer on the surface, preventing its further oxidation.

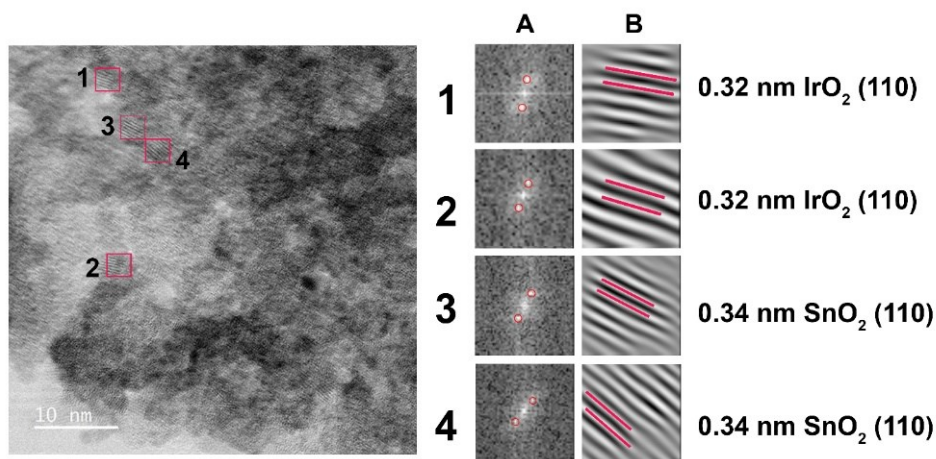


Figure 3.4: High resolution transmission electron micrograph of 10 wt% Sn/Ir catalyst, calculated  $d$ -spacing and the corresponding plane for selected areas.

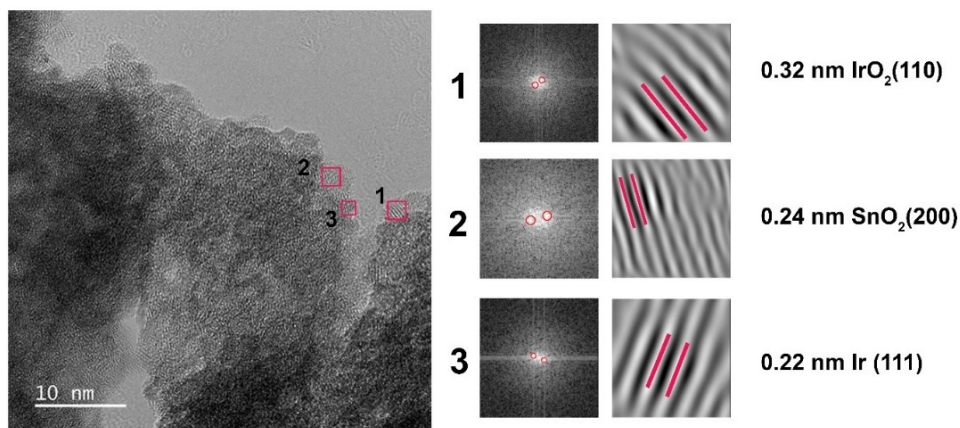


Figure 3.5: High resolution transmission electron micrograph of 10%Sn/Ir catalyst, calculated  $d$ -spacing and the corresponding plane for selected areas.

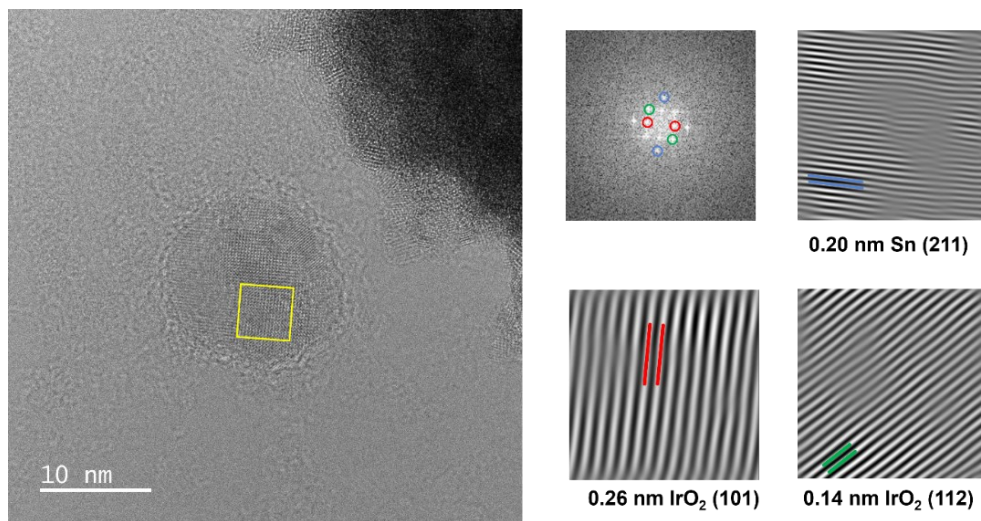


Figure 3.6: High resolution transmission electron micrograph of 10%Sn/Ir catalyst, calculated  $d$ -spacing and the corresponding plane for selected area.

### 3.3.2 Sn/Ir catalysts – PEM cell performance and overpotential analysis

Polarization curves in PEM water electrolysis using the Sn/Ir catalysts at the anode were recorded in the 1.3-2.2 V cell voltage range (Figure 3.7). The most notable observation in the polarization curves is that the addition of Sn leads to higher current density at the same cell voltage compared to Ir black MEAs with similar Ir loadings.

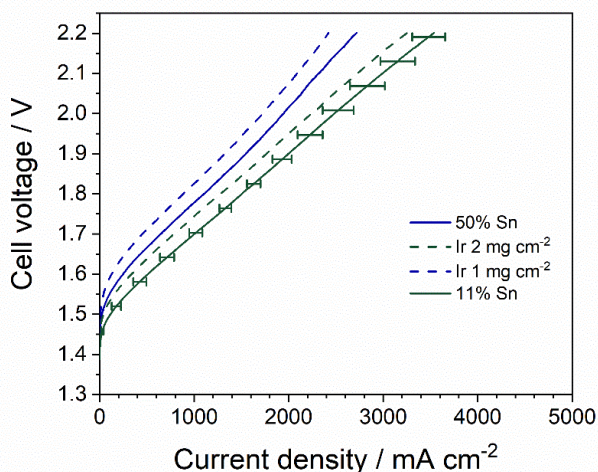


Figure 3.7: Polarization curves of Sn/Ir MEAs and Ir black MEAs, 0.75 mg cm<sup>-2</sup> 40 wt% Pt/C cathode catalyst, Nafion 115, 80 °C.

For gaining further insights into the underlying causes of the performance enhancement due to Sn addition, we performed an overpotential analysis (Figures 3.8-3.10).

The Ohmic resistance of iridium black MEAs is found to be almost independent of Ir loading (Figure 3.8). Sn/Ir MEAs exhibit slightly lower Ohmic resistance at higher Ir loading. Nevertheless, the difference in the Ohmic resistance values between the Sn/Ir MEAs and Ir black MEAs is small.

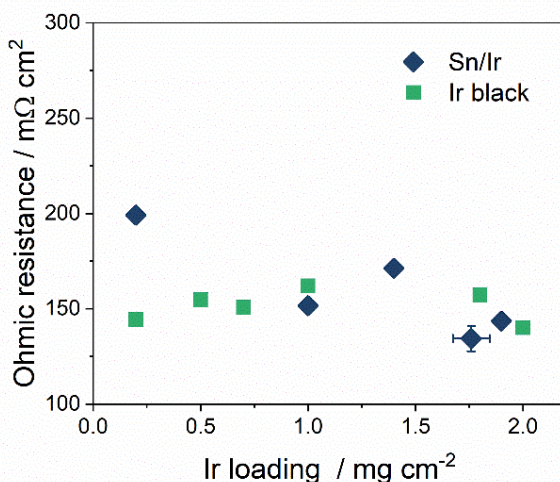


Figure 3.8: Ohmic resistance determined by EIS as a function of iridium loading for Sn/Ir and Ir black MEAs.

Looking at the kinetic overpotential, both the apparent Tafel slopes of the Sn/Ir MEAs and iridium black MEAs display similar values of 39-40  $\text{mV dec}^{-1}$  (Table 3.1), in agreement with literature values, suggesting that oxygen evolution follows the same reaction mechanism for both types of catalysts. The MEAs with the highest tin loading (90 wt%) and equivalent Ir loading of iridium black ( $0.2 \text{ mg cm}^{-2}$ ) show significantly higher Tafel slope and represent an exception (Table 3.1). The higher apparent Tafel slope observed does not necessarily point to a different reaction mechanism. However, as reported by Bernt et al., it could suggest additional voltage losses for the very thin and inhomogeneous catalyst layer, which we also visually observed during MEA preparation.<sup>25</sup> Additionally, it is possible that the Pt-coated titanium GDLs were partially in contact with the Nafion membrane directly, particularly for

the 90 wt% Sn MEA due to the thin catalyst layer, and might have exhibited some OER catalytic activity themselves, altering the value of the apparent Tafel slope.

Table 3.1: Kinetic parameters determined from Tafel plot analysis and Ohmic resistance recorded by EIS for Sn/Ir and iridium black MEAs.

MEA	Apparent Tafel slope (mV dec <sup>-1</sup> )	log j <sub>0</sub>	R <sub>el</sub> (Ω cm <sup>2</sup> )
5%Sn/Ir	39.28	-5.25	143.6
7%Sn/Ir	39.42	-5.53	145.2
10%Sn/Ir	39.23	-6.03	136.4
15%Sn/Ir	39.42	-5.53	134.8
20%Sn/Ir	39.22	-5.35	134.4
50%Sn/Ir	39.57	-6.48	151.6
90%Sn/Ir	67.63	-6.56	193.6
Iridium black 2 mg cm <sup>-2</sup>	39.54	-6.27	140.0
Iridium black 1.5 mg cm <sup>-2</sup>	39.64	-6.46	156.0
Iridium black 1 mg cm <sup>-2</sup>	39.72	-7.15	162.0
Iridium black 0.5 mg cm <sup>-2</sup>	39.74	-6.99	154.8
Iridium black 0.2 mg cm <sup>-2</sup>	50.50	-6.75	178.8

The exchange current density displayed by Sn/Ir MEAs with <30 wt% Sn catalysts is one order of magnitude higher compared to iridium black MEAs (Figure 3.9), illustrating the strong promotional effect of Sn in the OER reaction. It is difficult to make conclusions on the mechanism of Sn promotion solely based on polarization curves in the PEM cell. Saveleva et al. proposed a mechanism involving oxygen spill-over from Ir to SnO<sub>2</sub> for the enhanced performance of antimony-doped tin oxide-supported iridium catalysts based on near-ambient pressure X-ray photoelectron spectroscopy (NAP-XPS) studies.<sup>20</sup> Although a different synthesis approach was used to obtain the catalysts, it is likely that the promotion follows the proposed mechanism involving oxygen spill-over. The exchange current density decreases slightly with iridium loading on both types of MEAs, which can be attributed to the decrease in active catalyst surface area, leading to a lower number of surface reaction sites.

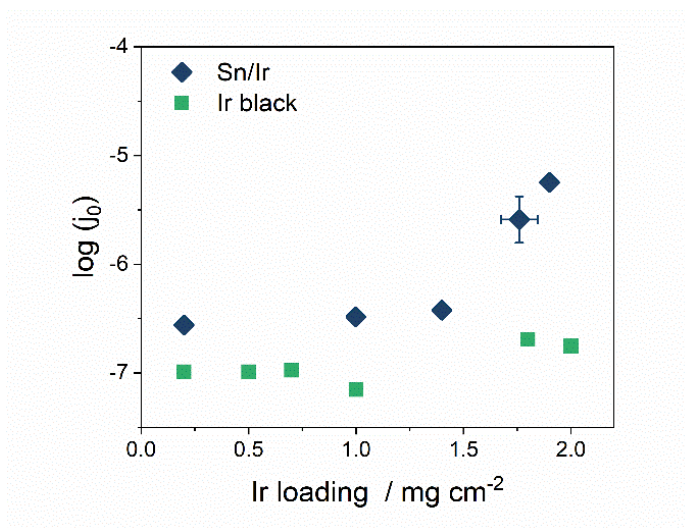


Figure 3.9: Logarithm of the exchange current density determined from  $iR$ -free Tafel plots as a function of iridium loading for Sn/Ir and Ir black MEAs.

Figure 3.10 shows no effect of Sn addition on mass transport overpotentials, and a similar range of mass transport overpotential (100-150 mV) as recorded at  $2 \text{ A cm}^{-2}$  current density for both Sn/Ir and Ir black MEAs.

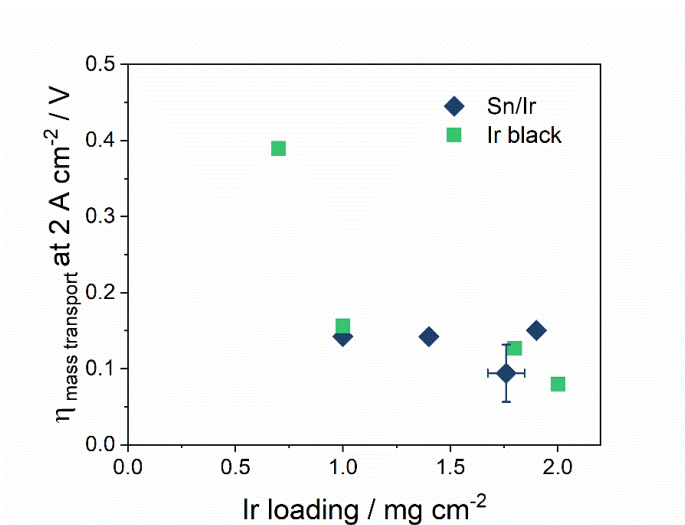


Figure 3.10: Mass transport overpotential at  $2 \text{ A cm}^{-2}$  current density as a function of  $\text{IrO}_2$  loading for Sn/Ir and Ir black MEAs.

Furthermore, the stability of the nanostructured Sn/Ir catalyst was investigated. Chronopotentiometry experiments at  $1 \text{ A cm}^{-2}$  for 24 h were conducted to investigate how the stability of the 10 wt% Sn/Ir catalyst compares to Ir black (Figure 3.11). No increase in cell voltage could be observed during the experiments, showing that 10% Sn addition does not affect the long-term stability of the MEA.

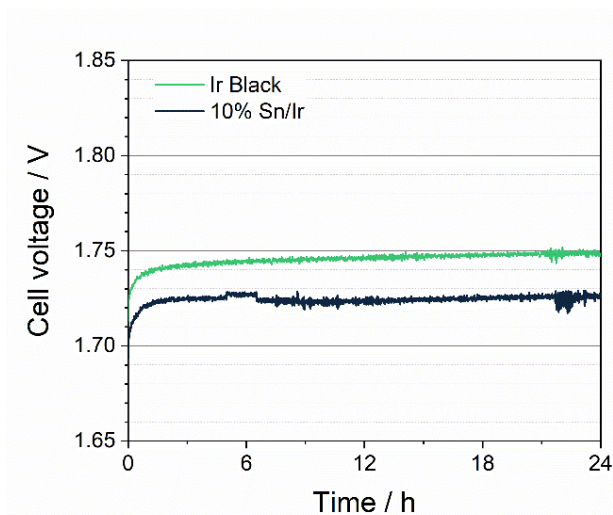


Figure 3.11: Chronopotentiometry experiments at  $1 \text{ A cm}^{-2}$  current density for a 10%Sn/Ir and Ir black MEAs.

To summarize, we were able to prepare iridium tin OER catalysts which valorize the promotional effect induced by the tin addition. The primary parameters at which the Sn/Ir MEAs excel are the lower kinetic overpotential and improved mass transport and, to a lesser extent, the lower Ohmic resistance compared to iridium black MEAs. A tin loading of around 11 wt% appears to be the optimum for achieving the superior performance with excellent long-term stability. MEAs with tin loadings higher than 20 wt% exhibited exchange current densities of one order of magnitude lower. It is possible that at high tin loadings, the surface of iridium particles becomes covered with tin oxide to a level at which the promotional effect is counterbalanced by a lower availability of surface sites.

### 3.4 Conclusions

In this work, we synthesized a series of Sn/Ir OER catalysts by a precipitation-deposition method with sodium borohydride reduction of Ir and Sn precursors. The goal of the study

was to investigate whether addition of tin to iridium-based catalysts improves the cell performance, and to elucidate the structural factors to induce Sn-Ir synergistic effects. Sn/Ir MEAs performed better than the counterpart, i.e., iridium black MEAs. The main contribution to the increased performance is the higher exchange current density for Sn/Ir MEAs, which suggests a higher intrinsic catalytic activity by inducing a higher degree of iridium utilization, a higher number of available surface reaction sites or a creation of highly active interfacial sites. Sn addition did not affect the mass transport overpotentials of the MEAs. Further *operando* investigations on these catalysts are required to confirm or disprove this hypothesis, which we will cover in our future works on the subject. Our results illustrate that the catalyst synthesis method, spatial distribution and mixing of Sn and Ir and the oxidation state of iridium is crucial to inducing Sn-Ir synergy.

### 3.5 References

1. Global Energy Review 2020, <https://www.iea.org/reports/global-energy-review-2020>, (accessed January, 2022)
2. J. O. M. Bockris, *Int. J. Hydrogen Energy*, 2002, **27**, 731.
3. M. Carmo, D. L. Fritz, J. Mergel and D. Stolten, *Int. J. Hydrogen Energy*, 2013, **38**, 4901.
4. S. M. Saba, M. Müller, M. Robinius and D. Stolten, *Int. J. Hydrogen Energy*, 2018, **43**, 1209.
5. E. Oakton, D. Lebedev, M. Povia, D. F. Abbott, E. Fabbri, A. Fedorov, M. Nachttegaal, C. Copéret and T. J. Schmidt, *ACS Catal.*, 2017, **7**, 2346.
6. D. Böhm, M. Beetz, M. Schuster, K. Peters, A. G. Hufnagel, M. Döblinger, B. Böller, T. Bein and D. Fattakhova-Rohlfing, *Adv. Funct. Mater.*, 2020, **30**, 1906670.
7. A. Hartig-Weiss, M. Miller, H. Beyer, A. Schmitt, A. Siebel, A. T. S. Freiberg, H. A. Gasteiger and H. A. El-Sayed, *ACS Applied Nano Materials*, 2020, **3**, 2185.
8. J. E. Park, S. Kim, O.-H. Kim, C.-Y. Ahn, M.-J. Kim, S. Y. Kang, T. I. Jeon, J.-G. Shim, D. W. Lee, J. H. Lee, Y.-H. Cho and Y.-E. Sung, *Nano Energy*, 2019, **58**, 158.

9. F. Hegge, F. Lombeck, E. Cruz Ortiz, L. Bohn, M. von Holst, M. Kroschel, J. Hübner, M. Breitwieser, P. Strasser and S. Vierrath, *ACS Applied Energy Materials*, 2020, **3**, 8276.
10. C. Rozain, E. Mayousse, N. Guillet and P. Millet, *Appl. Catal. B*, 2016, **182**, 123.
11. J. Polonský, R. Kodým, P. Vágner, M. Paidar, B. Bensmann and K. Bouzek, *J. Appl. Electrochem.*, 2017, **47**, 1137.
12. C. V. Pham, M. Bühler, J. Knöppel, M. Bierling, D. Seeberger, D. Escalera-López, K. J. J. Mayrhofer, S. Cherevko and S. Thiele, *Appl. Catal. B*, 2020, **269**, 118762.
13. H. N. Nong, L. Gan, E. Willinger, D. Teschner and P. Strasser, *Chemical Science*, 2014, **5**, 2955.
14. S. Siracusano, V. Baglio, A. Stassi, R. Ornelas, V. Antonucci and A. S. Aricò, *Int. J. Hydrogen Energy*, 2011, **36**, 7822.
15. J. Lim, D. Park, S. S. Jeon, C.-W. Roh, J. Choi, D. Yoon, M. Park, H. Jung and H. Lee, *Adv. Funct. Mater.*, 2018, **28**, 1704796.
16. G. Liu, J. Xu, Y. Wang and X. Wang, *J. Mater. Chem. A*, 2015, **3**, 20791.
17. H.-S. Oh, H. N. Nong, T. Reier, M. Gliech and P. Strasser, *Chemical Science*, 2015, **6**, 3321.
18. S. Geiger, O. Kasian, A. M. Mingers, K. J. J. Mayrhofer and S. Cherevko, *Scientific Reports*, 2017, **7**, 4595.
19. H.-S. Oh, H. N. Nong, T. Reier, A. Bergmann, M. Gliech, J. Ferreira de Araújo, E. Willinger, R. Schlögl, D. Teschner and P. Strasser, *J. Am. Chem. Soc.*, 2016, **138**, 12552.
20. V. A. Saveleva, L. Wang, O. Kasian, M. Batuk, J. Hadermann, J. J. Gallet, F. Bournel, N. Alonso-Vante, G. Ozouf, C. Beauger, K. J. J. Mayrhofer, S. Cherevko, A. S. Gago, K. A. Friedrich, S. Zafeiratos and E. R. Savinova, *ACS Catal.*, 2020, **10**, 2508.
21. J. Xu, G. Liu, J. Li and X. Wang, *Electrochim. Acta*, 2012, **59**, 105.



22. S. A. Grigoriev, P. Millet, K. A. Dzhus, H. Middleton, T. O. Saetre and V. N. Fateev, *Int. J. Hydrogen Energy*, 2010, **35**, 5070.
23. D. Lebedev, R. Ezhov, J. Heras-Domingo, A. Comas-Vives, N. Kaeffer, M. Willinger, X. Solans-Monfort, X. Huang, Y. Pushkar and C. Copéret, *ACS Cent. Sci.*, 2020, **6**, 1189.
24. G. C. da Silva, S. I. Venturini, S. Zhang, M. Löffler, C. Scheu, K. J. J. Mayrhofer, E. A. Ticianelli and S. Cherevko, *ChemElectroChem*, 2020, **7**, 2330.
25. M. Bernt, A. Siebel and H. A. Gasteiger, *J. Electrochem. Soc.*, 2018, **165**, F305.





# 4

## **Electrified conversion of contaminated water to value: selective conversion of aqueous nitrate to ammonia in a PEM cell**

### **Abstract**

The application of a polymer electrolyte membrane electrolytic cell for continuous conversion of nitrate, one of the contaminants in water, to ammonia at the cathode was explored in the present work. Among carbon-supported metal (Cu, Ru, Rh and Pd) electrocatalysts, the Ru-based catalyst showed the best performance. By suppressing the competing hydrogen evolution reaction at the cathode, we were able to reach 94% faradaic efficiency for nitrate reduction towards ammonium. We show the importance of matching the rate of the anodic reaction with the cathodic reaction to achieve high faradaic efficiency. By recirculating the effluent stream, 93% nitrate conversion was achieved in 8 h of constant current electrolysis at  $10 \text{ mA cm}^{-2}$  current density. The presented approach offers a promising path towards precious  $\text{NH}_3$  production from nitrate-containing water which needs purification, or which can be obtained after the capture of gaseous  $\text{NO}_x$  pollutants into water, leading to waste to value conversion.

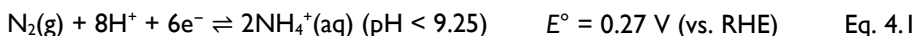
This chapter is based on the following publication:

S. Bunea, K. Clemens, A. Urakawa, *ChemSusChem* 2022, 15, e202102180.

## 4.1 Introduction

NH<sub>3</sub> production by the Haber-Bosch process is the main pillar of the fertilizer manufacturing industry. About 170 million tons of ammonia are produced yearly, and in 2008, nitrogen-containing fertilizers derived from NH<sub>3</sub> were responsible for feeding 48% of the world's population.<sup>1,2</sup> It is predicted that crop production needs to be increased by 100% by 2050 to meet the global food demand and so does the ammonia production capacity.<sup>3</sup> However, the widely practiced Haber-Bosch process is unsustainable due to the use of hydrogen originating from fossil fuel and the energy-intensive steam reforming process to produce hydrogen.<sup>4</sup> As a consequence, CO<sub>2</sub> emissions associated with the Haber-Bosch process account for 1% of the global annual CO<sub>2</sub> emissions.<sup>5</sup> The process can be made greener when the hydrogen is produced using renewable energy. Still, there is a relatively large intrinsic energy requirement of the process due to the high temperature and high pressure conditions of the Haber-Bosch process.

With increasing availability of renewable and natural energy sources which are accessible as electric power in most processes, the electrochemical synthesis of ammonia from nitrogen (Eq. 4.1) has attracted significant attention in the last decade.<sup>1,6-13</sup> Nevertheless, the reported product yields are still far from industrial relevance, due to challenges related to nitrogen activation.



Besides, there is another issue associated with increasing ammonia production. The use of nitrogen-containing fertilizers has led to an increase of nitrate ion (simply called nitrate or NO<sub>3</sub><sup>-</sup>) concentration in the soil and groundwater. It has to be removed to prevent eutrophication and consequences to human health (e.g., methemoglobinemia). Furthermore, highly polluting nitrate-containing waste streams are generated from various industrial processes such as uranium purification, saltpeter mining and metal finishing, where the abatement of the contaminants is crucial to minimize the environmental impacts.<sup>14</sup>

In this regard, electrochemical conversion of nitrate to ammonia, which can be present as ammonium ion (simply called ammonium or NH<sub>4</sub><sup>+</sup>) in water (Eq. 4.2), offers a unique solution to this problem because of the possibility to convert the undesired chemical

waste to a valuable product. This approach allows for closing the agricultural nitrogen cycle and helps to contribute towards a circular economy when the process is sourced from renewable energies. In a more ambitious approach, the large amounts of NO<sub>x</sub> gases generated by fossil fuel power plants, which can be absorbed in liquid solutions as nitrate and nitrite, could be reduced electrochemically to ammonia.<sup>15</sup>

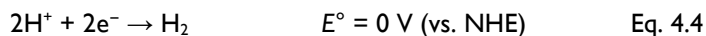


The electrochemical nitrate reduction has been extensively investigated for potential water treatment applications, where nitrogen is the main targeted reaction product (Eq. 4.3).<sup>16</sup>



Fundamental studies on the electrochemical nitrate reduction towards nitrogen at various noble and non-noble metal electrodes have been reported in literature.<sup>17-20</sup> The electrochemical conversion of nitrate to ammonia has gained interest only recently as a potential solution for nitrate valorization and faradaic efficiencies of up to 100% were achieved.<sup>21-23</sup> Still, for the commercialization and large-scale operation of the process, it is important to be able to perform the reaction in flow electrolysis cells at high faradaic efficiency and high selectivity towards ammonia/ammonium, reaching high single-pass conversion at the same time.

The nitrate reduction reaction to nitrogen has been implemented in a PEM flow cell, with high nitrate conversion and selectivity towards nitrogen reported using Cu, Ni, Pt and Pd electrodes.<sup>24-26</sup> This represents an important step towards the large-scale application of an electrochemical denitrification process. However, in the PEM cell the reaction is suggested to proceed via an electrolysis-assisted process in which nitrate ions are not electrochemically reduced at the cathode surface, but rather hydrogenated by the hydrogen evolved at the cathode in HER (Eq. 4.4).<sup>27, 28</sup>



High product yields can be obtained by operating the PEM cell in a high current regime, thus promoting heterogeneous nitrate hydrogenation. Still, the faradaic efficiency of such an approach is low due to high HER activity. On the other hand, it is well known that ammonia/ammonium formation from nitrate is favored at low electrolyte pH, which is the case for membranes typically used in PEM electrolysis cells.<sup>29</sup> Therefore, with an appropriate

choice of the cathode catalyst and by suppressing the competing HER, high faradaic efficiencies of nitrate reduction to ammonia in PEM cells should be achievable. A schematic representation of a PEM cell applied to electrochemical nitrate reduction is presented in Figure 4.1.

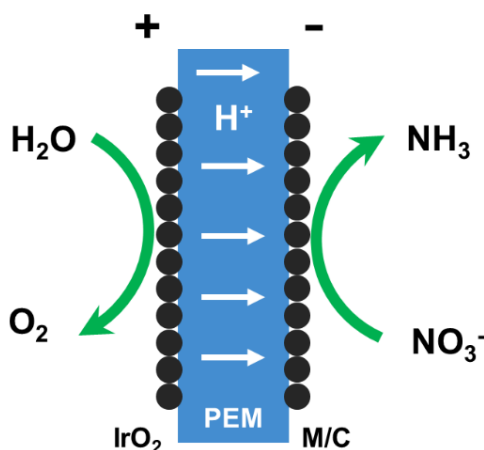


Figure 4.1: Schematic representation of the electrochemical nitrate reduction in a PEM electrolysis cell.

Recently, the electrochemical nitrate reduction to ammonia in an alkaline flow cell has been reported in studies.<sup>22</sup> The main motivation for the choice of an alkaline cell is the disfavored HER in alkaline media compared to acidic media, which should lead to higher faradaic efficiency of nitrate reduction products.<sup>30</sup> Although 100% faradaic efficiency for ammonia was obtained, the use of a liquid alkaline electrolyte, which is often corrosive, represents a significant environmental issue and possibly hinders a large-scale application of alkaline cells. Furthermore, considering the preferable acidic environment for ammonia formation from nitrate, the use of alkaline cells is counterintuitive. In a batch cell, the positive influence of low electrolyte pH and high nitrate concentration on ammonia formation was shown, reaching 82% faradaic efficiency.<sup>14</sup>

Therefore, for an electrochemical nitrate to ammonia process, enabling the reaction at high efficiency in a flow-through PEM electrolysis cell would be an important step towards the large-scale application. In this study, after identifying an active and selective catalyst, we show

how the faradaic efficiency can be improved by controlling the amount of protons travelling through the PEM and thus matching the rate of nitrate reduction rate with that of the HER.

## 4.2 Experimental

### 4.2.1 Catalyst synthesis

Pd/C, Cu/C, Rh/C and Ru/C catalyst powders were synthesized by the sodium borohydride reduction method as described for Cu/C and Pd/C elsewhere.<sup>31</sup> Vulcan XC-72 carbon black from Cabot Corporation was used as catalyst support. The metal precursor, PdCl<sub>2</sub> (Alfa Aesar, 99.9%), Cu(NO<sub>3</sub>)<sub>2</sub> (Sigma Aldrich, 99.5%), RhCl<sub>3</sub> hydrate (Sigma Aldrich, 99.98%) or RuCl<sub>3</sub> hydrate (Precious Metals Online, 99%) was added to a suspension of 100 mg Vulcan XC-72 in 100 mL water. The amount of precursor was calculated so that the final catalyst loading would be 40 wt%. The mixture was stirred for 1 h at room temperature. Subsequently, the reaction flask was transferred to an ultrasonic bath and a 6-fold molar excess of NaBH<sub>4</sub> powder was added. When bubble evolution stopped, the catalysts were washed by filtration, and dried at 90 °C overnight. The iridium oxide powder was synthesized following a modified Adams fusion method described elsewhere.<sup>32</sup>

### 4.2.2 Catalyst characterization

The synthesized catalyst powders were characterized by N<sub>2</sub> physisorption using a Micromeritics Tristar 3020 after an overnight degassing procedure at 150 °C. Powder X-ray diffractograms were recorded using a Bruker D8 ADVANCE X-ray diffractometer with a Co K-alpha radiation source. TEM micrographs were recorded using a Jeol JEM-1400 plus TEM.

### 4.2.3 MEA preparation

Nafion 115 (simply called Nafion hereafter) membranes (Ion Power) were activated by a three-step procedure: 1 h treatment in 3 wt% H<sub>2</sub>O<sub>2</sub> solution at 80 °C, 1 h treatment in 1 M H<sub>2</sub>SO<sub>4</sub> solution at 80 °C and 1 h treatment in boiling type I ultrapure water. The synthesized catalyst powders were suspended in inks containing 2 mL of isopropanol and Nafion ionomer. The amount of ionomer in the ink was 30 wt% of the catalyst loading. The inks were sonicated for 10 minutes in an ultrasonic bath and were deposited onto Nafion 115 membranes by spray coating. A loading of 2.5 mg cm<sup>-2</sup> was used for cathode catalyst



powders. The anode catalyst inks were prepared in a similar fashion. For the anode, iridium oxide powder was used. The amount of ionomer in the ink was 20 wt% of the catalyst loading. For experiments with hydrogen oxidation at the anode, a commercial 40 wt% Pt/C powder (Sigma Aldrich) was used to prepare the ink. The loading of the Pt/C catalyst was  $0.75 \text{ mg cm}^{-2}$ . The ionomer loading in the ink was the same as for the carbon-supported catalyst powders (30 wt%). After spraying, the membranes were hot pressed at  $120 \text{ }^\circ\text{C}$  at a pressure of 1 MPa for 3 minutes. The prepared catalyst-coated membranes were sandwiched between two  $2 \times 2 \text{ cm}^2$  Pt-coated 0.45 mm thick titanium felt GDLs (68% porosity, Bekaert) and assembled in an in-house designed PEM cell with titanium current collectors and machined serpentine flow channels.

#### **4.2.4 Electrochemical nitrate reduction experiments and product analysis**

A peristaltic pump was used to pump a  $\text{KNO}_3$  solution of different concentrations to the cathode compartment of the PEM cell. Type I ultrapure water was passed to the anode compartment. For experiments with hydrogen oxidation at the anode, a humidified 4 vol%  $\text{H}_2/\text{He}$  mixture was passed through the anode compartment at a flow rate of  $5 \text{ mL min}^{-1}$ . The cell temperature was kept at  $80 \text{ }^\circ\text{C}$  during the experiments. The electrochemical experiments were performed using an AUTOLAB PGSTAT302N potentiostat/galvanostat. Potentiostatic and galvanostatic experiments were performed for a duration of 30 min, over which the current and the potential were recorded, respectively (Figure 4.2).

The reactor outlet tube was immersed in 20 mL of 20 mM HCl solution in order to trap gas phase ammonia in the form of ammonium ion and in order to ensure a reliable quantification of reaction products. The quantification of liquid species was performed using a Metrohm 883 Basic ion chromatograph. A Metrosep C6 column was used for the quantification of ammonium, and a Metrosep A Supp 4 column was used for the quantification of nitrate and nitrite anions. The formed gas-phase products were not quantified; online mass spectrometry studies did not indicate the formation of nitrogen oxides. Thus, we assumed dinitrogen to be the majority gas phase product of electrochemical nitrate reduction.

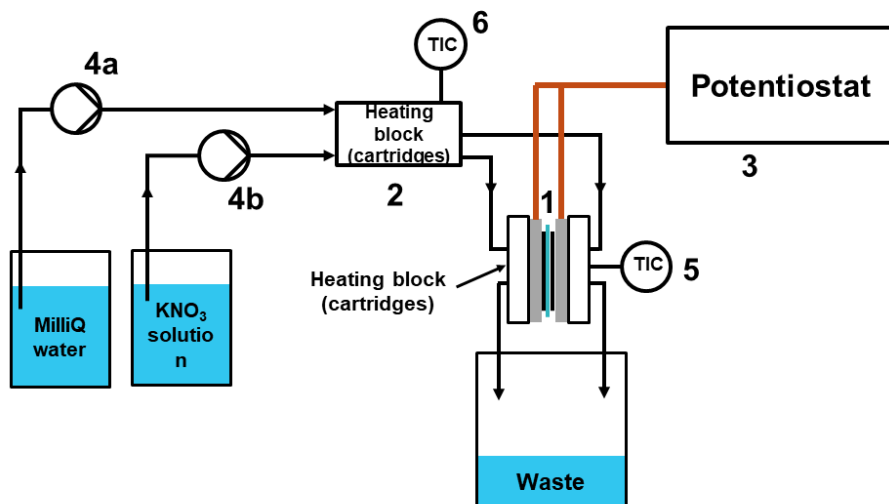


Figure 4.2: Schematic of the nitrate reduction setup: (1) PEM cell, (2) heating blocks, (3) potentiostat, (4a, 4b) peristaltic pumps, (5, 6) temperature controllers.

A flow of  $1 \text{ mL min}^{-1}$  and a 500 ppm nitrate ( $\text{KNO}_3$ ) solution were used during the screening experiments. In experiments with decreased  $\text{IrO}_2$  loading, the flow was set at  $0.5 \text{ mL min}^{-1}$ . Three different nitrate concentration solutions, 200 ppm, 500 ppm and 1000 ppm, were used to study concentration effects. For the recirculation experiment, 30 mL of  $\text{KNO}_3$  solution containing 1000 ppm  $\text{NO}_3^-$  in 80 mM HCl was used. 1 mL liquid samples were collected hourly over the duration of the experiment. The higher concentration of HCl solution used is motivated by the higher amount of ammonia produced over the 8 h experiment, as the 20 mM HCl solution was inefficient to trap the produced ammonia in the liquid phase for reliable quantitative analysis.

Nitrate conversion and ammonium selectivity were calculated based on the nitrogen balance. The faradaic efficiency towards ammonium was calculated using Eq. 4.5.

$$\text{Faradaic efficiency} = \frac{nzF}{It} \quad \text{Eq. 4.5}$$

$n$  = amount of  $\text{NH}_3$  formed

$z$  = number of electrons involved in the reaction

$F$  = Faraday's constant

$I = \text{current}$

$t = \text{time}$

The energy efficiency was calculated using Eq. 4.6.

$$\text{Energy efficiency} = \frac{(E_{\text{NH}_3}^\circ + E_{\text{O}_2}^\circ) \cdot FE_{\text{NH}_3}}{E_{\text{cell}}} \quad \text{Eq. 4.6}$$

$E_{\text{NH}_3}^\circ, E_{\text{O}_2}^\circ = \text{Standard potentials of the cathode and anode reactions}$

$E_{\text{cell}} = \text{Cell potential}$

$FE_{\text{NH}_3} = \text{Faradaic efficiency towards ammonia}$

## 4.3 Results and discussion

### 4.3.1 Catalyst characterization and MEA overpotential analysis

Conductive Vulcan XC-72 carbon black, typically used as a catalyst support both in PEM fuel cells and electrolyzers, was chosen as the support of the active metals due to its good electrical conductivity, high surface area, inertness and facile dispersibility of the resulting catalyst in the inks to be deposited over the Nafion membrane. Powder X-ray diffraction was used to identify the crystalline phase of the metals in the catalysts (Figure 4.3).

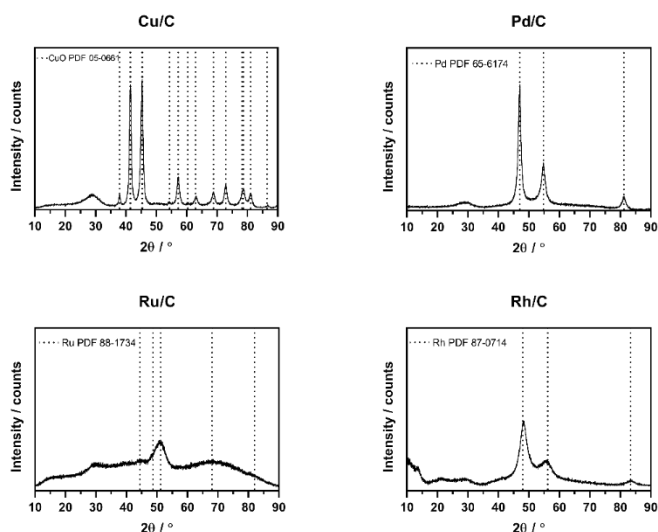


Figure 4.3: X-ray diffraction patterns of Vulcan XC-72-supported metal cathode catalysts.

Due to its amorphous structure, the Vulcan XC-72 support exhibits only a broad peak in the XRD pattern around  $28^\circ 2\theta$ . Based on XRD, Pd, Rh and Ru are present in the metallic form. Reflections characteristic to CuO were identified in the Cu-based catalyst. For the sake of brevity, the catalyst will be further denoted as Cu/C. Particle size and distribution of the active metals vary for each catalyst as indicated by TEM micrographs (Figure 4.4). Rh formed agglomerated clusters of nanoparticles (8-40 nm) over the support. A more uniform distribution of Pd in Pd/C was observed, with Pd particle size between 5 and 30 nm. CuO forms platelets which form agglomerates as large as 100 nm with a poorer dispersion. Ru/C forms spherical nanoparticles ranging from 2 to 6 nm, exhibiting the most uniform distribution among all catalysts, although some agglomerates as large as 20 nm were observed.

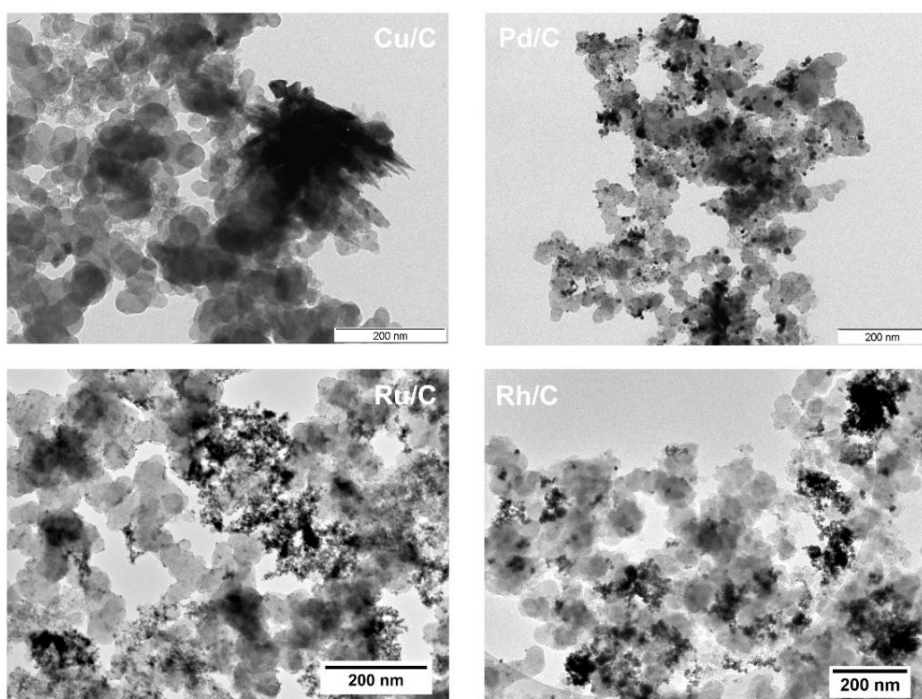


Figure 4.4: TEM micrographs of Vulcan XC72-supported metal cathode catalysts (40 wt% metal loading).

The BET surface area of the catalyst powders ( $122\text{-}168\text{ m}^2\text{ g}^{-1}$ ) measured by nitrogen physisorption is smaller than the surface area of the carbon support ( $238\text{ m}^2\text{ g}^{-1}$ ). This

indicates the deposition of metal nanoparticles over the carbon support, as the nanopores in the carbon support have partially blocked the pores of the nanoparticles, leading to a decrease in surface area (Table 4.1).

Table 4.1: BET surface area and pore volume for the synthesized catalyst powders and the Vulcan XC-72 support.

Material	BET surface area (m <sup>2</sup> g <sup>-1</sup> )	Pore volume (cm <sup>3</sup> g <sup>-1</sup> )
Vulcan XC-72	238	0.050
Pd/C	125	0.014
Ru/C	168	0.032
Cu/C	128	0.018
Rh/C	158	0.027
IrO <sub>2</sub>	122	0.004

The overpotential analysis was conducted according to the procedure reported elsewhere for PEM electrolysis cells.<sup>33</sup> Figure 4.5 provides an example of how the kinetic, Ohmic and mass transport overpotentials were determined. Tafel slopes and Ohmic resistance values determined from impedance spectroscopy are presented in Table 4.2. Recorded impedance spectra are presented in Figure 4.6.

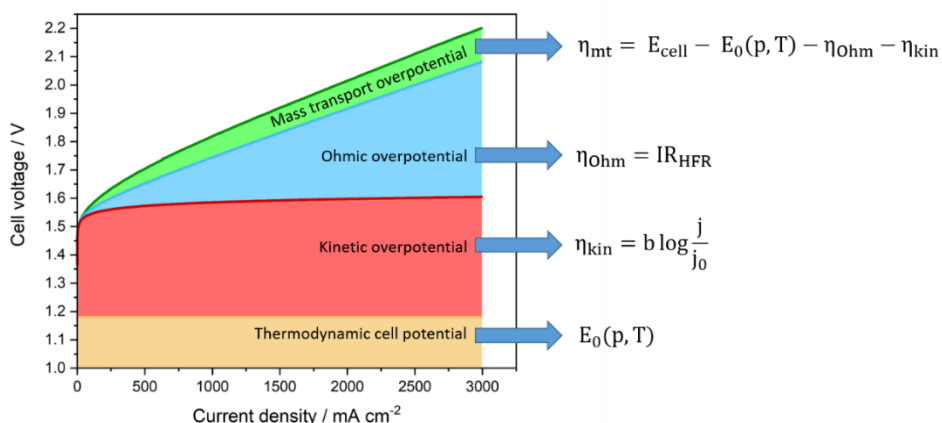


Figure 4.5: Overpotential contributions to overall cell voltage in a typical polarization curve of a PEM electrolyser and the corresponding equations used to model each parameter.

Table 4.2: Kinetic overpotential parameters and Ohmic resistance determined from overpotential analysis of M/C MEAs.

MEA	Tafel slope (V dec <sup>-1</sup> )	log j <sub>0</sub>	R Ohmic (mΩ cm <sup>2</sup> )
Ru/C	0.037	-20.51	192
Pd/C	0.033	-23.24	168
Rh/C	0.035	-14.31	188
Cu/C	0.042	-17.74	192

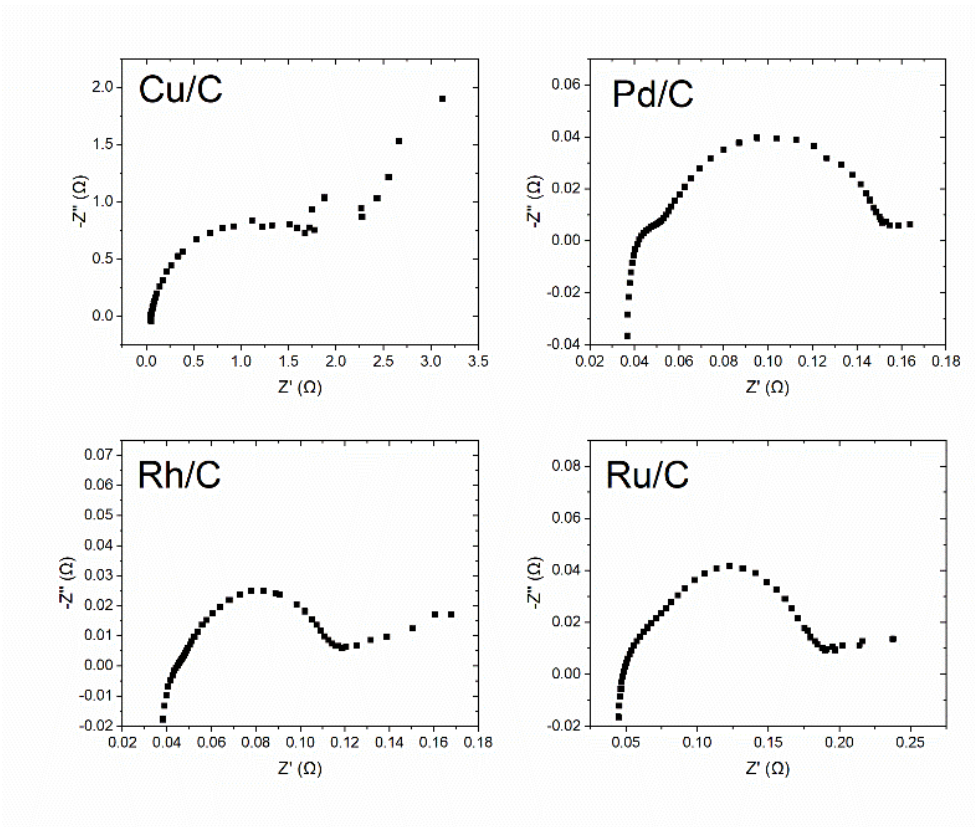


Figure 4.6: Impedance spectra of MEAs with four different metal catalysts.

### 4.3.2 Metal effects on nitrate reduction towards ammonia

Most studies on electrochemical nitrate reduction to ammonia available in literature focus on the investigation of metallic electrodes in three electrode cell assemblies.<sup>20, 34-39</sup> On the

other hand, PEM cells typically require the use of powdered electrocatalysts attached to PEM like Nafion. We synthesized and compared four different carbon-supported metal catalysts, namely Cu/C, Pd/C, Rh/C and Ru/C. The characterization of the catalysts by XRD, TEM and N<sub>2</sub> physisorption are summarized in the supporting information. These active metals were chosen based on the reported activity towards nitrate reduction to ammonia and conversion of nitrates to nitrogen in PEM cells. The catalytic performance of metal-free carbon support confirms very small ammonium formation. Pd is known to be active towards nitrate reduction to nitrogen, and in this context ammonia formation was viewed as the undesired reaction.<sup>25</sup> Rh and Ru were reported to yield ammonia as the major reaction product, with Rh reported to be the most active in three electrode cells using metallic electrodes.<sup>20</sup> Recently, 100% faradaic efficiency towards ammonia was reported over strained ruthenium nanoclusters.<sup>40</sup> A copper nanowire array electrode yielded 95.8% faradaic efficiency.<sup>21</sup> Nevertheless, the performance of these materials was only tested in conventional H-cells, which is difficult to translate to industrial applications.

At the anode, iridium oxide was coated over the Nafion membrane at the loading of 2 mg cm<sup>-2</sup>, which is typical for PEM electrolysis cells targeting water splitting for hydrogen production. XRD study confirmed that the catalyst consists solely of IrO<sub>2</sub> (Figure 4.7). The anode reaction follows Eq. 4.7.



Considering the half reaction of the nitrate reduction to ammonium at the cathode and the half reaction of water oxidation at the anode, a theoretical cell potential of -0.36 V can be expected (Eqs. 4.2 and 4.6). However, experimentally an overpotential is required to drive the reaction, mainly due to the sluggish kinetics of the anode reaction.

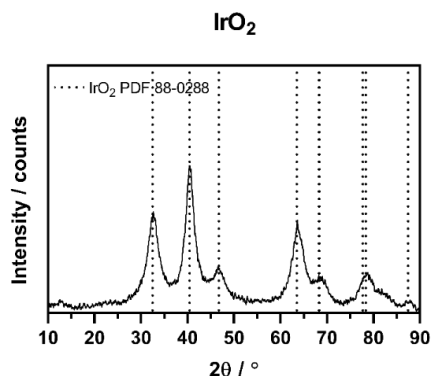


Figure 4.7: X-ray diffraction patterns of IrO<sub>2</sub> used as anode catalyst.

Electrocatalytic performance of the four catalysts was compared in a wide range of cell voltages, namely from 1.6 to 2.8 V. Figure 4.8 presents nitrate conversion using the four carbon-supported metal catalysts. The selectivity values shown here reflect the reaction selectivity towards nitrogen-containing species. Nitrogen was the only gaseous product that contained nitrogen and could be detected by online mass spectrometry. Thus, the product analysis was based mainly on the liquid phase analysis by ion chromatography. On the other hand, the faradaic efficiency reflects electron selectivity, which also includes the formation of hydrogen.

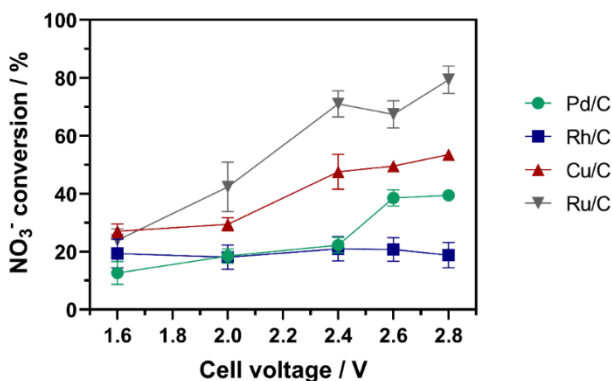


Figure 4.8: Nitrate conversion as a function of cell voltage for four different carbon-supported metal catalysts and metal-free Vulcan XC-72 carbon black.

The nitrate conversion increased in this order: Rh/C < Pd/C < Cu/C < Ru/C. Nitrate conversion increased at a higher cell voltage for all catalysts except Rh/C for which we



recorded a roughly constant conversion (20%), independent of cell voltage. Considering that the nitrate conversion of the carbon support ranged between 10%-20%, the added value of Rh seems marginal. This was unexpected, as Rh is reported to be the most active noble metal for nitrate reduction in acidic electrolyte.<sup>20</sup> All catalysts exhibited an increase in ammonium selectivity at higher cell voltage, reaching approximately 90% for Ru/C (Figure 4.9).

However, the ammonium selectivity increase was accompanied by a decrease in faradaic efficiency at higher cell voltage and higher current density (Figure 4.10, Figure 4.11). At 2.4-2.8 V the faradaic efficiency decreased to <1% for all catalysts, accompanying vigorous bubble formation at the cathode. Online mass spectroscopy of the outlet gas feed indicated H<sub>2</sub> as the only detectable product. This suggests that ammonium is produced via an electrolysis-assisted hydrogenation pathway (i.e., nitrate reacting with produced H<sub>2</sub>) at the high cell voltage, while at 1.6-2.0 V cell voltage the reaction likely follows an electrochemical pathway. The electrolysis-assisted route has been reported for nitrogen formation.<sup>26</sup> In principle, heterogeneous hydrogenation of nitrate to ammonia is also feasible in a PEM cell.<sup>28, 41, 42</sup>

At 1.6 V, Cu/C exhibited the highest faradaic efficiency with 42%, but this value dropped to approximately 11% at 2.0 V. Cu/C exhibited lower selectivity to side-products than Pd/C and Rh/C, but a higher selectivity than Ru/C (Figure 4.9). The general good performance of the Cu/C catalyst for ammonium formation implies that Cu is a promising non-noble metal catalyst for the reaction. Further research, for example using Cu alloys, would be of interest.

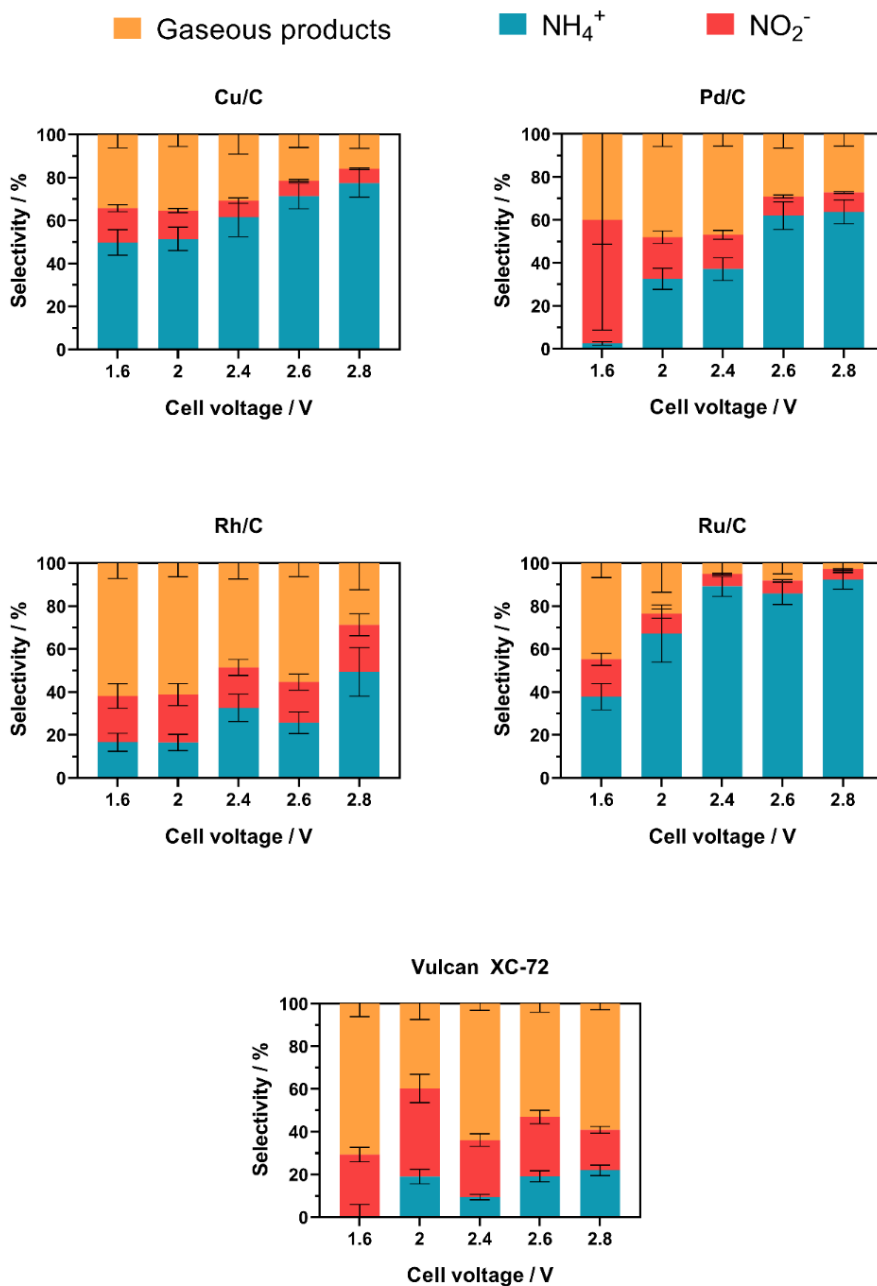


Figure 4.9: Nitrate reduction product selectivity as a function of cell voltage for four different carbon-supported metal catalysts and metal-free Vulcan XC-72 carbon black.

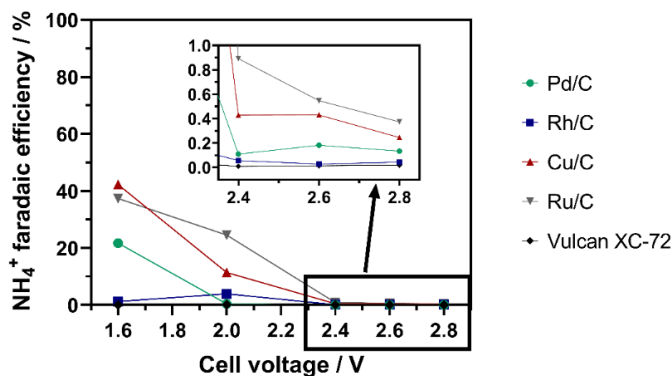


Figure 4.10: Ammonia faradaic efficiency as a function of cell voltage for four different carbon-supported metal catalysts and metal-free Vulcan XC-72 carbon black.

Interestingly, Pd/C showed very low faradaic efficiency for ammonia production over the entire range of the cell voltage (Figure 4.10). Nevertheless, ammonium selectivity reached approximately 65% at 2.8 V cell voltage, which indicates that ammonium can be produced over Pd via an electrolysis-assisted hydrogenation pathway.

Among the four catalysts, Ru/C showed the best faradaic efficiency towards ammonium over the wide range of cell voltages. This, in addition to the highest nitrate conversion and ammonium selectivity, motivated us to investigate the possibility of improving the faradaic efficiency of Ru/C by controlling the amount of protons recombining to hydrogen at the cathode.

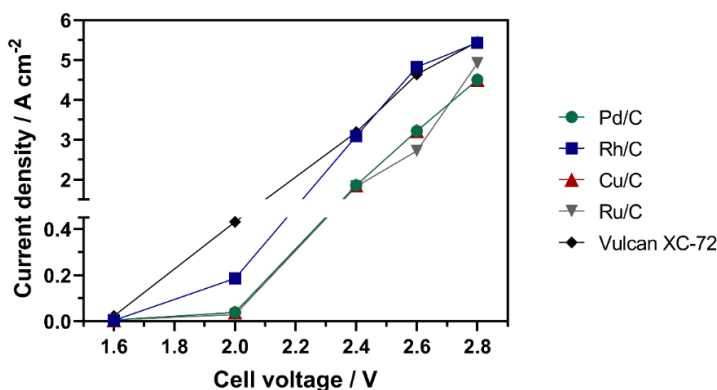


Figure 4.11: Current densities recorded for four different carbon-supported metal catalysts and metal-free Vulcan XC-72 carbon black as a function of cell voltage.

Furthermore, overpotential analysis of the polarization curves was carried out to determine the kinetic overpotentials of the four metals (Figure 4.12, Table 4.2).

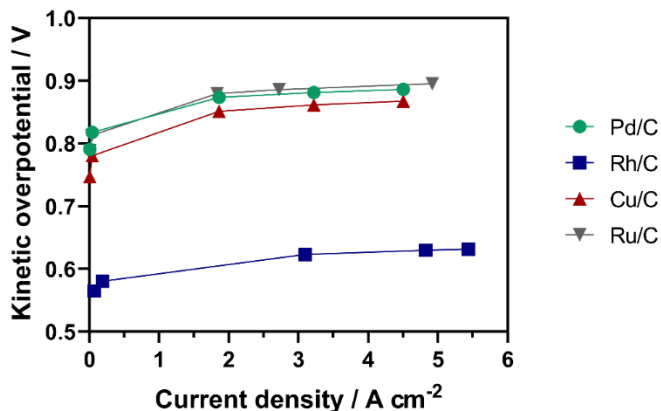


Figure 4.12: Kinetic overpotential of Vulcan XC-72-supported metal catalyst MEAs.

Due to challenges in implementing a reference electrode in the PEM electrolysis cells, it is difficult to disentangle the corresponding contributions from the reactions taking place at the cathode and anode. Hence, the apparent Tafel slopes reflect the reactions taking place at both electrodes. Nevertheless, considering that all the parameters except the cathode catalyst metal were identical, the plots in Figure 4.12 are useful for the purpose of comparing the MEAs that were used. The metal that exhibited the highest kinetic overpotential, Ru, shows the highest activity in nitrate reduction. At the same time, Rh shows the lowest kinetic overpotential for HER, making it a poor catalyst for nitrate reduction. This is in good agreement with literature, which shows that Rh is one of the most active metals to catalyze HER.<sup>43</sup> Based on the kinetic overpotential analysis, lower overpotential values are linked to higher HER rate in comparison to the nitrate reduction. The latter is more kinetically hindered unless HER is disfavored over the surface. Ru seems to achieve this condition by increasing the kinetic overpotential for HER.

### 4.3.3 Improving faradaic efficiency and single pass nitrate conversion to ammonia with Ru/C

When PEM electrolysis cells are used for water splitting, an increase in iridium oxide loading typically leads to higher current densities and higher HER rates in the cell. Increasing the

amount of catalyst at the anode leads to a higher surface area available for water molecules to adsorb and undergo oxidation, and hence there is a higher recorded current at the same cell voltage that is applied. In other words, a lower iridium oxide loading should yield lower current densities by limiting the oxidation reaction and thus restricting the amount of protons generated at the anode and transported to the cathode. Previous experiments indicated HER as the main cause for low faradaic efficiency towards nitrate reduction products and we decided to investigate whether this approach could improve the faradaic efficiency. We therefore decreased the iridium oxide loading from  $2 \text{ mg cm}^{-2}$  to  $0.3 \text{ mg cm}^{-2}$  and shifted the applied cell voltages towards a lower range, from 1.2 to 2.1 V. To increase the nitrate single pass conversion and to increase the effective reaction time in the cell, the nitrate solution flow was decreased from  $1 \text{ mL min}^{-1}$  to  $0.5 \text{ mL min}^{-1}$ .

To investigate the influence of nitrate concentration on the cell performance, we tested three different initial nitrate solution concentrations: 200, 500 and 1000 ppm (Figure 4.13). Interestingly, regardless of nitrate concentration, there is a maximum in the faradaic efficiency around 1.8 V (Figure 4.13a). Increasing the cell voltage further drastically decreased the efficiency. Higher faradaic efficiency was observed in the more concentrated nitrate solutions (53, 69 and 78% for 200, 500 and 1000 ppm solutions, respectively), indicating that high nitrate concentration at the catalyst surface is important to achieve efficient utilization of electrons towards ammonia/ammonium formation. A similar relationship between solution concentration and faradaic efficiency was also reported by McEnaney et al.<sup>14</sup>

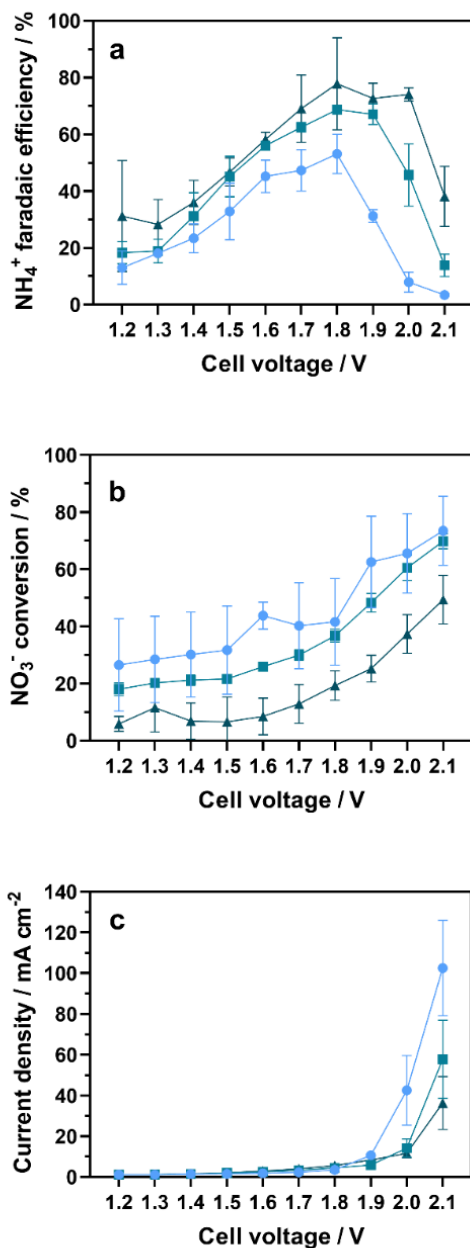


Figure 4.13: Faradaic efficiency towards ammonium, (b) single pass nitrate conversion and (c) current density for solutions of different initial nitrate concentration as a function of cell voltage, Ru/C cathode catalyst and 0.3 mg cm<sup>-2</sup> iridium oxide anode loading.

In terms of the current density, in the 1.2-1.8 V range, the measured values were comparable ( $<10 \text{ mA cm}^{-2}$ ) for the three cases. On the other hand, in the 1.9-2.1 V range, the current density increased for all cases, with the steepest change for the 200 ppm solution, followed by the 500 and 1000 ppm solutions (Figure 4.13b). This tendency is consistent with the concentration effects on the maximum faradaic efficiency at 1.8 V (*vide supra*), indicating that a higher HER rate is observed when the surface nitrate concentration is lower. In other words, by increasing the surface nitrate concentration, the reaction selectivity can be tuned towards ammonium even at high cell voltages.

The single pass conversion in the PEM cell was also affected by the variation of reactant concentration. The highest conversion was observed in the experiments with 200 ppm of initial nitrate solution concentration, reaching 74% at 2.1 V (Figure 4.13c). For the 1000 ppm nitrate solution, the conversion was the lowest, not exceeding 50% at 2.1 V. The amount of converted nitrate increased with concentration from 200 to 500 ppm. Changing the concentration to 1000 ppm did not result in a further increase in the amount of converted nitrate compared to the 500 ppm case in the 1.2-1.8 V range. At higher cell voltages, differences between the converted nitrate amount became more noticeable between the 500 and 1000 ppm solutions, with more nitrate transformed at higher concentration. This may suggest that at high cell voltages, nitrate conversion proceeds via a different or an additional mechanism, as a slight decrease in ammonia selectivity was also observed in this potential range (Figure 4.14). For example, the reaction rate might be enhanced by the activated electrolysis-assisted path.

$\text{NH}_4^+$   $\text{NO}_2^-$  Gaseous products

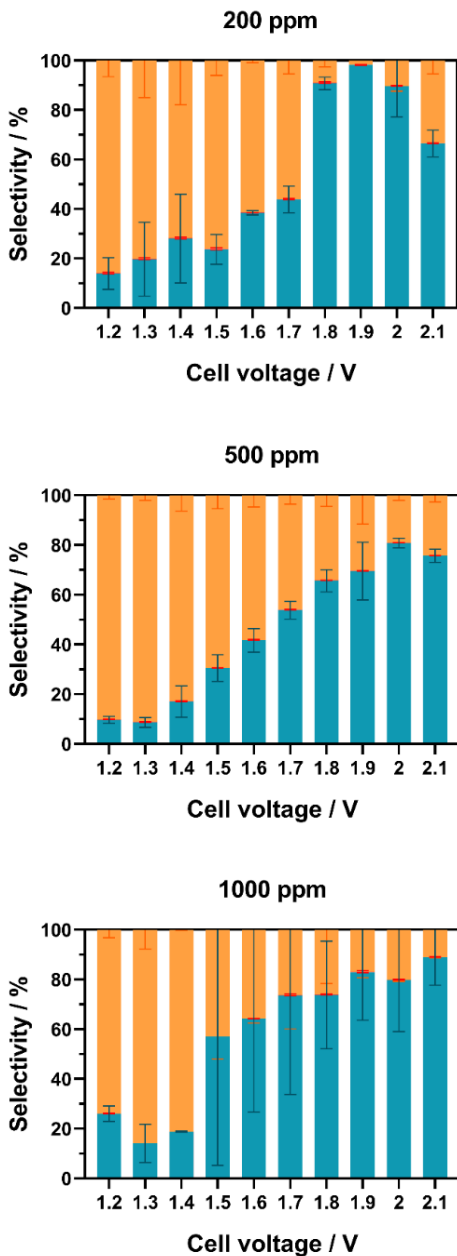


Figure 4.14: Nitrate reduction product selectivity for the Ru/C catalysts and  $0.3 \text{ mg cm}^{-2} \text{ IrO}_2$  loading MEA (water oxidation anode), for solutions of different concentrations as a function of cell voltage.



Mass transport overpotential as a function of concentration was determined by overpotential analysis (Figure 4.15). In general, higher mass transport overpotential was observed at higher nitrate concentrations. At cell voltages of  $>1.9$  V, HER becomes dominant over nitrate reduction according to the faradaic efficiency, and the concentration dependency implies that higher nitrate concentration hinders the HER. This is explained by the higher surface nitrate concentration and consequent kinetic hindrance of HER at the electrode surface.

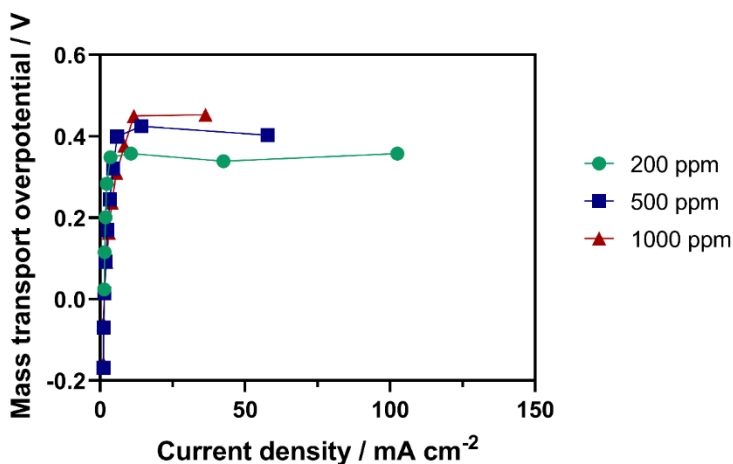


Figure 4.15: Mass transport overpotential for Ru/C MEAs with  $0.3 \text{ mg cm}^{-2}$   $\text{IrO}_2$  anode catalyst at different nitrate solution concentrations.

Overall, our approach of decreasing the anode catalyst loading is effective, drastically improving the ammonium faradaic efficiency of Ru/C by approximately 38% (Figure 4.10 vs. Figure 4.13a) up to 69% at 1.8 V for the 500 ppm nitrate solution. Importantly, the current density during the experiments with  $0.3 \text{ mg cm}^{-2}$   $\text{IrO}_2$  loading was one order of magnitude lower than that recorded for the MEAs with  $2 \text{ mg cm}^{-2}$   $\text{IrO}_2$  loading at the anode. At cell voltages higher than 2.0 V, a sharp drop in the faradaic efficiency was observed, accompanied by an increase in the current density for the undesired use of the electrons for HER. We have shown the possibility to reach high single pass nitrate conversions and ammonium faradaic efficiencies at the low current densities and demonstrated the facile electrochemical activation of nitrate and the favorable reaction kinetics with the Ru catalyst despite the involvement of eight electrons for the conversion. Such “mild” electrochemical conditions

with the high reaction performance suggest promising prospects for the industrial implementation of an electrochemical nitrate to ammonium/ammonia process.

The highest recorded energy efficiency of nitrate reduction to ammonia was 15% for the 1000 ppm solution at 1.8 V (Figure 4.16).

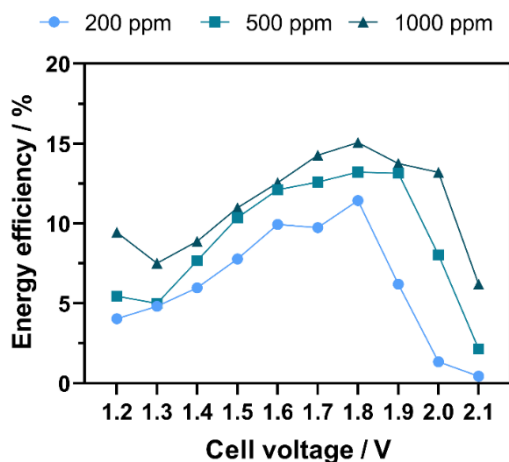


Figure 4.16: Energy efficiency towards ammonia as a function of cell voltage for the Ru/C MEA with  $0.3 \text{ mg cm}^{-2} \text{ IrO}_2$  anode catalyst.

#### 4.3.4 Maximizing ammonium faradaic efficiency by replacing the anode reaction from water oxidation to hydrogen oxidation

So far, we demonstrated a way to tune the current density and proton transport through the membrane electrolyte by decreasing the catalyst loading, and hence the number of active sites for water dissociation and oxidation. From a different point of view, it should be possible to control the proton transport by limiting the amount of water at the anode. For this aim, we conducted electrolysis experiments using water vapor as anode feed. Unfortunately, we were not successful in obtaining reproducible and reliable results. An underlying reason could be the uncontrolled water condensation inside our PEM cell. As an alternative approach, we replaced water oxidation taking place at the anode by hydrogen oxidation for generating protons at the anode. This has a great advantage since the hydrogen concentration in the gas flow can be more precisely controlled. Furthermore, by using a Pt-based catalyst and at low current densities, the anode can be considered a pseudo-reference

reversible hydrogen electrode (RHE), which allows for a better understanding of how the working electrode (cathode) potential influences the nitrate reduction reaction.

As expected, the potentials at which comparable current densities were achieved were considerably lower, as the overpotential of the hydrogen oxidation reaction is considerably lower than the overpotential of the water oxidation reaction. In principle, coupling nitrate reduction to ammonia at the cathode and hydrogen oxidation at the anode yields a theoretical cell potential of 0.88 V. Experimentally, an open circuit potential (OCP) of approximately 0.6 V was observed, but we were not able to identify ammonium formation under OCP conditions. Application of cathodic potentials was required to drive ammonia formation, likely due to the existence of overpotential in the cell.

We investigated the reaction performance for the three different concentrations of nitrate solution (Figure 4.17), similar to the previous experiments (Figure 4.13). We passed a humidified 4% hydrogen feed to the anode compartment at 5 mL min<sup>-1</sup>. Under these conditions, the amount of hydrogen undergoing dissociation and the amount of protons available and traveling through the membrane towards the cathode compartment were strongly limited. This was reflected by the low current densities recorded during the experiments, which did not exceed approximately 7 mA cm<sup>-2</sup>. They did not increase with applied potential between -0.6 and -1.2 V vs. pseudo-RHE (Figure 4.17a). The trend observed earlier regarding the faradaic efficiency was found for solutions of different nitrate concentrations, decreasing in this order: 1000 > 500 > 200 ppm. For the 1000 ppm nitrate solution, a remarkably high faradaic efficiency of 94% for ammonium was observed. This confirms the positive effects of higher nitrate concentration at the catalyst surface on the ammonium faradaic efficiency.

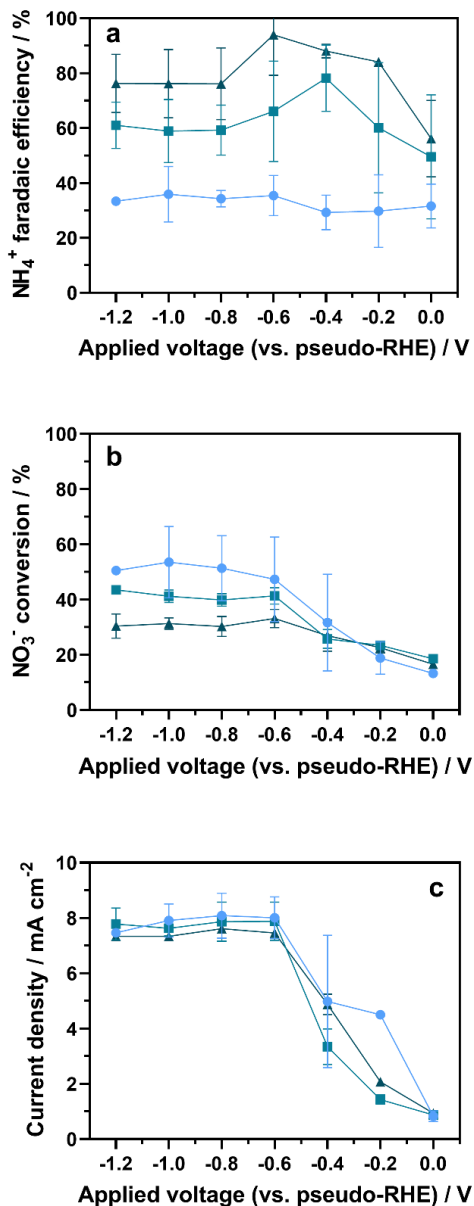


Figure 4.17: (a) Faradaic efficiency towards ammonium, (b) nitrate conversion and (c) current density for Ru/C cathode catalyst, Pt/C anode catalyst and  $5 \text{ mL min}^{-1}$  humidified 4%  $\text{H}_2/\text{He}$  flow.

Generally, the observed faradaic efficiency values were higher compared to the case where water oxidation took place at the anode. Conversely, the current densities at which

maximum faradaic efficiency was observed were lower in experiments with hydrogen oxidation:  $7.5 \text{ mA cm}^{-2}$  at  $-0.6 \text{ V}$  vs. pseudo-RHE (94% FE) vs.  $8.4 \text{ mA cm}^{-2}$  at  $1.9 \text{ V}$  cell voltage (78% FE) for the 1000 ppm nitrate solution;  $3.34 \text{ mA cm}^{-2}$  at  $-0.4 \text{ V}$  vs. pseudo-RHE (78% FE) vs.  $4.49 \text{ mA cm}^{-2}$  at  $1.9 \text{ V}$  (69% FE) for the 500 ppm nitrate solution. The increase in the faradaic efficiencies with decreasing current densities suggests a lower HER rate in the experiments with hydrogen oxidation at the anode and even more efficient use of electrons towards ammonium formation.

For the 200 ppm nitrate solution, the observed maximum faradaic efficiency was lower than in the case of water oxidation at the anode. However, the current density in the experiments with water oxidation was lower for the 200 ppm nitrate solution;  $2\text{-}3 \text{ mA cm}^{-2}$  at maximum faradaic efficiency (48%). When hydrogen oxidation was used as the anode reaction, the current density was approximately  $7 \text{ mA cm}^{-2}$  at maximum faradaic efficiency (35%) at  $-0.6 \text{ V}$  vs. pseudo-RHE. The lower faradaic efficiency could be due to a higher extent of HER, induced by the poorer availability of nitrate at the catalyst surface.

Notably, the difference in the cell voltage values at which the maximum faradaic efficiency was obtained for the two cases (water oxidation vs. hydrogen oxidation) was approximately  $1.3 \text{ V}$ . This is close to the theoretical potential of  $1.23 \text{ V}$  required for water oxidation at the anode. This is an indirect proof that the reaction is electrochemically driven by the cathodic potential when the faradaic efficiency is high. Furthermore, the electrochemical nitrate reduction to ammonia can be operated at a considerably lower cell voltage when an external hydrogen supply is used. This mode of operation allows avoiding the use of the expensive iridium oxide as a water oxidation catalyst.

Interestingly, the faradaic efficiency towards ammonium decreased in the potential range of  $-0.8 - -1.2 \text{ V}$  vs. pseudo-RHE for the 500 ppm and 1000 ppm nitrate solution (Figure 4.17a). This decrease in faradaic efficiency was not accompanied by a substantial change in current density, which was limited by the low hydrogen flow at the anode. This may be due to a change in selectivity of nitrate reduction as a function of applied potential. No nitrite formation was observed during the experiments with hydrogen oxidation at the anode either (Figure 4.18), and thus this decrease in faradaic efficiency can be attributed to the formation of gaseous nitrate reduction products, although they could not be detected in this work.

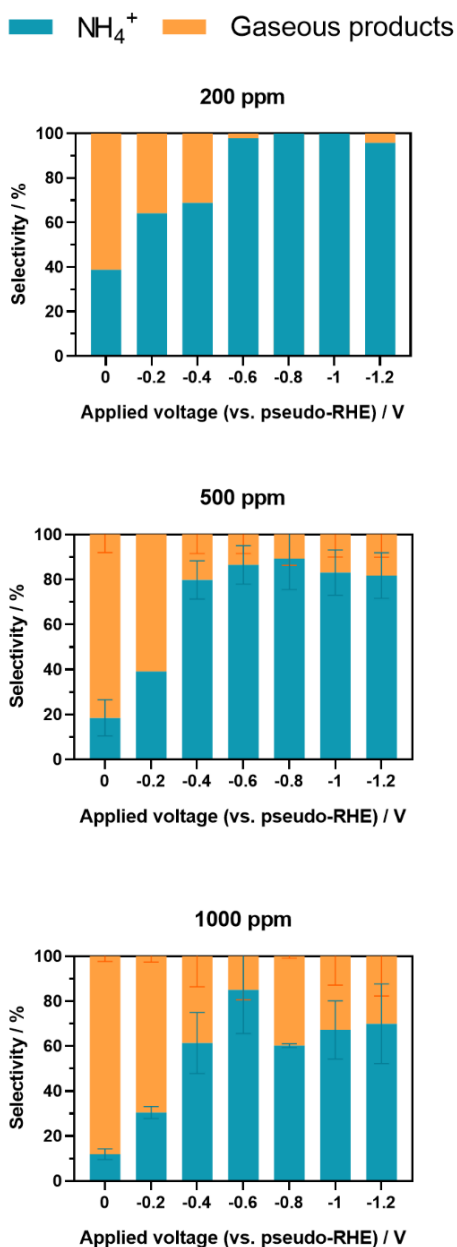


Figure 4.18: Nitrate reduction product selectivity for the Ru/C catalysts and Pt/C (hydrogen oxidation anode) MEA, for solutions of different concentrations.

The nitrate conversion showed an increase down to  $-0.6$  V vs. pseudo-RHE and did not increase further at more negative potentials (Figure 4.17b). Considering the rather constant current densities observed in the potential range of  $-0.6$  –  $-1.2$  V due to limited availability of protons, this observation supports the hypothesis of a hydrogenation pathway for ammonia formation in this potential range. The highest conversion was observed for the 200 ppm nitrate solution, at approximately 50%. The conversion showed a decrease with increasing solution concentration, reaching approximately 30% for the 1000 ppm nitrate solution. This is consistent with previous experiments with water oxidation at the anode, and indicates the impact of nitrate concentrations on its availability on the catalyst surface.

In the experiments with hydrogen oxidation at the anode we were able to reach almost 100% faradaic efficiency for the 1000 ppm nitrate solution, proving that high faradaic efficiencies for electrochemical transformations in a PEM cell are possible. The highest energy efficiency of 70% is at  $-0.2$  V vs. pseudo-RHE (Figure 4.19). Solutions of higher nitrate concentration are expected to yield higher faradaic efficiency towards ammonium. The most critical element to reaching high faradaic efficiencies was proved to be precise control of the current density, and hence, the proton transport through the membrane. This is necessary to suppress HER by limiting the hydrogen availability at the anode.

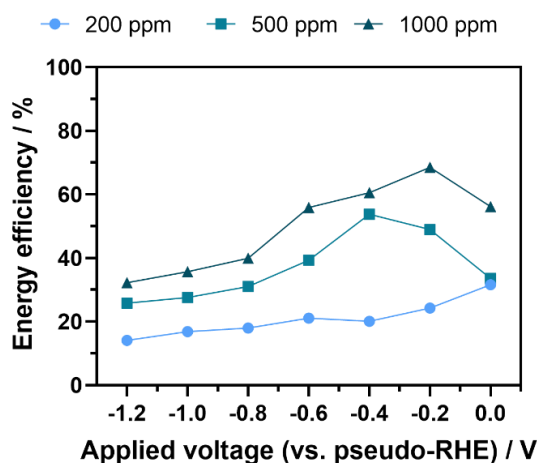


Figure 4.19: Energy efficiency towards ammonia as a function of applied voltage for the Ru/C and Pt/C catalyst (hydrogen oxidation at anode) MEA.

### 4.3.5 Maximizing nitrate conversion by cathode solution recirculation

Depending on the source of nitrate streams, nitrate concentrations vary and flexible strategies are required to achieve the desired nitrate conversions, ideally to ammonium in our case. A practical solution to influence the reaction time is to recirculate the solution through the cell. To test whether achieving full nitrate conversion by this approach is feasible, we conducted a  $10 \text{ mA cm}^{-2}$  constant current electrolysis experiment for 8 h, during which 30 mL of a 1000 ppm nitrate solution was recirculated at a flow rate of  $0.5 \text{ mL min}^{-1}$  through the cathode compartment of the cell. In this experiment, water oxidation was the anode reaction. The nitrate conversion showed a steady increase over the reaction duration and reached 93% after 8 h (Figure 4.20). The selectivity towards ammonium increased from 61% after the first hour of reaction to 75% after 8 h. The recorded faradaic efficiency towards ammonium was 46% after the first hour of reaction and decreased to 26% after 8 h. The decrease in the faradaic efficiency can be attributed to a lower nitrate concentration in the recirculated solution as the reaction proceeded and to more severe competition with HER.

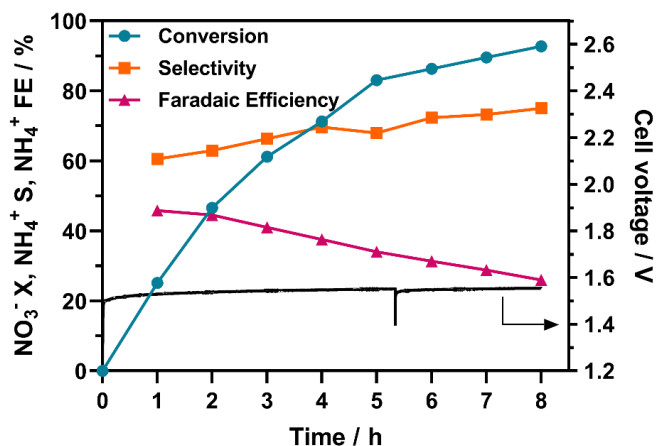


Figure 4.20: Nitrate conversion (X), ammonium faradaic efficiency (FE) and selectivity (S) and the recorded cell voltage for an 8 h recirculation experiment with 1000 ppm nitrate solution,  $10 \text{ mA cm}^{-2}$  constant current electrolysis.

A notable detail of this experiment was that HCl was added to the nitrate solution and recirculated at the cathode for an efficient trapping of ammonia in the form of ammonium ion in the liquid phase. The amount of added HCl was 2.4 mmol to account for an 80 mM



acid concentration in the reaction flask. The addition of the acid led to a decrease in cell voltage from 1.9 to 1.4 V. It is well-established that the nitrate reduction reaction is more favorable in an acidic environment, which is the case for the Nafion membrane that we used in our cell. Nevertheless, a pH gradient between the nitrate solution flowing into the cell and the membrane exists. The nitrate solution that we typically used showed pH values between 6 and 7. With the acid addition, the pH of the solution decreased to approximately 1.1. The observation of the lower cell voltage of this experiment hints at the importance of the nitrate solution pH passed into the electrolyser, aside from the membrane pH.

Furthermore, the cell voltage increased by  $4.25 \text{ mV h}^{-1}$ , which suggests a promising long-term stability of the cell. The performance degradation in PEM cells depends on many factors, including the stability of current collector material, iridium oxide anode catalysts and Nafion membrane besides water impurities. The optimization of long-term stability of PEM cells is therefore part of a broader field, and outside of the scope of the current study.

The recirculation operation mode was proved efficient in reaching >90% nitrate conversion in the PEM cell. Due to the addition of HCl, ammonia is present in the form of ammonium chloride after the 8 h experiment. The recovery of ammonia gas from ammonium chloride can be achieved by stripping at alkaline pH values.

### 4.4 Conclusions

Continuous electrochemical nitrate reduction to ammonia in a PEM electrolyser was investigated. Ru was found as an active and selective cathode metal catalyst for the reaction. We were able to suppress HER by regulating the amount of protons transported through the PEM and could reach almost full faradaic efficiency as high as 94% towards ammonium. Proton transport was controlled by tuning the amount and thus activity of the anode catalyst for water oxidation or by passing a controlled amount of  $\text{H}_2$  at the anode. The results indicate the importance of optimizing the counter-electrode reaction to reach high efficiency in electrocatalytic transformations using PEM cells, an aspect which is often overlooked in literature on the scaling up of electrochemical reactions. Although further investigation is necessary, direct electrocatalytic transformation of nitrate to ammonium was hinted at lower cell voltage up to the point where the faradaic efficiency towards ammonium formation reaches a maximum. Above the cell voltage reaching the maximum, the reaction

is apparently dominated by the electrolysis-assisted hydrogenation, namely nitrate hydrogenation by H<sub>2</sub> produced in the PEM cell. Furthermore, the availability of the nitrate ions near the catalyst surface plays a vital role in defining the faradaic efficiency; the higher the concentration, the higher the efficiency. This poses a practical challenge of converting a low concentration nitrate solution or reaching full nitrate conversion where HER is difficult to be suppressed. In such a case, by regulating proton transport precisely and using hydrogen at the anode, one can still achieve good and selective conversion of nitrate to ammonia/ammonium.

## 4.5 References

1. G. Soloveichik, *Nat. Catal.*, 2019, **2**, 377.
2. J. W. Erisman, M. A. Sutton, J. Galloway, Z. Klimont and W. Winiwarter, *Nat. Geosci.*, 2008, **1**, 636.
3. X. Zhang, E. A. Davidson, D. L. Mauzerall, T. D. Searchinger, P. Dumas and Y. Shen, *Nature*, 2015, **528**, 51.
4. M. Appl, *Ullmann's Encyclopedia of Industrial Chemistry*, ed. 2011,
5. L. K. Boerner, in *Chemical & Engineering News*, American Chemical Society, 2019, vol. 97.
6. A. R. Singh, B. A. Rohr, J. A. Schwalbe, M. Cargnello, K. Chan, T. F. Jaramillo, I. Chorkendorff and J. K. Nørskov, *ACS Catal.*, 2017, **7**, 706.
7. J. G. Chen, R. M. Crooks, L. C. Seefeldt, K. L. Bren, R. M. Bullock, M. Y. Darensbourg, P. L. Holland, B. Hoffman, M. J. Janik, A. K. Jones, M. G. Kanatzidis, P. King, K. M. Lancaster, S. V. Lymar, P. Pfromm, W. F. Schneider and R. R. Schrock, *Science*, 2018, **360**, eaar6611.
8. J. Deng, J. A. Iñiguez and C. Liu, *Joule*, 2018, **2**, 846.
9. V. Kyriakou, I. Garagounis, A. Vourros, E. Vasileiou and M. Stoukides, *Joule*, 2020, **4**, 142.
10. S. Z. Andersen, V. Čolić, S. Yang, J. A. Schwalbe, A. C. Nielander, J. M. McEnaney, K. Enemark-Rasmussen, J. G. Baker, A. R. Singh, B. A. Rohr, M. J. Statt, S. J. Blair, S.

- Mezzavilla, J. Kibsgaard, P. C. K. Vesborg, M. Cargnello, S. F. Bent, T. F. Jaramillo, I. E. L. Stephens, J. K. Nørskov and I. Chorkendorff, *Nature*, 2019, **570**, 504.
11. Y.-C. Hao, Y. Guo, L.-W. Chen, M. Shu, X.-Y. Wang, T.-A. Bu, W.-Y. Gao, N. Zhang, X. Su, X. Feng, J.-W. Zhou, B. Wang, C.-W. Hu, A.-X. Yin, R. Si, Y.-W. Zhang and C.-H. Yan, *Nat. Catal.*, 2019, **2**, 448.
  12. X. Guo, H. Du, F. Qu and J. Li, *J. Mater. Chem. A*, 2019, **7**, 3531.
  13. C. Tang and S.-Z. Qiao, *Chem. Soc. Rev.*, 2019, **48**, 3166.
  14. J. M. McEnaney, S. J. Blair, A. C. Nielander, J. A. Schwalbe, D. M. Koshy, M. Cargnello and T. F. Jaramillo, *ACS Sustainable Chem. Eng.*, 2020, **8**, 2672.
  15. Y. Sun, X. Hong, T. Zhu, X. Guo and D. Xie, *Appl. Sci.*, 2017, **7**, 377.
  16. M. Duca and M. T. M. Koper, *Energy Environ. Sci.*, 2012, **5**, 9726.
  17. V. Rosca, M. Duca, M. T. de Groot and M. T. M. Koper, *Chem. Rev.*, 2009, **109**, 2209.
  18. M. Dortsiou and G. Kyriacou, *J. Electroanal. Chem.*, 2009, **630**, 69.
  19. I. Katsounaros, M. Dortsiou, C. Polatides, S. Preston, T. Kypraios and G. Kyriacou, *Electrochim. Acta*, 2012, **71**, 270.
  20. G. E. Dima, A. C. A. de Vooy and M. T. M. Koper, *J. Electroanal. Chem.*, 2003, **554-555**, 15.
  21. Y. Wang, W. Zhou, R. Jia, Y. Yu and B. Zhang, *Angew. Chem., Int. Ed.*, 2020, **59**, 5350.
  22. Y. Wang, A. Xu, Z. Wang, L. Huang, J. Li, F. Li, J. Wicks, M. Luo, D.-H. Nam, C.-S. Tan, Y. Ding, J. Wu, Y. Lum, C.-T. Dinh, D. Sinton, G. Zheng and E. H. Sargent, *J. Am. Chem. Soc.*, 2020, **142**, 5702.
  23. P. H. van Langevelde, I. Katsounaros and M. T. M. Koper, *Joule*, 2021, **5**, 290.
  24. M. Machida, K. Sato, I. Ishibashi, M. A. Hasnat and K. Ikeue, *Chem. Commun.*, 2006, 732.

25. M. A. Hasnat, I. Ishibashi, K. Sato, R. Agui, T. Yamaguchi, K. Ikeue and M. Machida, *Bull. Chem. Soc. Jpn.*, 2008, **81**, 1675.
26. J. Ampurdanés, S. Bunea and A. Urakawa, *ChemSusChem*, 2021, **14**, 1534.
27. M. A. Hasnat, R. Agui, S. Hinokuma, T. Yamaguchi and M. Machida, *Catal. Commun.*, 2009, **10**, 1132.
28. I. Katsounaros and G. Kyriacou, *Electrochim. Acta*, 2008, **53**, 5477.
29. J. Yang, P. Sebastian, M. Duca, T. Hoogenboom and M. T. M. Koper, *Chem. Commun.*, 2014, **50**, 2148.
30. T. Cheng, L. Wang, B. V. Merinov and W. A. Goddard, *J. Am. Chem. Soc.*, 2018, **140**, 7787.
31. O. M. Ilinitch, F. P. Cuperus, L. V. Nosova and E. N. Gribov, *Catal. Today*, 2000, **56**, 137.
32. S. Siracusano, V. Baglio, S. A. Grigoriev, L. Merlo, V. N. Fateev and A. S. Aricò, *J. Power Sources*, 2017, **366**, 105.
33. T. Schuler, T. J. Schmidt and F. N. Büchi, *Journal of The Electrochemical Society*, 2019, **166**, F555.
34. K. Bouzek, M. Paidar, A. Sadílková and H. Bergmann, *J. Appl. Electrochem.*, 2001, **31**, 1185.
35. G. E. Dima, G. L. Beltramo and M. T. M. Koper, *Electrochim. Acta*, 2005, **50**, 4318.
36. S. Taguchi and J. M. Feliu, *Electrochim. Acta*, 2007, **52**, 6023.
37. M. Li, C. Feng, Z. Zhang and N. Sugiura, *Electrochim. Acta*, 2009, **54**, 4600.
38. M. Li, C. Feng, Z. Zhang, Z. Shen and N. Sugiura, *Electrochem. Commun.*, 2009, **11**, 1853.
39. E. Pérez-Gallent, M. C. Figueiredo, I. Katsounaros and M. T. M. Koper, *Electrochim. Acta*, 2017, **227**, 77.

40. J. Li, G. Zhan, J. Yang, F. Quan, C. Mao, Y. Liu, B. Wang, F. Lei, L. Li, A. W. M. Chan, L. Xu, Y. Shi, Y. Du, W. Hao, P. K. Wong, J. Wang, S.-X. Dou, L. Zhang and J. C. Yu, *J. Am. Chem. Soc.*, 2020, **142**, 7036.
41. X. Huo, D. J. Van Hoomissen, J. Liu, S. Vyas and T. J. Strathmann, *Appl. Catal. B*, 2017, **211**, 188.
42. L. Wei, D.-J. Liu, B. A. Rosales, J. W. Evans and J. Vela, *ACS Catal.*, 2020, **10**, 3618.
43. S. Trasatti, *Journal of Electroanalytical Chemistry and Interfacial Electrochemistry*, 1972, **39**, 163.





# 5

## Electrochemical conversion of NO to NH<sub>3</sub> in a PEM cell

### Abstract

the continuous electrochemical NO reduction to ammonia in a polymer electrolyte membrane cell was investigated in this chapter. We used a ruthenium-based catalyst at the cathode and an iridium oxide catalyst at the anode. The highest ammonia faradaic efficiency was observed at 1.9 V cell voltage. Adjusting the NO flow allowed us to achieve 97% NO conversion and 93% ammonia faradaic efficiency for a 5% NO/He feed. The ammonia yield was 0.51 mmol cm<sup>-2</sup> h<sup>-1</sup>, among the highest reported to date with the unique advantage of continuous operation. Experiments with a low NO concentration feed of 983 ppm showed 98% conversion at 0 V vs. pseudo-RHE. Achieving this remarkable performance at such mild conditions indicates the great potential of the PEM cells for NO<sub>x</sub> abatement applications and the production of valuable NH<sub>3</sub>.

This chapter is based on the following publication:

S. Bunea, M. Coppens, A. Urakawa, *in preparation*.



## 5.1 Introduction

The anthropogenic perturbation of the natural nitrogen cycle represents a concerning threat to the environment.  $\text{NO}_x$  gases emitted by fossil fuel power plants and automobile engines contribute to the formation of acid rains and smog and are harmful for the natural environment and human health.<sup>1</sup> The development of the selective catalytic reduction (SCR) technology and the implementation of such units in power plants have significantly decreased  $\text{NO}_x$  emissions over the last decades.<sup>2</sup> However, the operational costs of SCR are high due to the requirement of continuous ammonia or urea supply, and the resulting dinitrogen gas does not represent a valuable product from a commercial point of view. It would be more desirable to convert  $\text{NO}_x$  gases to a useful chemical such as ammonia. The market price for ammonia is around 500 \$  $\text{ton}^{-1}$ . Currently, ammonia is produced via the energy-intensive Haber-Bosch process, which is responsible for 1% of the yearly global  $\text{CO}_2$  emissions.<sup>3</sup> The electrochemical  $\text{NO}_x$  reduction to ammonia could represent a possible solution for decentralized, on-demand, and small-scale ammonia production powered by renewable electricity.

As the global population is expected to increase over the following decades, so will the production of nitrogen-based fertilizers to meet the growing demand for food.<sup>4</sup> At the same time, the effects of anthropogenic activity over the last 200 years have become increasingly noticeable, impacting the environment in a catastrophic manner. The Paris agreement, adopted in 2016, aims to curb  $\text{CO}_2$  emissions to keep the Earth's temperature increase under 1.5 °C compared to pre-industrial levels. In this context, it is clear that alternative processes for ammonia production need to be developed to aid the achievement of this ambitious goal.

The electrochemical nitrogen reduction reaction (NRR) to ammonia has gained significant research interest over the last decade.<sup>5-8</sup> Nevertheless, reported faradaic efficiency and nitrogen conversion are far from commercially relevant values. The main reason for low efficiency is the high chemical stability of the nitrogen molecule. Efforts to activate nitrogen electrochemically have proved inefficient to date.

An alternative path is to convert the harmful reactive nitrogen species, such as  $\text{NO}_x$ , to ammonia by using renewable electricity, closing the reactive nitrogen cycle (Figure 5.1).

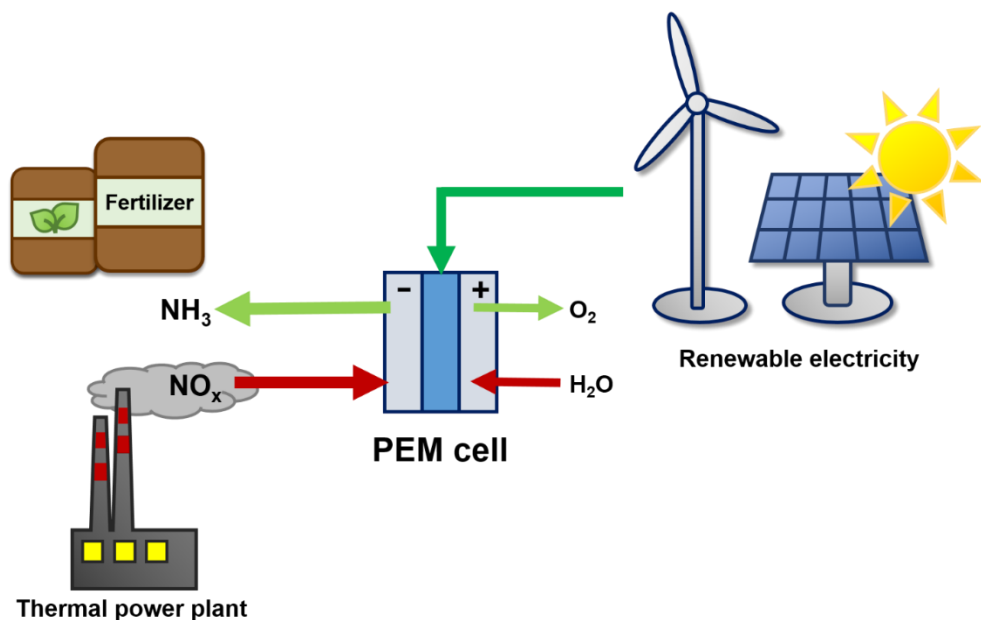


Figure 5.1: Concept of continuous electrochemical ammonia synthesis process from  $\text{NO}_x$  and renewable electricity in a PEM cell.

The technological process of nitrogen fixation via nitric oxide is more than a century old, based on the reaction of nitrogen oxidation first documented by Cavendish.<sup>9</sup> It has actually been implemented on as large a scale as the Birkeland-Eyde process at the beginning of the 20<sup>th</sup> century. The process used electric arc discharge for reacting nitrogen with oxygen to produce nitric oxide, which was subsequently converted to nitrates for use in agriculture. Unfortunately, due to very large energy requirements and the advent of the economic Haber-Bosch process using fossil fuels, the Birkeland-Eyde process was quickly replaced by the new process.<sup>10</sup> Nevertheless, in the context of the depletion of fossil fuels and the impact of huge carbon emissions associated with the Haber-Bosch process, the interest in alternative nitrogen activation routes involving NO has increased in recent years.<sup>11-15</sup> Nitrogen oxidation to NO would represent the first step in a two-step process of sustainable ammonia synthesis. The second step would represent the NO reduction reaction to ammonia, which is the main topic of this work.

The electrochemical NO reduction reaction (NORR) targeting hydroxylamine production was investigated in the 1970s.<sup>16-18</sup> In those studies, ammonia was regarded as a by-product and considered undesirable. In recent years, more studies emphasizing ammonia formation

have emerged.<sup>19-23</sup> Faradaic efficiencies to ammonia as high as 100% were achieved. Nevertheless, most studies report the use of metallic electrodes immersed in liquid electrolyte in batch systems. For large-scale industrial application, a gas flow reactor would be more desirable due to the advantages of continuous operation, thus avoiding the need for an ammonia stripping unit to separate it from the liquid cathode feed.

In this work, a PEM electrolysis cell using a Ru/C cathode catalyst was employed for the gas phase NORR. The cathodic NORR was combined with water oxidation or hydrogen oxidation at the anode of the cell to prove the versatility of the operation. When the hydrogen oxidation reaction (HOR) takes place at the anode, an OCP of approximately 0.85 V was recorded and at low current densities the cell can be concomitantly used for electricity generation. A schematic representation of the two approaches is presented in Figure 5.2.

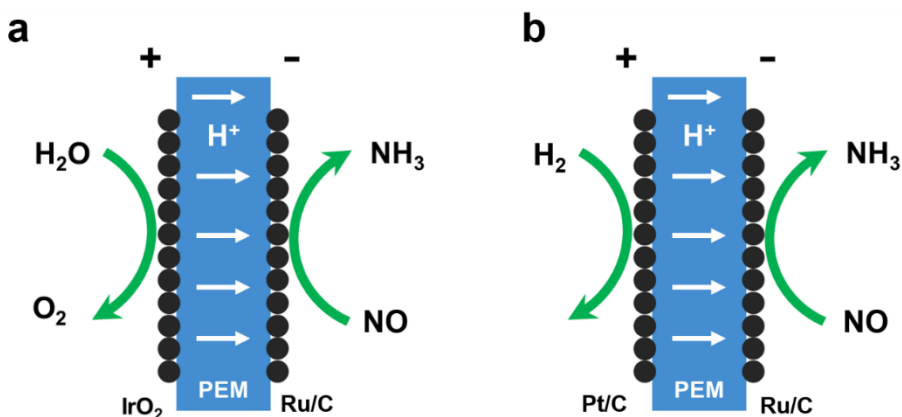


Figure 5.2: Schematic representation of NO reduction at the cathode of a PEM cell with (a) water oxidation and (b) hydrogen oxidation at the anode.

## 5.2 Experimental

### 5.2.1 Catalyst synthesis

Electrically conductive active carbon Vulcan XC-72 (Cabot Corp) was used as catalyst support. RuCl<sub>3</sub> · xH<sub>2</sub>O (Sigma Aldrich) was used as Ru precursor, respectively. The sodium borohydride synthesis method, described elsewhere, was used for the preparation of cathode catalysts.<sup>24</sup> In brief, the powders were prepared by suspending the carbon support

in 100 mL water, to which the soluble metal precursors were added. The precursor concentration was calculated so that the final metal loading in the catalyst would be 40 wt%. After stirring the mixture for 1 h at room temperature, sodium borohydride powder in six-fold excess was slowly added. Vigorous hydrogen gas evolution was observed. The mixture was stirred for another 30 minutes until gas evolution stopped. The resulting catalysts were filtered and washed with 2 liters of water. Subsequently, the powders were dried at 90 °C overnight and were further used for ink preparation and deposition over Nafion membranes.

### 5.2.2 Preparation of MEAs

Commercial Nafion 115 (called Nafion hereafter) membranes with a thickness of 127 μm were used as solid polymer acidic electrolyte in the PEM cell. The membranes were activated as follows: 1 h at 80 °C in 3% H<sub>2</sub>O<sub>2</sub> solution, 1 h at 80 °C in 1 M H<sub>2</sub>SO<sub>4</sub>, followed by 1 h boiling in type I ultrapure water. The cathode catalyst powders were incorporated in isopropanol-based inks, consisting of the catalyst powder (amounting to 2.5 mg cm<sup>-2</sup> loading on membrane), 30 wt% Nafion ionomer and 2 mL of isopropanol. The inks were deposited over heated Nafion membranes at 60 °C via spray-coating deposition. For experiments with water oxidation at the anode, commercial iridium oxide (Premion, Alfa Aesar) was used as anode catalyst and deposited in a similar fashion. The inks in this case consisted of the IrO<sub>2</sub> powder (amounting to 1 mg cm<sup>-2</sup> loading on membrane, unless stated otherwise), 20 wt% Nafion ionomer and 2 mL of isopropanol. For experiments with hydrogen oxidation at the anode, a commercial 40 wt% Pt/C catalyst was used (Sigma Aldrich). The ink composition was similar to that of the NO reduction cathode catalyst, and the amount of catalyst loading on the MEA was 1.5 mg cm<sup>-2</sup>. The Nafion ionomer loading was 30 wt% and 2 mL of isopropanol were used for ink preparation. These were deposited in a similar fashion as the cathode catalysts on the other side of Nafion membranes. After spraying, the catalyst-coated membranes (CCMs) were hot-pressed at 120 °C at 1 MPa pressure for 3 minutes using a lab press.

Subsequently, the CCMs were sandwiched between two porous platinum-coated titanium felt GDLs (0.45 mm, Bekaert) and assembled in an in-house built PEM electrolysis cell with titanium bipolar plates with serpentine flow channels and two aluminum cartridge-heated

end plates. The cell was tightened using 8 stainless steel rods (4 mm  $\varnothing$ ) using a torque wrench set at 5 N·m to ensure uniform compression across the cell area.

### 5.2.3 Nitric oxide reduction setup and product quantification

The setup used for electrochemical NO experiments is presented in Figure 5.3. A mixture of 5% NO and 1% CH<sub>4</sub> in He was fed to the cathode side of the PEM cell via mass flow controllers (MFC) (7.1, 7.2, and 8). A flow of 20 mL min<sup>-1</sup> was used during experiments, unless stated otherwise. He was used for purging the cathode compartment between experiments. The ammonia and hydroxylamine produced at the cathode were trapped in a 0.2 M hydrochloric acid (Sigma Aldrich) solution, which was further analyzed via ion chromatography and UV-vis spectrophotometry (6). In experiments with HOR at the anode, a condenser was used for removing ammonia from the outlet stream. The use of the acid trap led to the humidification of the stream and intense water-characteristic bands in the IR spectra, hindering the quantification of other IR-active species. A Metrohm 883 Basic IC Plus chromatograph equipped with a Metrosep C6 separation column was used for the quantification of ammonia and a Unicam UV 500 UV-Vis spectrometer was used for the quantification of hydroxylamine by a method described elsewhere (6.1).<sup>23,25</sup> A Bruker Alpha infrared spectrometer equipped with a transmission gas analysis module was used for the quantification of NO and N<sub>2</sub>O. CH<sub>4</sub> was used as internal standard to account for volume changes during electrochemical experiments, which can arise due to the consumption of NO as well as due to the trapping of NH<sub>3</sub> or HER. Nitrogen was quantified using a CompactGC (Global Analyser Solutions) (9). At the anode, a peristaltic pump (Ismatec) was used to feed type I ultrapure water at a flow of 1 mL min<sup>-1</sup> in experiments with water oxidation at the anode. An MFC was used to feed hydrogen at a flow of 40 mL min<sup>-1</sup> for experiments with hydrogen oxidation at the anode (3). For the latter, the hydrogen feed was humidified using a syringe pump (Isco), which fed water at a rate of 50  $\mu$ L min<sup>-1</sup> in a preheated tee fitting at 80 °C (10). A Metrohm Autolab PGSTAT302N potentiostat was used for electrochemical measurements (2). The PEM cell was heated at 80 °C using cartridge heaters and a temperature controller (4).

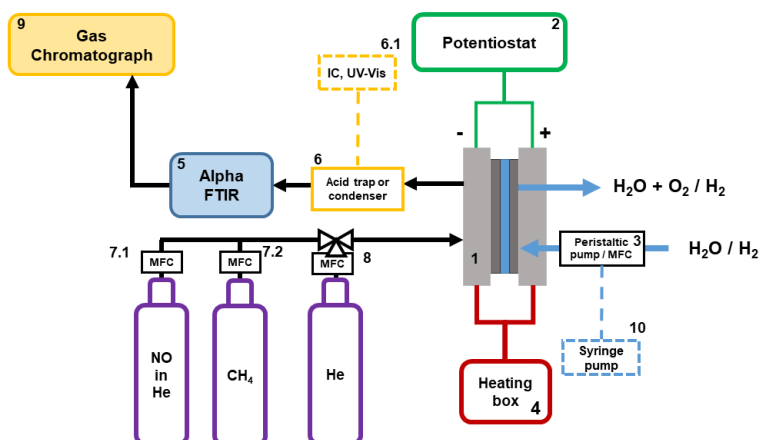


Figure 5.3: Schematic of electrochemical NO reduction setup.

#### 5.2.4 Catalyst characterization

The catalyst powders were characterized by nitrogen physisorption with a Micromeritics Tristar 3020 apparatus after an overnight degassing step at 120 °C. X-ray powder diffractograms were measured with a Bruker D8 ADVANCE X-ray diffractometer with a Co K-alpha radiation source. Transmission electron micrographs were acquired on a Jeol JEM-1400 plus transmission electron microscope (TEM).

Conductive Vulcan XC-72 carbon black, typically used as a catalyst support both in PEM fuel cells and electrolyzers, was chosen as the support of the active metal due to its good electrical conductivity, high surface area, inertness and facile dispersibility of the resulting catalyst in the inks to be deposited over the Nafion membrane. Powder X-ray diffraction was used to identify the crystalline phase of the metal in the catalysts (Figure 5.4). The Vulcan XC-72 support, due to its amorphous structure, exhibits only a broad peak in the XRD pattern around  $28^\circ 2\theta$ . Based on XRD, Ru is present in the metallic form.

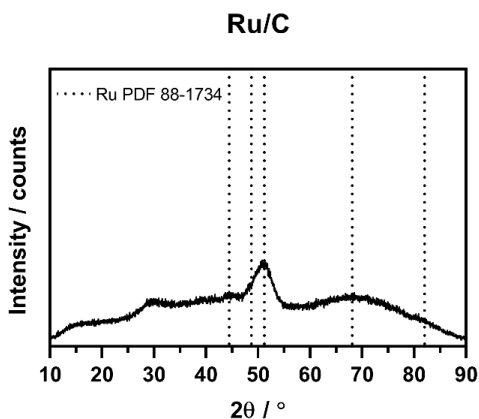


Figure 5.4: X-ray diffractogram of the Ru/C catalyst.

Particle size and distribution of the active metal is indicated by TEM micrographs (Figure 5.5). Ru/C forms spherical nanoparticles range from 2 to 6 nm, exhibiting a uniform distribution, although some agglomerates as large as 20 nm were observed.

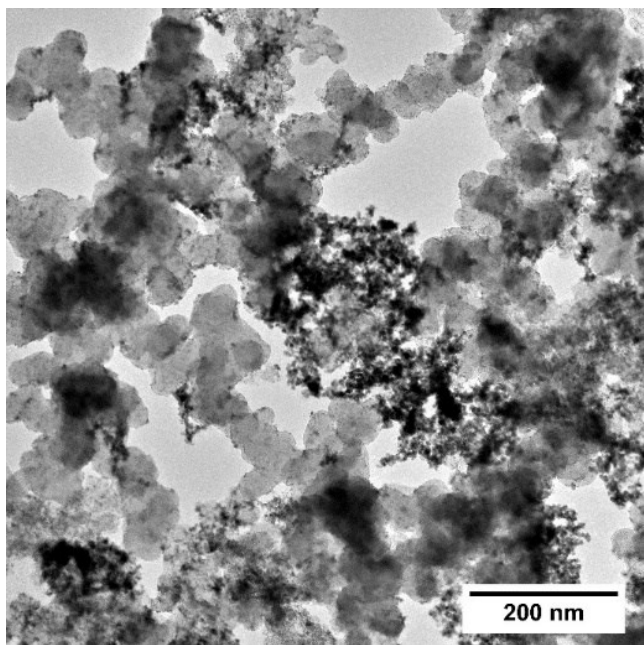


Figure 5.5: TEM micrograph of Vulcan-XC72-supported ruthenium catalyst (40 wt% metal loading). The BET surface area of the Ru/C catalyst was  $168 \text{ m}^2 \text{ g}^{-1}$ , smaller than that of Vulcan XC-72 active carbon ( $238 \text{ m}^2 \text{ g}^{-1}$ ). This indicates the deposition of metal nanoparticles over the

carbon support, as the nanopores in the carbon support have partially blocked the pores of the nanoparticles, leading to a decrease in surface area.

## 5.3 Results and discussion

### 5.3.1 Experiments with water oxidation at anode

The choice of Ru/C catalyst was based on our previous experience with this catalyst in electrochemical nitrate reduction studies in a PEM cell.<sup>26</sup> There, it exhibited high faradaic efficiency and selectivity towards ammonium. As NO is an intermediate species in the electrochemical nitrate reduction mechanism, we expected to observe a similar trend in the activity of the ruthenium catalyst.

We investigated a cell voltage range between 1.7 and 2.1 V. Constant voltage experiments were carried out for 30 minutes. Considering the standard reduction potentials in Eq. 5.1 and Eq. 5.2, the thermodynamic potential of a cell with nitric oxide reduction taking place at the cathode and water oxidation at the anode is  $E^\circ_{cell} = -0.394$  V (Eq. 5.3). Nevertheless, due to competing HER and difficulties in implementing a reference electrode in a PEM cell, the cell voltage range investigated during experiments was significantly higher.



$$E^\circ_{cell} = 0.836 \text{ V} - 1.229 \text{ V} = -0.393 \text{ V} \quad \text{Eq. 5.3}$$

Figure 5.6 presents the faradaic efficiency towards different NO reduction products as a function of cell voltage along with the average current density recorded during the experiments.

The ammonia faradaic efficiency exhibited a promising value of approximately 50% already at the lowest cell voltage tested (1.7 V) with a current density of 32 mA cm<sup>-2</sup>. The faradaic efficiency increased with cell voltage, exhibiting a maximum of approximately 78%, at 1.9 V, at a current density of ca. 64 mA cm<sup>-2</sup>. At 2-2.1 V, the faradaic efficiency to ammonia decreased, and an increase in hydrogen faradaic efficiency was observed.



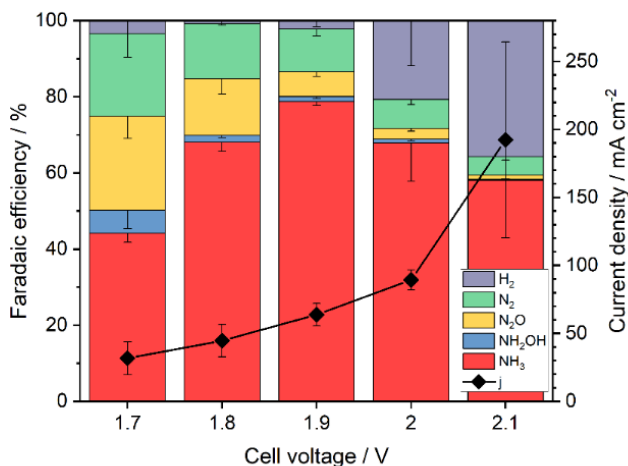


Figure 5.6: Faradaic efficiency towards various products in the NO reduction and current densities at varying cell voltage, 25 mL min<sup>-1</sup> 5% NO/He cathode feed, 2.5 mg cm<sup>-2</sup> 40 wt% Ru/C cathode catalyst, 1 mg cm<sup>-2</sup> IrO<sub>2</sub> anode catalyst, Nafion 115, 80 °C.

The cause for the increase in hydrogen faradaic efficiency is the recorded high current densities at 2 and 2.1 V, leading to an imbalance in the reaction rates at the anode (water oxidation) and the cathode (NO reduction). Under these conditions, a higher amount of protons was generated at the anode, resulting in a higher recombination rate to produce molecular hydrogen at the cathode of the cell, similar to our observations in electrochemical nitrate reduction experiments.<sup>26</sup>

Nitrogen formation was observed at cell voltages as low as 1.7 V. Despite the lowered faradaic efficiency to N<sub>2</sub> at higher cell voltage, N<sub>2</sub> selectivity among the N-containing products remained relatively constant over the whole investigated cell voltage range (Figure 55.7). As reported in our previous studies, it is possible that nitrogen formation does not follow an electrochemical transformation pathway, but rather follows an electrolysis-assisted hydrogenation route.<sup>27</sup> In this latter pathway, the hydrogen is evolved *in situ* at the cathode and reacts with nitric oxide at the catalyst surface. This pathway is not strongly affected by the electrode potential, leading to the relatively constant N<sub>2</sub> selectivity over the investigated cell voltage range.

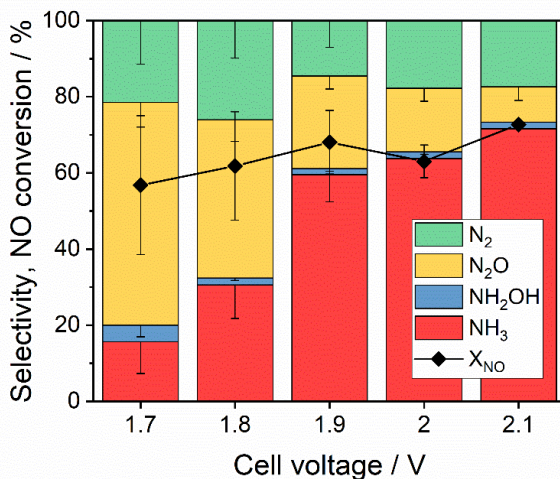


Figure 5.7: NO conversion and selectivity to various nitrogen products as a function of cell voltage, 25 mL min<sup>-1</sup> 5% NO/He cathode feed, 2.5 mg cm<sup>-2</sup> 40 wt% Ru/C cathode catalyst, 1 mg cm<sup>-2</sup> IrO<sub>2</sub> anode catalyst, Nafion 115, 80 °C.

N<sub>2</sub>O formation appeared more favorable at low cell voltage, showing a considerable faradaic efficiency of 28% at 1.7 V, which decreased to 2% at 2.1 V. This is in good agreement with literature, which reports N<sub>2</sub>O formation dominating at high cathodic potentials (0.3-0.7 V vs. RHE).<sup>28</sup> In our case, this represents the low cell voltage region. In literature, more favored ammonia formation has been reported at low cathodic potentials (<0.3 V vs. RHE). In our case, this condition is reflected in the high cell voltage region. Hydroxylamine formation was also detected, although the amounts were low throughout the investigated cell voltage range. The highest recorded faradaic efficiency for hydroxylamine was 6.5% at 1.7 V cell voltage. At higher cell voltages, it dropped below 2%.

The ammonia faradaic efficiency as a function of cell voltage greatly resembles the trends observed in our work on aqueous nitrate reduction with the same ruthenium catalyst.<sup>26</sup> This suggests that the reaction proceeds via a similar mechanism. In nitrate reduction, adsorbed NO may be an important reaction intermediate from which various products can emerge.<sup>29</sup> Furthermore, as it is likely that the catalyst-ionomer interface is wet during the operation due to water diffusion from the anode side, NO may be absorbed in the wet ionomer phase and may subsequently undergo transformation to ammonia.

Overall, the obtained ammonia yield ( $0.51 \text{ mmol cm}^{-2} \text{ h}^{-1}$  at 2.1 V cell voltage with a faradaic efficiency of 57%) was among the highest reported in literature (Figure 5.8). Furthermore, the reaction was implemented in a flow reactor which is more practical for scale-up compared to the generally reported cells with liquid electrolyte.<sup>20, 22, 23</sup> Our study demonstrates that NORR in a PEM cell is able to surpass the performance obtained in most reports using batch cells, making the approach attractive for scaling up.

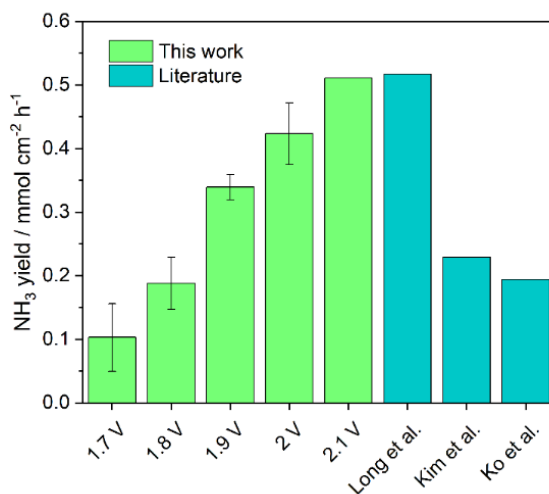


Figure 5.8: Comparison between NORR ammonia yield rates in our work and in literature.<sup>20, 22, 23</sup>

### 5.3.2 Impact of anode catalyst loading

The results above show promising activity in NORR towards ammonia. At the same time, the competitive and dominating HER leads to low ammonia faradaic efficiency at cell voltages above 2 V. To investigate the importance of the balance between the anode and cathode reaction rates, experiments with different iridium oxide loadings at the anode were conducted.<sup>26</sup> The rates of water oxidation and proton generation are dependent on the number of active sites on the catalyst surface at the anode. If the anode catalyst loading is too high, elevated current densities can be achieved in the PEM cell, but most of the electrons are inefficiently used in the undesired reaction of proton recombination to produce hydrogen at the cathode, unless a hindrance for HER is in place. In the experiments described in this section, the cathode catalyst loading over MEAs was kept constant at  $2.5 \text{ mg cm}^{-2}$ , while iridium oxide loadings were varied: 0.3, 1 or  $2 \text{ mg cm}^{-2}$ .

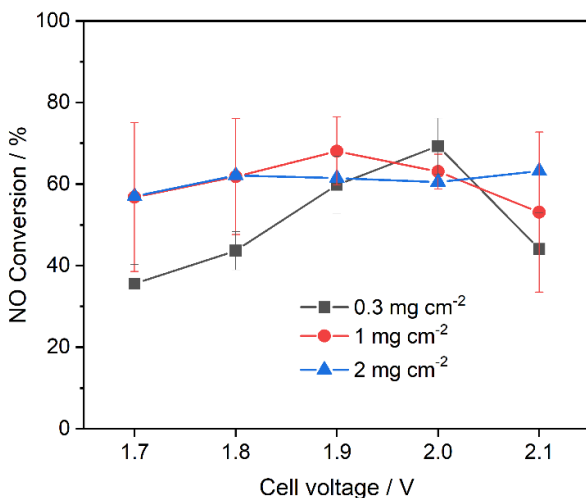


Figure 5.9: NO conversion as a function of cell voltage for MEAs with different iridium oxide anode catalyst loading, 25 mL min<sup>-1</sup> 5% NO/He cathode feed, 2.5 mg cm<sup>-2</sup> 40 wt% Ru/C cathode catalyst, Nafion I 15, 80 °C.

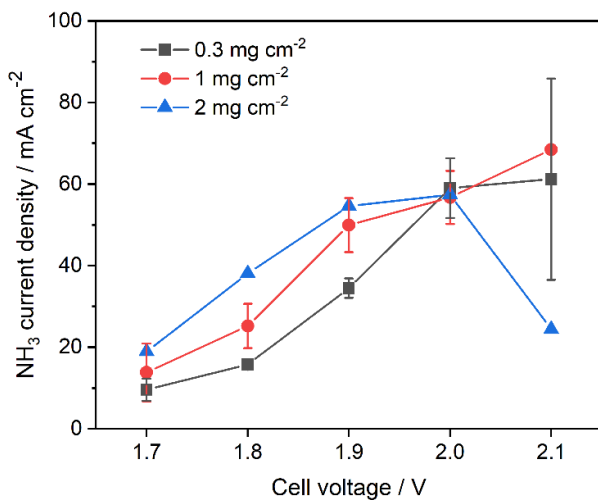


Figure 5.10: Ammonia partial current density as a function of cell voltage for MEAs with different iridium oxide anode catalyst loading, 25 mL min<sup>-1</sup> 5% NO/He cathode feed, 2.5 mg cm<sup>-2</sup> 40 wt% Ru/C cathode catalyst, Nafion I 15, 80 °C.

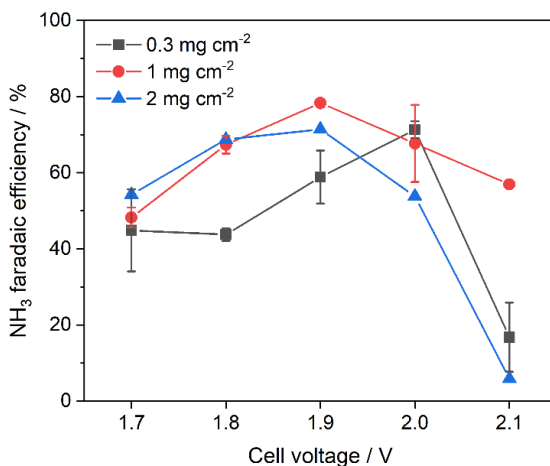


Figure 5.11: Faradaic efficiency as a function of cell voltage for MEAs with different iridium oxide anode catalyst loading, 25 mL min<sup>-1</sup> 5% NO/He cathode feed, 2.5 mg cm<sup>-2</sup> 40 wt% Ru/C cathode catalyst, Nafion 115, 80 °C.

Figure 5.9 shows that at cell voltages between 1.7 and 1.9 V, NO conversion increases with iridium oxide loading. At 2.0 V, similar performance for the three MEAs was recorded. At 2.1 V, the 1 mg cm<sup>-2</sup> IrO<sub>2</sub> MEA was found as performing the best. The ammonia partial current density (Figure 5.10), which is the result of multiplying faradaic efficiency and total current density, indicates that for 0.3 mg cm<sup>-2</sup> IrO<sub>2</sub> MEA, the proton generation rate at the anode is low, explaining the poorer NO conversion observed in Figure 5.9. For the 1 and 2 mg cm<sup>-2</sup> IrO<sub>2</sub> MEAs, ammonia partial current density increases with iridium oxide loading. At the same time, the ammonia faradaic efficiency decreases with the increase of iridium oxide loading from 1 to 2 mg cm<sup>-2</sup> (Figure 5.11) at cell voltages above 1.8 V. The likely explanation for this observation is that NORR to ammonia proceeds via a heterogeneous electrolysis-assisted hydrogenation mechanism (i.e., NO reduction by produced H<sub>2</sub>) at cell voltages above 1.9 V. This hypothesis is supported by the observation of a higher ammonia production yield for the MEA with 2 mg cm<sup>-2</sup> iridium oxide loading (Figure 5.12). It is also notable that the highest ammonia yield was observed at 2.1 V cell voltage for the 1 mg cm<sup>-2</sup> MEA, where ammonia faradaic efficiency exhibited a modest value of 57%, but NO conversion was highest (ca. 70%) along with the ammonia partial current density (ca. 70 mA cm<sup>-2</sup>).

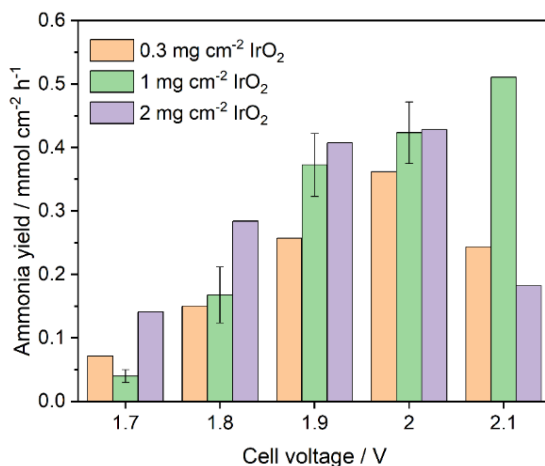


Figure 5.12: Ammonia yield as a function of cell voltage for MEAs with various iridium oxide anode catalyst loading.

2 mg cm<sup>-2</sup> is the typical loading for PEM water electrolyzers, but due to the high costs of iridium oxide it is generally desirable to use lower loadings.<sup>30</sup> For further experiments in this study, the intermediate iridium oxide loading of 1 mg cm<sup>-2</sup> was used to test the lower loading and advantageous faradaic efficiency to NH<sub>3</sub>. Loading as low as 0.3 mg cm<sup>-2</sup> IrO<sub>2</sub> over membranes is technically challenging due to inhomogeneities that arise during catalyst spray-coating deposition.

### 5.3.3 Towards complete single-pass NO conversion

After identifying faradaic efficiency and conversion trends as a function of cell voltage, our next goal was to maximize NO conversion by optimizing reaction conditions further. One of the parameters that are easy to tune was the gas flow through the cathode compartment of the PEM cell. It is expected that higher NO conversion can be achieved at low flow rate due to a longer residence time of NO molecules in the PEM cell. The flow variation experiments were conducted at 1.9 V cell voltage, where the best performance was observed in terms of ammonia faradaic efficiency and NO conversion. At 8 mL min<sup>-1</sup> 5% NO/He flow, 97% single-pass conversion was achieved in the PEM cell (Figure 5.13). However, the faradaic efficiency towards ammonia is lower at these conditions, likely due

to the low reactant availability at the catalyst surface at high conversion and proton recombination to hydrogen.

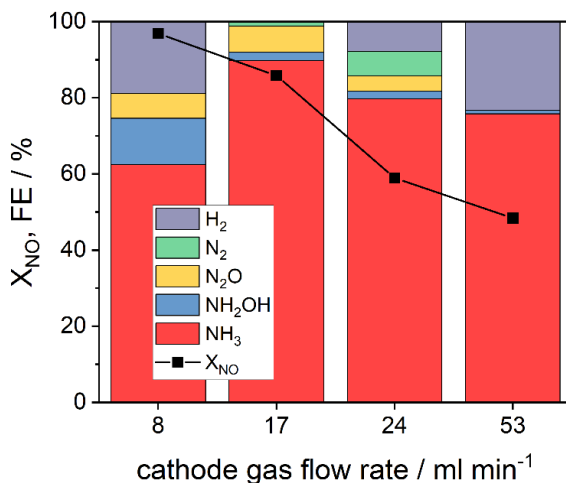


Figure 5.13: NO conversion ( $X_{\text{NO}}$ ) and faradaic efficiency (FE) towards ammonia as a function of cathode gas flow rate at 1.9 V cell voltage, 2.5 mg cm<sup>-2</sup> 40 wt% Ru/C cathode catalyst, 1 mg cm<sup>-2</sup> IrO<sub>2</sub> anode catalyst, Nafion 115, 80 °C.

At an increased flow rate, NO conversion decreased as expected. The lowest value of 48% was recorded at 53 mL min<sup>-1</sup> gas flow. An even higher ammonia faradaic efficiency was found at the lower flow rate of 17 mL min<sup>-1</sup> as compared to at 24 mL min<sup>-1</sup> of the previous experiments (Figure 5.6). NO conversion showed a further decrease at 53 mL min<sup>-1</sup> flow, reaching 73%. This could be due to less efficient contact of NO with the catalyst or less efficient NO absorption in the ionomer. Another possibility is the drying of the catalyst/ionomer interface at high gas flows. This point requires further investigation.

### 5.3.4 Experiments with hydrogen oxidation at the anode

We further explored the possibility of operating with hydrogen oxidation at the anode. This may allow for a more precise control of the competing HER, yielding higher faradaic efficiency towards ammonium, besides studying cathodic potential more independently.<sup>26</sup>

A similar approach has been reported and referred to as “electrogenative nitric oxide reduction”, suggesting a galvanic cell (fuel cell) operation mode.<sup>17, 18</sup> Porous platinum and ruthenium black were used as cathode catalysts in various acidic electrolytes, like HClO<sub>4</sub>,

HCl, H<sub>2</sub>SO<sub>4</sub>, H<sub>3</sub>PO<sub>4</sub> and HNO<sub>3</sub>. Almost full NO conversion was achieved for the Pt electrode. The selectivity was strongly influenced by the choice of electrolyte. For Ru, a higher ammonia selectivity was observed, but similar to Pt, it varied strongly with the used electrolyte.

Considering the standard reduction potential of nitric oxide to ammonia (Eq. 5.4), coupled with HOR at the anode (Eq. 5.5), a theoretical cell potential of 0.836 V is obtained (Eq. 5.6).



$$E^\circ_{\text{cell}} = 0.836 \text{ V} - 0 \text{ V} = 0.836 \text{ V} \quad \text{Eq. 5.6}$$

In our work, an open circuit potential of approximately 0.6 V was measured. However, reduction products could not be detected in the voltage range reported by Langer and Page, 0 – 0.6 V, and very low current densities were recorded during our experiments.<sup>17, 18</sup> Since our main goal was to achieve as high NO conversion to NH<sub>3</sub> as possible, potentials more negative than 0 V were applied to drive the transformation (Figure 5.14). For the anode compartment of the cell, where a platinum catalyst and a hydrogen feed were used, the assumption of pseudo-RHE reference electrode holds at low current densities. Therefore, for these experiments, the applied potentials are reported vs. pseudo-RHE.

The most striking observation is the considerably higher faradaic efficiency towards hydrogen at comparable current densities to experiments with water oxidation at the anode. An explanation for the higher concentration of hydrogen in the outlet stream could be its crossover from the anode to the cathode compartment through the Nafion membrane, altering the faradaic efficiency values of nitrogen-containing species. This significant difference in faradaic efficiency was not observed in our liquid-phase nitrate reduction experiments. However, there we used a diluted hydrogen feed of 4% in He, while a pure hydrogen feed was used for the NORR experiments of this work. Initially, the choice for undiluted hydrogen was made in order to explore the fuel cell mode operation without anticipating the impact of its diffusion through the membrane on the reaction performance.



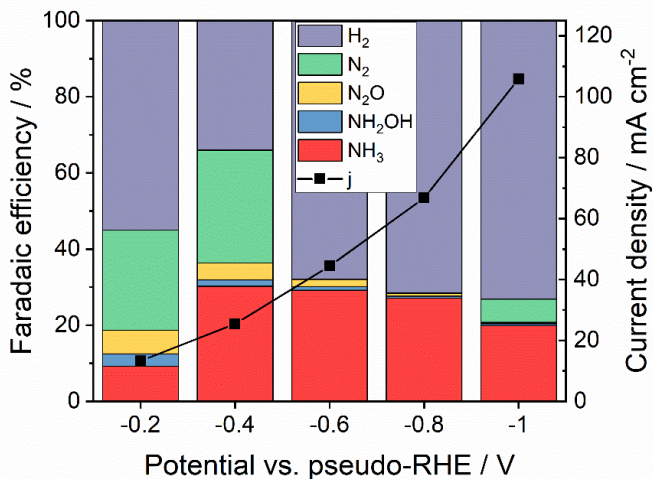


Figure 5.14: Faradaic efficiency with recorded current density as a function of applied potential (vs. pseudo-RHE), 30 mL min<sup>-1</sup> 5%NO/He cathode feed, 2.5 mg cm<sup>-2</sup> 40 wt% Ru/C cathode catalyst, 50 mL min<sup>-1</sup> H<sub>2</sub> anode feed, 1.5 mg cm<sup>-2</sup> 40 wt% Pt/C anode catalyst, Nafion 115, 80 °C.

The lowest faradaic efficiency towards ammonia (approximately 9%) was observed at the lowest applied potential of -0.2 V vs. pseudo-RHE. It reached a maximum faradaic efficiency of 30% at -0.4 V vs. pseudo-RHE. At more negative cell voltages, a slight decrease was observed with the ammonia faradaic efficiency of 20% at -1 V vs. pseudo-RHE, accompanied by an increase in hydrogen formation.

The NO conversion was also significantly lower compared to experiments with water oxidation at the anode (Figure 5.15 vs. Figure 5.7). It increased upon shifting applied potentials to more negative values, reaching a maximum of approximately 30% at -1 V vs. pseudo-RHE. Interestingly, ammonia selectivity showed a maximum at -0.8 V vs. pseudo-RHE (approximately 85%), which is different from the potential at which the highest faradaic efficiency was observed (-0.4 V vs. pseudo-RHE). This is different from the previous observations both for NORR experiments with water oxidation at the anode and nitrate reduction experiments, where the highest ammonia faradaic efficiency and selectivity was generally observed at the same cell voltage. This difference could be caused by hydrogen crossover through the membrane. Subsequently, higher H<sub>2</sub> concentrations might become available at the catalyst surface, leading to a higher NO hydrogenation rate and higher selectivity to ammonia as a result.

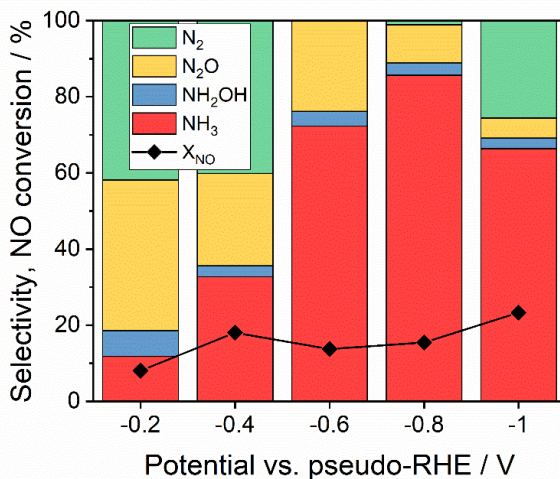


Figure 5.15: NO conversion and selectivity to nitrogen reduction products as a function of applied potential (vs. pseudo-RHE), 30 mL min<sup>-1</sup> 5%NO/He cathode feed, 2.5 mg cm<sup>-2</sup> 40 wt% Ru/C cathode catalyst, 50 mL min<sup>-1</sup> H<sub>2</sub> anode feed, 1.5 mg cm<sup>-2</sup> 40 wt% Pt/C anode catalyst, Nafion 115, 80 °C.

The NO conversion was also significantly lower compared to experiments with water oxidation at the anode (Figure 5.15 vs. Figure 5.7). It increased upon shifting applied potentials to more negative values, reaching a maximum of approximately 30% at -1 V vs. pseudo-RHE. Interestingly, ammonia selectivity showed a maximum at -0.8 V vs. pseudo-RHE (ca. 85%), which is different from the potential at which the highest faradaic efficiency was observed (-0.4 V vs. pseudo-RHE). This is different from the previous observations both for NORR experiments with water oxidation at the anode and nitrate reduction experiments, where the highest ammonia faradaic efficiency and selectivity was generally observed at the same cell voltage. This difference could be caused by hydrogen crossover through the membrane. Subsequently, higher H<sub>2</sub> concentrations might become available at the catalyst surface, leading to a higher NO hydrogenation rate and higher selectivity to ammonia as a result.

Overall, the performance of NORR to ammonia with hydrogen oxidation at the anode was not as high as in the experiments with water oxidation at the anode. Generally, we found the cell operation with gases both at the cathode and anode more challenging. In the first experiments that we conducted we found that gas humidification and electrode flooding play an important role for the long-term stability of the cell. The optimization of these

aspects was not conducted in this study, but it should allow for achieving comparable performance to experiments with water oxidation at the anode.

### 5.3.5 NORR as potential $\text{NO}_x$ abatement technology

Experiments described in the previous sections were conducted with a 5%  $\text{NO}/\text{He}$  mixture. In practice, such high  $\text{NO}$  concentrations might not be accessible in typical  $\text{NO}$  sources, such as power plants and car exhaust streams.  $\text{NO}_x$  concentration in such feeds is typically between 500 and 1000 ppm.<sup>31</sup> To investigate the applicability of NORR in PEM cells for more realistic  $\text{NO}_x$ -containing feeds, we conducted experiments with a 983 ppm  $\text{NO}/\text{He}$  mixture. In this case, the formed ammonia was not collected in the acid trap, and a condenser was used to remove the majority of water and ammonia after the PEM cell, which interfered with our established transmission-IR quantification method at such low  $\text{NO}$  concentration (Figure 5.3). Therefore, we only investigated whether a relevant single pass  $\text{NO}$  conversion could be achieved for low  $\text{NO}$  concentration streams.

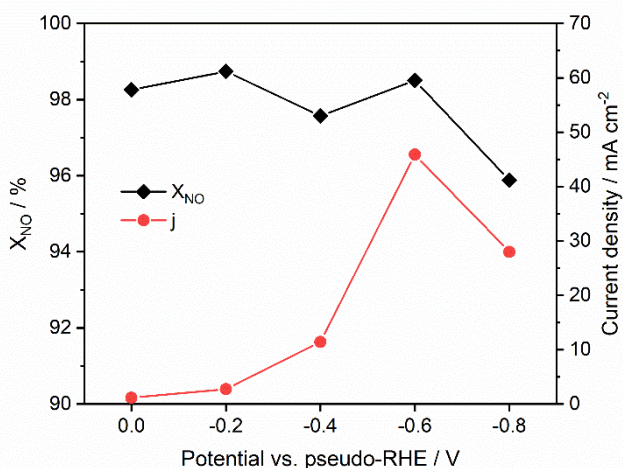


Figure 5.16:  $\text{NO}$  conversion ( $X_{\text{NO}}$ ) and recorded current density as a function of applied potential (vs. pseudo-RHE) during experiments with 983 ppm  $\text{NO}/\text{He}$  feed,  $2.5 \text{ mg cm}^{-2}$  40 wt%  $\text{Ru}/\text{C}$  cathode catalyst,  $1.5 \text{ mg cm}^{-2}$  40 wt%  $\text{Pt}/\text{C}$  anode catalyst, Nafion 115,  $80^\circ\text{C}$ .

As shown in Figure 5.16,  $\text{NO}$  conversion exceeds with 98% already at 0 V vs. pseudo-RHE. The current density exhibited a remarkably low value of approximately  $1 \text{ mA cm}^{-2}$ . The current density increased between -0.2 and -0.6 V and the  $\text{NO}$  conversion showed a

relatively stable value of around 98%. At -0.8 V a drop in current density and NO conversion was observed, possibly due to suboptimal humidification/water management in the cell.

The NORR performance reported in this work shows the great potential of this technology for NO<sub>x</sub> abatement applications to pollutant abatement (N<sub>2</sub> formation) or value creation (NH<sub>3</sub> formation), greatly overcoming state-of-the-art technologies in terms of energy efficiency. The Ru catalyst was shown to selectively produce ammonia in NORR. However, if NORR to nitrogen is targeted, alternative catalysts such as Pd or Cu are worth investigating, as these were proved active in nitrate reduction to nitrogen.<sup>25</sup> These metals also have the advantage of being cheaper than Ru.

## 5.4 Conclusions

The electrochemical conversion of NO to NH<sub>3</sub> in a PEM cell was investigated. A Ru/C catalyst afforded exceptional reaction performance with NO conversion reaching approximately 97% and faradaic efficiency of approximately 93% towards ammonia using a 5% NO/He feed. The recorded ammonia yield of 0.51 mmol cm<sup>-2</sup> h<sup>-1</sup> NH<sub>3</sub> is among the highest reported to date. This is particularly promising for large-scale applications, because all the advantages of PEM cells, such as low Ohmic losses, good product separation and relatively easy scalability, apply to NORR. Experiments with a 983 ppm NO feed, comparable to typical NO<sub>x</sub> concentrations in car exhaust and power plant flue gas streams, were conducted and 98% conversion was achieved at potentials as low as 0 V, indicating that the PEM cell could be used as an alternative to state-of-the-art NO<sub>x</sub> abatement technologies. The main advantages for such application are the *in situ* generation of reductant (hydrogen atom/molecule) and the low temperature (approximately 80 °C) at which the PEM cell operates, compared to the 300 °C and above for selective catalytic reduction (SCR), three-way catalysis (TWC) and NO<sub>x</sub> storage and reduction (NSR).

## 5.5 References

1. M. Kampa and E. Castanas, *Environ. Pollut.*, 2008, **151**, 362.
2. K. Skalska, J. S. Miller and S. Ledakowicz, *Sci. Total Environ.*, 2010, **408**, 3976.
3. L. K. Boerner, in *Chemical & Engineering News*, American Chemical Society, 2019, vol. 97.

4. X. Zhang, E. A. Davidson, D. L. Mauzerall, T. D. Searchinger, P. Dumas and Y. Shen, *Nature*, 2015, **528**, 51.
5. G. Soloveichik, *Nat. Catal.*, 2019, **2**, 377.
6. B. H. R. Suryanto, H.-L. Du, D. Wang, J. Chen, A. N. Simonov and D. R. MacFarlane, *Nat. Catal.*, 2019, **2**, 290.
7. V. Kyriakou, I. Garagounis, A. Vourros, E. Vasileiou and M. Stoukides, *Joule*, 2020, **4**, 142.
8. C. Ampelli, *Nat. Catal.*, 2020, **3**, 420.
9. H. S. Eyde, *Journal of the Royal Society of Arts*, 1909, **57**, 568.
10. K. H. R. Rouwenhorst, F. Jardali, A. Bogaerts and L. Lefferts, *Energy Environ. Sci.*, 2021, **14**, 2520.
11. Y. Wang, A. W. DeSilva, G. C. Goldenbaum and R. R. Dickerson, *Journal of Geophysical Research: Atmospheres*, 1998, **103**, 19149.
12. N. Cherkasov, A. O. Ibhadon and P. Fitzpatrick, *Chemical Engineering and Processing: Process Intensification*, 2015, **90**, 24.
13. J. Medford and M. C. Hatzell, *ACS Catal.*, 2017, **7**, 2624.
14. M. Anand, C. S. Abraham and J. K. Nørskov, *Chemical Science*, 2021, **12**, 6442.
15. R. Hawtof, S. Ghosh, E. Guarr, C. Xu, R. Mohan Sankaran and N. Renner Julie, *Science Advances*, 2019, **5**, eaat5778.
16. L. J. J. Janssen, M. M. J. Pieterse and E. Barendrecht, *Electrochim. Acta*, 1977, **22**, 27.
17. S. H. Langer and K. T. Pate, *Nature*, 1980, **284**, 434.
18. S. H. Langer and K. T. Pate, *Industrial & Engineering Chemistry Process Design and Development*, 1983, **22**, 264.

19. J. Soto-Hernández, C. R. Santiago-Ramirez, E. Ramirez-Meneses, M. Luna-Trujillo, J.-A. Wang, L. Lartundo-Rojas and A. Manzo-Robledo, *Appl. Catal. B*, 2019, **259**, 118048.
20. J. Long, S. Chen, Y. Zhang, C. Guo, X. Fu, D. Deng and J. Xiao, *Angew. Chem., Int. Ed.*, 2020, **59**, 9711.
21. J. Choi, H.-L. Du, C. K. Nguyen, B. H. R. Suryanto, A. N. Simonov and D. R. MacFarlane, *ACS Energy Lett.*, 2020, **5**, 2095.
22. D. Kim, D. Shin, J. Heo, H. Lim, J.-A. Lim, H. M. Jeong, B.-S. Kim, I. Heo, I. Oh, B. Lee, M. Sharma, H. Lim, H. Kim and Y. Kwon, *ACS Energy Lett.*, 2020, **5**, 3647.
23. B. H. Ko, B. Hasa, H. Shin, E. Jeng, S. Overa, W. Chen and F. Jiao, *Nat. Commun.*, 2020, **11**, 5856.
24. O. M. Ilinitich, F. P. Cuperus, L. V. Nosova and E. N. Gribov, *Catal. Today*, 2000, **56**, 137.
25. Afkhami, T. Madrakian and A. Maleki, *Anal. Sci.*, 2006, **22**, 329.
26. S. Bunea, K. Clemens and A. Urakawa, *ChemSusChem*, 2021, **15**, e202102180.
27. J. Ampurdanés, S. Bunea and A. Urakawa, *ChemSusChem*, 2021, **14**, 1534.
28. H. Wan, A. Bagger and J. Rossmeisl, *Angew. Chem., Int. Ed.*, 2021, **60**, 21966.
29. V. Rosca, M. Duca, M. T. de Groot and M. T. M. Koper, *Chem. Rev.*, 2009, **109**, 2209.
30. M. Carmo, D. L. Fritz, J. Mergel and D. Stolten, *Int. J. Hydrogen Energy*, 2013, **38**, 4901.
31. F. Gholami, M. Tomas, Z. Gholami and M. Vakili, *Sci. Total Environ.*, 2020, **714**, 136712



# 6

## Conclusions and outlook

Strong commitment to net-zero emissions goals has triggered the fast deployment of both alkaline and PEM electrolysis systems on large scale. Although some skepticism still exists in the industry and in the scientific community, mainly due to challenges of hydrogen storage and transportation infrastructure, at the moment it appears that the wide adoption of green hydrogen technologies is inevitable. The strongest argument in favor of electrolysis-generated hydrogen as energy vector is the lack of more efficient or scalable alternatives.

High costs and scarcity of noble metals used as catalysts, particularly iridium, might hinder PEM electrolysis from becoming the leading technology, but it has already found niche applications, and will definitely continue to do so. This does not imply that research into developing cheaper catalysts should stop.

At the same time, a technology related to PEM, namely alkaline anion exchange membrane electrolysis (AEM), in which the acidic membrane is replaced by rapidly developing alkaline membranes, allows for the use of non-noble metal catalysts such as nickel oxide for the anodic OER. To date, one of the most important problems of AEMs is membrane durability and long-term stability. Just as in the case of PEM electrolysis, it is expected that research in novel membrane materials will solve this issue.

The work presented in Chapters 1 and 2 on iridium-tin oxygen evolution catalysts offers a deeper understanding of the importance of morphology and nano-structuring in binary catalysts for achieving superior performance. What we believe is particularly interesting for the research community is that the developed catalyst materials were tested in a PEM



electrolysis cell directly, and not in a batch three electrode setup, which is very common in literature. Due to differences in the electrode/electrolyte interface between the two cells, performance differences arise, and extrapolation of the activity observed in three electrode cells to PEM cells is not precise.

For a long time, nitrogen electrochemistry has only been a topic of fundamental research in the scientific community. Although numerous brilliant reports on reaction mechanisms were published, only in the recent years these reactions became interesting from the perspective of scale-up and as an alternative to the Haber-Bosch process. To date, electrochemical nitrogen activation has proved inefficient. We believe that despite tremendous efforts and literature reports, it will be difficult to achieve relevant production rates to compete with Haber-Bosch. On the other hand, two-step activation approaches where the first step is nitrogen oxidation to nitric oxide and the second step is the nitric oxide reduction to ammonia might be easier to develop on a large scale. Technology readiness level (TRL) of such technologies to date is still low (TRL1-3) but we expect that many technologies will emerge in the following years, when wide consensus is reached regarding the low efficiency of electrochemical nitrogen activation.

The work described in Chapters 3 and 4 might provide useful insight into the importance of tuning proton transport through the Nafion membrane for reaching high efficiencies of the desired reaction. The findings might be translated to other electrochemical reactions and cells as well, for example to electrochemical CO<sub>2</sub> reduction. Ruthenium, which was used as a catalyst in our work is still a scarce and expensive noble metal. Research into cheaper alternatives, of which we found copper as promising, is recommended for advancing the field further.

Meanwhile, to decrease the enormous carbon footprint of the Haber-Bosch process, in line with net-zero emission pledges, using electrolysis-generated hydrogen would represent an important step forward and would buy more time for the scientific community to develop more efficient, entirely electrocatalytic alternatives.





## Acknowledgements

I would like to thank Professor Atsushi Urakawa for offering me the opportunity to conduct my PhD studies in his research group. Looking back at the last four years, I can certainly say that I could not have imagined a more suitable PhD supervisor. I feel lucky that I could enjoy a perfect balance of research freedom and very precise guidance towards becoming a more critical thinker and an independent researcher. Doing a PhD in two countries was an amazing and unique experience, both professionally and personally. Thank you very much, Atsushi!

From 2019 on, after moving to Delft, I had the honor to have Professor Tom Burdyny as my copromotor. Dear Tom, your positive attitude and advice was extremely stimulating at moments when the future outcome for a few chapters in this thesis looked unclear. Your very clear vision about research publishing has been of great help. I am sincerely grateful to you for that.

I would like to thank the committee members for reading my dissertation and for participating in the defense ceremony.

Many thanks to the members of the Urakawa group at ICIQ in Tarragona and of the Catalysis Engineering section at TU Delft for their support and friendship: Atul, Jordi, Rohit, Lingjun, Nat, Donato, Min, Disha, Thomas, Jose, Kei.

Dear Bart, Harrie, Willy and Liliana, your contribution to keeping the lab running smoothly cannot be overestimated. Thank you very much for your help and expertise. I would like to thank the secretaries of the group, Aurora at ICIQ and Els at TU Delft, for their administrative support.

I am especially glad that I had the chance to supervise Bachelor and Master students. Guiding them through their projects was an extremely useful experience for me because I found myself learning together with them more about my research topic. The work described in Chapters 4 and 5 would not have been possible without the contribution of Kevin and Manoj. It was a pleasure to work with you! Thank you!

## Acknowledgements

---

I am grateful to my family for supporting me in pursuing a PhD, my mother Diana, my father Marin and my two sisters, Maria and Ioana. Although we don't see each other as often as we would like to, I always feel your support and care.

Finally, my wife Dorina. The completion of this thesis and the person that I became as a result of the PhD journey would not have been possible without her. I am deeply grateful for this.

Delft  
March 2022

## List of publications

Publications within the scope of this thesis:

**Bunea, S.;** Clemens, K.; Urakawa, A. Electrified conversion of contaminated water to value: selective conversion of aqueous nitrate to ammonia in a PEM cell. *ChemSusChem*, **2021**.

**Bunea, S.;** Zeng, P.; Willinger, M. G.; Urakawa, A. The influences of nanostructures of Sn and Ir for oxygen evolution reaction in PEM water electrolysis. *Under review*.

**Bunea, S.;** Coppens, M.; Urakawa, A. Electrochemical conversion of NO to NH<sub>3</sub> in a PEM cell. *In preparation*.

**Bunea, S.;** Urakawa, A. Electrochemical conversion of NO to NH<sub>3</sub> in a PEM cell. *Patent application filed in February 2022*.

Publications outside the scope of this thesis:

Ampurdanés J.; **Bunea, S.;** Urakawa, A. PEM electrolysis-assisted catalysis combined with photocatalytic oxidation towards complete abatement of nitrogen-containing contaminants in water. *ChemSusChem*, **2021**, *14*, 1534.

**Bunea, S.;** Urakawa, A. In Situ Spectroscopic Methods to Study Electrochemical CO<sub>2</sub> Reduction. In *Carbon Dioxide Electrochemistry: Homogeneous and Heterogeneous Catalysis*; Robert, M., Costentin, C., Daasbjerg, K., Eds.; The Royal Society of Chemistry, **2021**; pp. 347-407.

Gabrysch, T.; Peng, B.; **Bunea, S.;** Dyker, G.; Muhler, M. The Role of Metallic Copper in the Selective Hydrodeoxygenation of Glycerol to 1,2-Propanediol over Cu/ZrO<sub>2</sub>. *ChemCatChem*, **2018**, *10*, 1344.



## Curriculum Vitae

Sorin Bunea was born on April 14<sup>th</sup>, 1991, in Orhei, Republic of Moldova. He received his upper secondary education at the Spiru Haret Lyceum in Chişinău, Republic of Moldova and obtained his high school diploma (Diplomă de Bacalaureat) in 2010. He started studying chemistry at Alexandru Ioan Cuza University of Iaşi in Romania in 2011, focusing on organic chemistry. After successfully finishing his BSc studies in 2014, he moved to Germany in the



same year to pursue his MSc degree, at Ruhr University Bochum, supported by a study scholarship from the German Academic Exchange Service (DAAD). There, he focused on heterogeneous catalysis and studied the glycerol hydrodeoxygenation reaction catalyzed by zirconia-supported copper catalysts under the supervision of Prof. dr. Martin Muhler. He obtained his MSc degree in chemistry, with a specialization in industrial chemistry in 2016. In 2017, he started his PhD studies under the supervision of Prof. dr. Atsushi Urakawa at the Institute of Chemical Research of Catalonia in Tarragona, Spain. In 2019, he joined Professor Urakawa at the Catalysis Engineering section of the Chemical Engineering Department at Delft University of Technology. In his PhD studies, he focused on electrocatalytic water splitting and nitrate/nitric oxide reduction in PEM cells.



